UNIVERSITY OF MICHIGAN
JUN 17 1953
ENGINEERING LIBRARY

JOURNAL OF THE AERONAUTICAL SCIENCES

VOLUME 20 JUNE, 1953 NUMBER 6

CONTENTS

Fully Plastic Rotating Disc with Large Strains.....MELVIN ZAID 369

An Investigation of the Flow About Cones and Wedges at and Beyond the Critical Angle.....G. W. JOHNSTON 378

The Upwash Correction for an Oscillating Wing in a Wind Tunnel.....THEODORE R. GOODMAN 383

Stress Analysis of Sheet-Stringer Panels with Cutouts....HARVEY G. MCCOMB, JR. 387

Oscillating Airfoils at High Mach Number.....M. J. LIGHTHILL 402

The Contribution of Higher Mode Resonance to Helicopter Rotor-Blade Bending.....HAROLD HIRSCH 407

Readers' Forum: "Further Note on the Use of the Neutral Point as a Stability Parameter," by S. J. Deitchman; "A Note on the Weight of the Blades in an Axial-Flow Compressor," by John Mitchell Stephenson; "A Method for Differentiation of Experimental Data," by William M. Kauffman and Marvin Shinbrot; "Leading-Edge Separation from Delta Wings at Supersonic Speeds," by Mac C. Adams; "Improvement of Pressure Recovery of a Fixed Diffuser by Means of Suction," by Ashton M. Patterson; "The Two-Dimensional Incompressible Aerodynamic Coefficients for Oscillatory Changes in Airfoil Camber," by Irvin N. Spielberg; "Note on the Use of Two-Dimensional Compressible Flow Aerodynamic Coefficients in the Flutter Analysis of a Tapered Wing," by R. J. Werdes; "An Observation on the Vortex System of Dual-Rotation Propellers," by J. J. Eisenhuth and B. W. McCormick; "A Note on Second-Order Supersonic Flow Theory," by Robert E. Lavender; "Influence Matrix of Beam Vibration," by L. S. Dzung; "Regarding the Computation of Unsteady Air Forces by Means of Mathieu Functions," by Henry E. Fettis; "On the Measurement of Surface Pressure with a Static Probe," by W. W. Willmarth; "Concerning 'The Subsonic Calculation of Circulatory Spanwise Loadings for Oscillating Airfoils by Lifting-Line Techniques,'" by M. A. Dengler and Martin Goland; "Errata—'The von Kármán Integral Method as Applied to a Turbulent Boundary Layer,'" by Nguyen Van Le; "Errata—'Elastic Stability of Simply Supported Flat Rectangular Plates . . .,'" by Robert G. Noel.....426–440

Published by the
INSTITUTE OF THE AERONAUTICAL SCIENCES, INC.

JOURNAL OF THE AERONAUTICAL SCIENCES

Editor: HUGH L. DRYDEN, *Director, NACA*

Associate Editor: ROBERT R. DEXTER *Managing Editor:* BERNEICE H. JARCK

Editorial Committee

Aerodynamics

Francis Clauser
Howard Emmons
Antonio Ferri
Alexander Flax
R. Paul Harrington
R. T. Jones
Carl Kaplan
H. W. Liepmann
C. C. Lin
H. F. Ludloff
Harold Luskin
John R. Markham
Clark B. Millikan
Shatswell Ober
W. Bailey Oswald
Allen E. Puckett
Elliott G. Reid
H. J. E. Reid
Russell Robinson
G. B. Schubauer
W. R. Sears
John Stack
Theodore von Kármán
Richard von Mises

Air Transport

Charles Froesch
J. A. Herlihy
R. D. Kelly
Otto E. Kirchner
Jerome Lederer
John C. Leslie
R. Dixon Speas

Flight Testing

W. K. Ebel
R. R. Gilruth
Melvin N. Gough
E. G. Stout

Structures and Materials

W. B. Bleakney
E. W. Conlon
L. H. Donnell
E. C. Hartmann
N. J. Hoff
Samuel Levy
E. E. Lundquist
Alfred S. Niles
W. Ramberg
E. Reissner
F. R. Shanley
H. W. Sibert
C. R. Strang
S. Timoshenko
H. S. Tsien
Chi-Teh Wang

Rotating Wing Aircraft

F. B. Gustafson
K. H. Hohenemser
Bartram Kelley
R. B. Maloy
Ralph McClarren
R. H. Miller
R. H. Prewitt
Igor I. Sikorsky

Vibration and Flutter

Lee Arnold
M. A. Biot
R. L. Bisplinghoff
William Bollay
Chieh-Chien Chang
I. E. Garrick
Martin Goland
J. P. Den Hartog

Aircraft Design

W. E. Beall
W. K. Ebel
Hall L. Hibbard
Richard Hutton
C. L. Johnson
A. A. Kartveli
C. J. McCarthy
Fred E. Weick
Robert J. Woods

Electronics in Aviation

K. C. Black
E. F. Herzog
David S. Little
D. K. Martin
George Rappaport
Paul Rosenberg
L. M. Sherer

Physiologic Problems

H. G. Armstrong
Louis H. Bauer
Robert J. Benford
Eugene Du Bois
W. Randolph Lovelace, II
Ross A. MacFarland

Fuels and Oils

D. P. Barnard
J. H. Doolittle
Graham Edgar
R. T. Goodwin
S. D. Heron
A. M. Rothrock

Flight Propulsion

George W. Brady
Frank W. Caldwell
L. S. Hobbs
E. E. Johnson
Joseph Keenan
R. P. Kroon
Hans Reissner
Abe Silverstein
C. Fayette Taylor
E. S. Taylor
P. Taylor
E. S. Thompson
H. S. Tsien

Instruments

Allan G. Binnie
J. R. Bradburn
Charles H. Colvin
C. S. Draper
S. G. Eskin
O. E. Esval
H. W. Holzapfel
W. L. Howland
George H. Purcell
C. F. Savage
O. Hugo Schuck
C. L. Seward, Jr.
L. D. Statham
R. C. Sylvander
D. K. Warner

Meteorology

C. F. Brooks
D. M. Little
E. J. Minser
F. W. Reichelderfer
H. C. Willett

SUBSCRIPTION RATES

JOURNAL OF THE AERONAUTICAL SCIENCES, Published Monthly.—United States and Possessions: 1 Year, $12.00; Single Copies, $1.50. Foreign Countries Including Canada (American Currency Rates): 1 Year, $13.00; Single Copies, $1.50.

AERONAUTICAL ENGINEERING REVIEW, Published Monthly.—United States and Possessions: 1 Year, $3.00; Single Copies, $0.50. Foreign Countries Including Canada (American Currency Rates): 1 Year, $3.50; Single Copies, $0.50.

Notices of change of address should be sent to the Institute at least 30 days prior to actual change of address.

Manuscripts for publication, proofs, and all correspondence should be addressed to the Editorial Office of the JOURNAL.

Correspondence regarding subscriptions may be addressed to Publication Office, 20th and Northampton Sts., Easton, Pa., or to the Editorial Office of the JOURNAL OF THE AERONAUTICAL SCIENCES, 2 East 64th Street, New York 21, New York.

Copyright, 1953, by the Institute of the Aeronautical Sciences, Inc.

Entered as Second Class Matter at the Post Office, Easton, Pa., May 1, 1937. Acceptance for mailing at a special rate of Postage provided for in the Act of August 24, 1912. Authorized April 29, 1937.

JOURNAL OF THE AERONAUTICAL SCIENCES

VOLUME 20 JUNE, 1953 NUMBER 6

Fully Plastic Rotating Disc with Large Strains*

MELVIN ZAID†

Sperry Gyroscope Company‡

ABSTRACT

The thin rotating disc of arbitrary profile and boundary conditions is considered for a material with an arbitrary stress-strain curve. In order to investigate stresses, strains, and speeds leading to failure, a finite strain theory is used.

The concept of a strain plane is introduced, and with it, general solutions are obtained and particularized to many specific profiles and materials. Residual stresses in one particular case are evaluated. With the aid of these solutions, it is shown that the bursting speed is dependent largely on profile shape, and examples are presented to show this relationship.

The small strain theory indicates that complete yielding of a perfectly plastic disc takes place for a speed of about 17 per cent above that for a disc at the elastic limit. The large strain theory, however, indicates that a speed of approximately 100 per cent above the elastic limit can be achieved before the disc will burst. The latter is a more realistic theory for evaluation of allowable safety factors.

A theoretical solution for bursting is checked against previously performed experimental work and agrees to within 1 per cent. Strain distributions check quite well.

NOMENCLATURE

a = instantaneous radius to edge of disc

a' = original radius to edge of disc

A = $D\left[1 - \phi_r + \dfrac{x_b DJ - (\phi_t - \phi_r)}{1 - e^{\phi_t - \phi_r}}\right]$

b = undetermined radius

B = $D[2 - \phi_r]$**

c = constant

c_b = c/b

D = variable coefficient relating stress and strain**

E = modulus of elasticity

J = $\dfrac{3}{2} T x_b + \dfrac{\phi_r}{D} \dfrac{d}{dx_b} (\ln l_0)$**

l = deformed length

l_0 = undeformed length

q = l_0 at x_{bi}

r = radial distance to an element in the undeformed disc

r_a = r/a**

$r_{a'}$ = r/a'**

r_b = r/b**

s = effective stress = $(\sqrt{2}/2)\sqrt{(s_1 - s_2)^2 + (s_2 - s_3)^2 + (s_3 - s_1)^2}$

s_0 = effective stress at elastic limit

s_1, s_2, s_3 = principal stresses

s_r, s_t, s_z = radial, tangential, and axial stresses, respectively, corresponding to the position $(r + u)$ in the deformed disc

t = deformed thickness

t_0 = undeformed thickness††

T = $\omega^2 b^2 \gamma / s_0$

T_1 = $\omega^2 a^2 \gamma / s_0$

u = radial displacement of an element at initial radius r during plastic yielding of the disc

x = $r + u$**

x_a = x/a**

x_b = x/b**

γ = density (mass per unit³)

δ_k^n = $\begin{cases} 0, & n \neq k \\ 1, & n = k \end{cases}$

ϵ = effective strain = $(\sqrt{2}/3)\sqrt{(\epsilon_1 - \epsilon_2)^2 + (\epsilon_2 - \epsilon_3)^2 + (\epsilon_3 - \epsilon_1)^2}$

$\epsilon_r, \epsilon_t, \epsilon_z$ = radial, tangential and axial strain, respectively, corresponding to an element at distance $(r + u)$ in the deformed disc**

θ = angle

ρ = normalizing factor

σ = s/s_0

$\sigma_r, \sigma_t, \sigma_z$ = $s_r/s_0, s_t/s_0, s_z/s_0$

σ_r' = $\sigma_{residual}$

σ_p = $\sigma_{plastic}$

σ_e = $\sigma_{elastic}$

$\tau_{rz}, \tau_{rt}, \tau_{zt}$ = shear stresses

ϕ_r = $2\epsilon_r + \epsilon_t$**

ϕ_t = $2\epsilon_t + \epsilon_r$**

ω = angular speed (rad. per unit time)

ω_0 = bursting speed of flat disc

Received January 9, 1953.

* Based on Doctoral Thesis, Massachusetts Institute of Technology, 1951. The author is deeply indebted to Dr. C. W. MacGregor for his invaluable aid while at M.I.T.

† Senior Engineer.

‡ Division of The Sperry Corporation.

** A further subscript 0, i, or 1 refers to the outside or inside or position only slightly removed from i.

†† A second subscript e refers to the thickness at the edge.

UNIVERSITY OF MICHIGAN LIBRARIES

(I) Introduction

The thin rotating disc is often met in practical design problems. If the speed is sufficiently low, the disc will behave elastically, in which case the solution is known.[1] For intermediate speeds that lead to consideration of the plastic-elastic disc, the solution is also known.[2–6] However, except for experimental work, little has been done on a large strain theory for the thin rotating disc. Such a theory is useful in predicting bursting speeds and thus in establishing safety factors.

Since this paper represents an early step toward the development of such a theory, it is felt that certain simplying assumptions are justified. For instance, a deformation rather than a flow theory is used. From a purely mathematical point of view, it is sufficient to state this assumption and then solve the resulting equations. However, such a procedure can lead to unrealistic solutions. It is therefore worth while to state in advance some of the results obtained for this problem. (1) The only case for which a detailed study is made shows that the stress ratios remain nearly constant as the loading is increased. (2) For another case, in which the results had been previously established experimentally, the bursting speed is predicted to within 1 per cent, and the strain distributions agree quite well even for strains beyond the maximum load point of the tensile specimen.

Solutions are obtained for discs with flat and variable profiles and for a strain hardening or nonstrain-hardening material.

(II) Theory

It is assumed that:

(1) The material is homogeneous and isotropic.

(2) The sum of the plastic strains equals zero.

(3) The ratio of the principal true strain differences to the corresponding stress differences are equal.

(4) There is a unique relationship between effective stress and effective strain.

(5) The variation of stress across the thickness is neglected, as well as the effect of axial components of the radial stress for large deformations.

(6) Heating due to air friction is negligible.

The effective stress at a point is defined as

$$s = (\sqrt{2}/2)\sqrt{(s_1 - s_2)^2 + (s_2 - s_3)^2 + (s_3 - s_1)^2} \quad (1)$$

and the effective strain, as

$$\epsilon = (\sqrt{2}/3)\sqrt{(\epsilon_1 - \epsilon_2)^2 + (\epsilon_2 - \epsilon_3)^2 + (\epsilon_3 - \epsilon_1)^2} \quad (2)$$

Assumption (4) can be derived from a tension test in the form

$$s = f(\epsilon) \quad (3)$$

For the rotating disc

$$s_1 = s_r \qquad \epsilon_1 = \epsilon_r$$
$$s_2 = s_t \qquad \epsilon_2 = \epsilon_t$$
$$s_3 = s_z = 0 \qquad \epsilon_3 = \epsilon_z$$

and we take

$$\tau_{rt} = \tau_{tz} = \tau_{zr} = 0$$

Assumptions (2) and (3) lead to

$$E\epsilon_r = D^*[s_r - (1/2)s_t] \quad (4)$$

$$E\epsilon_t = D^*[s_t - (1/2)s_r] \quad (5)$$

$$E\epsilon_z = -(D^*/2)(s_t + s_r) \quad (6)$$

The true strain is defined, after Ludwik,[7] as

$$d\epsilon = dl/l$$

or

$$\epsilon = \ln (l/l_0)$$

This leads to

$$\epsilon_r = \ln \frac{d(r+u)}{dr} = \ln \left(1 + \frac{du}{dr}\right) \quad (7)$$

$$\epsilon_t = \ln \frac{(r+u)\,d\theta}{r\,d\theta} = \ln \left(1 + \frac{u}{r}\right) \quad (8)$$

$$\epsilon_z = \ln (t/t_0) \quad (9)$$

The equation of equilibrium taken in the radial direction is

$$\frac{ds_r}{d(r+u)} = \frac{s_t - s_r}{r+u} - s_r \frac{d}{d(r+u)} (\ln t) - \omega^2\gamma(r+u) \quad (10)$$

Combining Eqs. (7) and (8), one obtains the compatibility equation,

$$1 - e^{\epsilon_t - \epsilon_r} = (r+u)[d\epsilon_t/d(r+u)] \quad (11)$$

It is now convenient to introduce the following dimensionless variables:

$$D = D^*s_0, \qquad x_b = (r+u)/b$$
$$\sigma_r = s_r/s_0, \qquad \sigma_t = s_t/s_0$$
$$T = \omega^2 b^2 \gamma/s_0$$

Where b is an undetermined radius and s_0 an undetermined stress, usually taken as the elastic limit. The equations then become

$$\frac{d\sigma_r}{dx_b} = \frac{\sigma_t - \sigma_r}{x_b} - \sigma_r \frac{d}{dx_b} (\ln t) - Tx_b \quad (12)$$

$$x_b(d\epsilon_t/dx_b) = 1 - e^{\epsilon_t - \epsilon_r} \quad (13)$$

$$\sigma = g(\epsilon) \quad (14)$$

$$2\sigma^2 = (\sigma_r - \sigma_t)^2 + \sigma_r^2 + \sigma_t^2 \quad (15)$$

$$(9/2)\epsilon^2 = (\epsilon_r - \epsilon_t)^2 + (\epsilon_t - \epsilon_z)^2 + (\epsilon_z - \epsilon_r)^2 \quad (16)$$

$$\epsilon_r = D[\sigma_r - (\sigma_t/2)] \quad (17)$$

$$\epsilon_t = D[\sigma_t - (\sigma_r/2)] \tag{18}$$

$$\epsilon_z = -(D/2)(\sigma_r + \sigma_t) \tag{19}$$

$$\epsilon_z = \ln (t/t_0) \tag{20}$$

Let us define two new symbols

$$\phi_r = 2\epsilon_r + \epsilon_t \tag{21}$$

$$\phi_t = 2\epsilon_t + \epsilon_r \tag{22}$$

where $\phi_t - \phi_r = \epsilon_t - \epsilon_r$. Then Eqs. (17) and (18) can be combined to yield

$$\sigma_r = (2/3)(\phi_r/D) \tag{23}$$

$$\sigma_t = (2/3)(\phi_t/D) \tag{24}$$

Using these in Eqs. (15) and (16), there results

$$\epsilon = D\sigma \tag{25}$$

Rewriting Eq. (12) with these new quantities results in

$$\phi_r D' + D\left[\frac{\phi_t - \phi_r}{x_b} - \phi_r' - \phi_r (\ln t)'\right] - \frac{3}{2} D^2 T x_b = 0 \tag{26}$$

where

$$(d/dx_b)(\ \ ) \equiv (\ \ )'$$

Eqs. (13) to (20) inclusive and Eq. (26) supply nine independent equations with eleven unknowns, but, by assuming t_0, these are reduced to a system that can be solved in terms of one variable, x_b. It should be noted that Eq. (25) is derived from the other nine equations and therefore is not independent.

(III) Solution

The method of solution will be to write this group as a simple pair of linear equations that can be solved numerically.

Introducing Eqs. (13) and (20) into Eq. (26) there follows:

$$\frac{d\epsilon_t}{1 - e^{\phi_t - \phi_r}}\left[\frac{3}{2} D^2 T x_b^2 - D(\phi_t - \phi_r) + D\phi_r x_b \frac{d}{dx_b}(\ln t_0)\right] = \phi_r\, dD - D\, d\phi_r - D\phi_r\, d\epsilon_z \tag{27}$$

where we used

$$\frac{d}{dx_b}(\ln t) = \frac{d\epsilon_z}{dx_b} + \frac{d}{dx_b}(\ln t_0)$$

Using assumption (2), there results

$$\phi_r\, dD = A\, d\epsilon_t + B\, d\epsilon_r \tag{28}$$

where

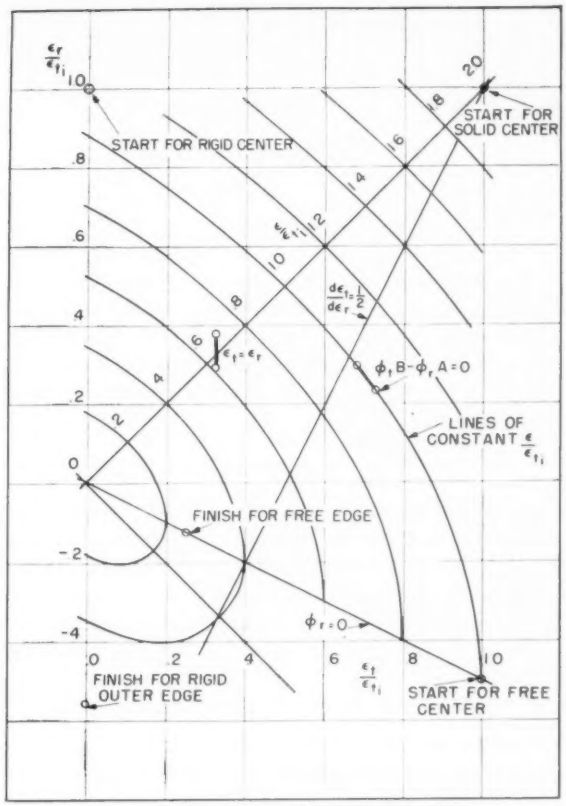
START FOR RIGID CENTER
START FOR SOLID CENTER
FINISH FOR FREE EDGE
FINISH FOR RIGID OUTER EDGE
START FOR FREE CENTER
LINES OF CONSTANT
$\phi_t B - \phi_r A = 0$
$\phi_r = 0$
$\epsilon_t = \epsilon_r$

FIG. 1. Boundary conditions on strain plane.

$$\left.\begin{aligned} A &= D\left[1 - \phi_r + \frac{x_b DJ - (\phi_t - \phi_r)}{1 - e^{\phi_t - \phi_r}}\right] \\ B &= D[2 - \phi_r] \\ J &= \frac{3}{2} T x_b + \frac{\phi_r}{D}\frac{d}{dx_b}(\ln t_0) \end{aligned}\right\} \tag{29}$$

To get the second equation, we write Eq. (16) in its differential form,

$$(3/2)\epsilon\, d\epsilon = \phi_r\, d\epsilon_r + \phi_t\, d\epsilon_t \tag{30}$$

Eqs. (28) and (30) are now written as

$$\left.\begin{aligned} d\epsilon_t &= \frac{(3/2)\, B\epsilon\, d\epsilon - \phi_r^2 dD}{B\phi_t - A\phi_r} \\ d\epsilon_r &= (\phi_r\, dD - A\, d\epsilon_t)/B \end{aligned}\right\} \tag{31}$$

$(B\phi_t - A\phi_r \neq 0)$. Eq. (31) establishes the strain path on a strain plane (Fig. 1) prescribed by Eq. (16).

For the special case of $B\phi_t - A\phi_r = 0$, it can be shown that the strain path is tangent to the lines of $\epsilon =$ constant or

$$d\epsilon_t/d\epsilon_r = -\phi_r/\phi_t = -B/A \tag{32}$$

A second special case occurs when the strain path crosses the line $\epsilon_r = \epsilon_t$, and $x_b \neq 0$. It can be shown in this case that

$$d\epsilon_t \to \left[\frac{(3/2)B\epsilon\, d\epsilon - \phi_r^2\, dD}{x_b D^2 J \phi_r}\right](\epsilon_t - \epsilon_r) \qquad (33)$$

or $d\epsilon_t \to 0$, $(\epsilon_t \to \epsilon_r)$. Using Eq. (33) in Eq. (13)

$$dx_b \to -\left[\frac{(3/2)B\epsilon\, d\epsilon - \phi_r^2\, dD}{\phi_r D^2 J}\right] \qquad (34)$$

$$d\epsilon_r \to (\phi_r/B)\, dD \qquad (35)$$

The procedure will then be to use Eqs. (13), (25), and (31), or any of the equations for special cases, together with the stress-strain diagram, to numerically evaluate the strain and instantaneous position (x_b). The original position of the point in question is then found from Eq. (8),

$$r_b = x_b/e^{\epsilon_t} \qquad (36)$$

It will thus only be necessary to establish the boundary conditions in strain components. Then, once a set of starting values is determined in the strain plane, a path is obtained having its terminal point at an intersection with the boundary line. The sign of $\pm\,|d\epsilon|$ is selected so as to keep dx_b single valued, a physical necessity.

(IV) Boundary and Starting Conditions

Because the numerical work is made much easier, all integration will be started at the center of the disc and will progress outward.

(1) *Solid Center*

From the equilibrium Eq. (12) we see that $\sigma_t - \sigma_r = 0$ in order that stresses remain finite as $x_b \to 0$. This means in Eqs. (23) and (24) that $\phi_t = \phi_r$.

Using this in Eq. (16) gives

$$\epsilon = 2\epsilon_r = 2\epsilon_t \qquad (37)$$

at $x_b \to 0$.

To determine the starting increment of strain on the strain plane, we return to Eq. (13). Evaluating the indeterminate at $x_b \to 0$, making use of the fact that $\epsilon_r = \epsilon_t$, leads to

$$2d\epsilon_t = d\epsilon_r \qquad (38)$$

and using this in Eq. (30) finally results in

$$d\epsilon_t = (1/3)d\epsilon, \qquad d\epsilon_r = (2/3)d\epsilon \qquad (39)$$

at $x_b \to 0$. The evaluation of dx_b is obtained by differencing from a point x_{b1}, toward $x_b = 0$. In this backward difference we use the values of $d\epsilon_1$, $= -d\epsilon$, $d\epsilon_{r1} = -d\epsilon_r$, $d\epsilon_{t1} = -d\epsilon_t$, and $dD_1 = -dD$, the values of dD, $d\epsilon$ being determined from the $\sigma - \epsilon$ diagram and $d\epsilon_r$, $d\epsilon_t$ from Eq. (39). Using Eq. (28) leads to

$$3\epsilon_{r1}(dD_1/d\epsilon_{t1}) \approx A_1 + 2B_1$$

Substituting the values for A_1, B_1 from Eq. (29), considering $\phi_{r1} \approx \phi_{t1}$, and applying the compatibility equation to evaluate $x_{b1}/(\phi_{t1} - \phi_{r1})$, we have

$$x_{b1}D_1^2 J_1 \approx -3B_1\, d\epsilon_t + \phi_{r1}\, dD \qquad (40)$$

Eqs. (37) to (40) furnish all the necessary starting conditions for the solid center.

(2) *Free Edge*

Here we have the boundary condition of $\sigma_r = 0$ or

$$\phi_r = 0 \qquad (41)$$

x_b is chosen in an arbitrary fashion at the inner edge. By use of a normalizing procedure to be developed, we will see that this choice results in no loss in generality.

(3) *Rigid Edge*

This condition implies that the boundary suffers no change of radius or

$$\epsilon_t = 0 \qquad (42)$$

As above, an arbitrary choice of x_b is made.

(4) *General Edge Condition*

Any condition of stress or strain may be imposed at the boundaries and, with the aid of Eqs. (23) and (24), may be expressed in terms of strain alone.

(V) Strain Plane

Fig. 1 illustrates the strain plane, with the lines of constant ϵ/ϵ_{ti} being elliptical, the abscissa being ϵ_t/ϵ_{ti}, and the ordinate being ϵ_r/ϵ_{ti}. In order to keep the coordinates of the order of 1, the divisor ϵ_{ti} was used, this value being the tangential strain at the center of the disc. In the case of rigid center we use ϵ_{ri} instead of ϵ_{ti}, which is zero.

(VI) Normalization of T and x_b

x_b is defined as $(r + u)/b$, where b is undetermined. Let us further define

$$x_a = (r + u)/a, \qquad x_{a0} = 1 \qquad (43)$$

where a is merely the instantaneous outer radius. We then have

$$x_a = x_b/x_{b0} \qquad (44)$$

as the normalized instantaneous radius. To get the original radius, we use Eq. (36), which is written in terms of the normalized instantaneous radius as

$$r_a = x_a/e^{\epsilon_t} \qquad (45)$$

where $r_a = r/a$.

It will be seen from Eqs. (12), (29), and (31) that this normalization requires a change of T to

$$T_1 = \omega^2 a^2 \gamma/s_0$$

or

$$T_1 = x_{b0}^2 T \tag{46}$$

where we call T_1 the characteristic speed of the normalized disc.

(VII) Generalized Profile

Several methods[8] for analysis of the arbitrary profile have been discussed. The objective here is to evaluate

$$(d/dx_b)(\ln t_0)$$

Using Eq. (7), we have

$$dx_b/dr_b = e^{\epsilon_r}$$

Therefore,

$$\frac{d}{dx_b}(\ln t_0) = e^{-\epsilon_r}\frac{d}{dr_b}(\ln t_0) \tag{47}$$

For any special profile in which there appears $t_0 = f(r)$, Eq. (47) can be used directly.

In this respect a profile can be constructed, in a piecewise manner, either graphically or analytically.

A useful profile is

$$t_0 = \text{const.}, \quad 0 < r_b < r_1 \tag{48}$$

$$t_0 = e^{nr_b}, \quad r_1 < r_b < r_2 \tag{49}$$

$$t_0 = \text{const.}, \quad r_2 < r_b < r_0 \tag{50}$$

then,

$$\frac{d}{dx_b}(\ln t_0) = 0, \quad 0 < r_b < r_1$$

$$\frac{d}{dx_b}(\ln t_0) = ne^{-\epsilon_r}, \quad r_1 < r_b < r_2$$

$$\frac{d}{dx_b}(\ln t_0) = 0, \quad r_2 < r_b < r_0$$

which is a decreasing or increasing profile, depending on n, with a flat at the center and edge.

In this paper a second profile was studied. Let us take the most general case

$$t_0 = \rho q[1 - \sum_K A_k \beta^k]$$

where

$$\beta = (r_b - r_{bi}')/(c_b - r_{bi}')$$

with $c_b = c/b \geq 1$, r_{bi}' a constant.

A useful simplification is to take $A_k = \delta_k{}^n$, so that

$$t_0/q = \rho(1 - \beta^n) \tag{51}$$

Here, q is the thickness of the disc at $x_b = x_{bi}$ and ρ is a factor required to normalize t_0/q with reference to this position. From Eq. (51),

$$\frac{d}{dr_b}(\ln t_0) = \frac{n(r_b - r_{bi}')^{-1}}{1 - \left(\dfrac{c_b - r_{bi}'}{r_b - r_{bi}'}\right)^n}$$

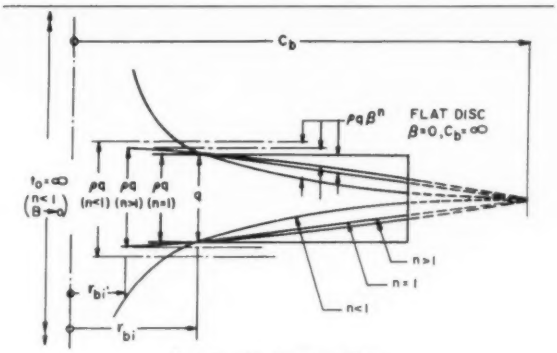

Fig. 2. Various profiles.

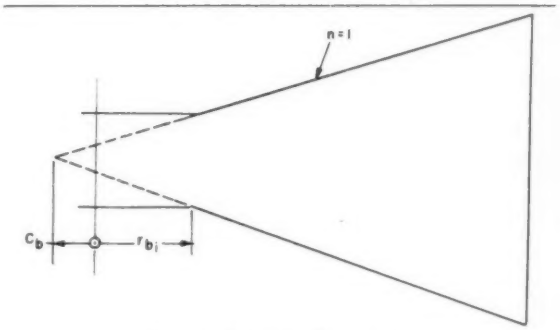

Fig. 3. Linear profile, $c_b < 0$.

Introducing this into Eq. (29) and using Eq. (18), we have

$$\frac{d}{dx_b}(\ln t_0) = \frac{ne^{-\epsilon_r}\left(\dfrac{x_b}{e^{\epsilon_t}} - \dfrac{x_{bi}'}{e^{\epsilon_{ti}'}}\right)^{-1}}{1 - \left(\dfrac{c_b - \dfrac{x_{bi}'}{e^{\epsilon_{ti}'}}}{\dfrac{x_b}{e^{\epsilon_t}} - \dfrac{x_{bi}'}{e^{\epsilon_{ti}'}}}\right)} \tag{52}$$

From Eq. (52) we see that the factors ρq do not appear in the solution, thus this solution is general with regard to thickness. Hence, it is sufficient to find the solution for a normalized thickness and multiply it by q for the actual disc.

To find the normalizing factor ρ, we need only set $t_0/q = 1$ at $x_b = x_{bi}$, or

$$\rho = 1/\left[1 - \left(\frac{\dfrac{x_{bi}}{e^{\epsilon_{ti}}} - \dfrac{x_{bi}'}{e^{\epsilon_{ti}'}}}{c_b - \dfrac{x_{bi}'}{e^{\epsilon_{ti}'}}}\right)\right] \tag{53}$$

Now $r_{bi}' = x_{bi}'/e^{\epsilon_{ti}'}$ is taken arbitrarily, and in this paper the only case investigated is $0 \leq r_{bi}' \leq r_{bi}$, with the special restriction of $r_{bi}' < r_{bi}$, for $n < 1$, in order to avoid infinite derivatives.

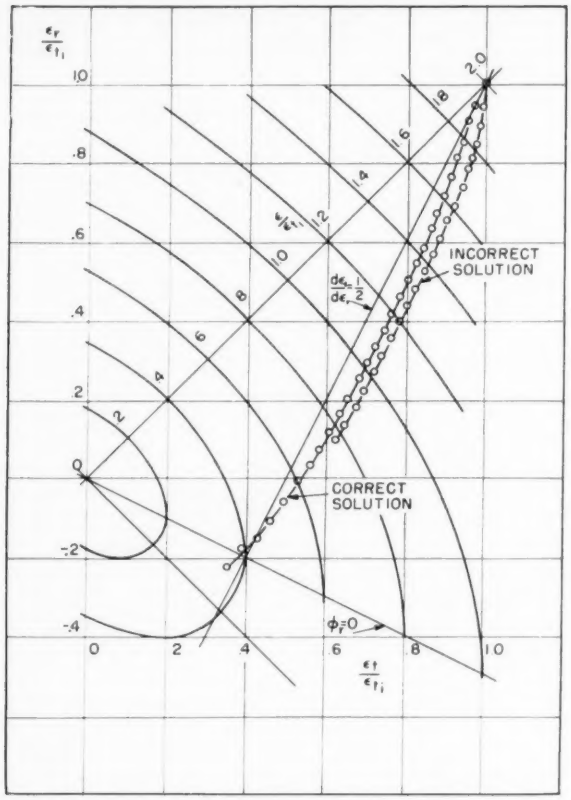

FIG. 4. Strain path for solutions with and without initial error, $\epsilon_i = 0.3348$, brass.

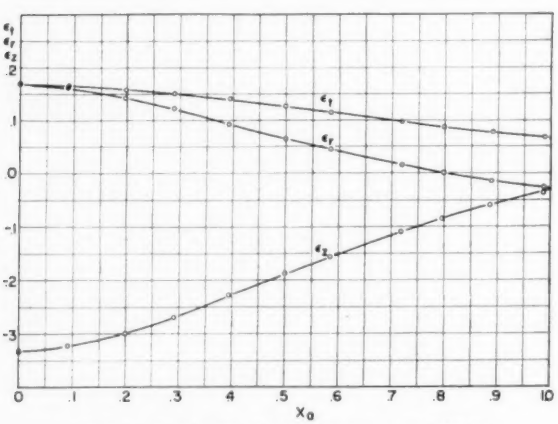

FIG. 5. Strain distribution, brass, $\epsilon_i = 0.3348$.

From Eq. (33) we see that, when $r_b = c_b$, there results $t_0/q = 0$, so that c_b is taken to be the measurement from the center of the disc to the vertex of the extended profile. This is illustrated in Figs. 2 and 3.

Now, for $c_b = \infty$, we have the flat profile. For $n = 1$, a linear variation of thickness with radius results. Then, since $\beta \leq 1$, we have $1 - \beta^n \leqslant 1 - \beta$, $n \leqslant 1$. With respect to the linear profile ($n = 1$), we see that $n < 1$ leads to a concave profile and $n > 1$ to a convex profile. Fig. 2 illustrates these profiles.

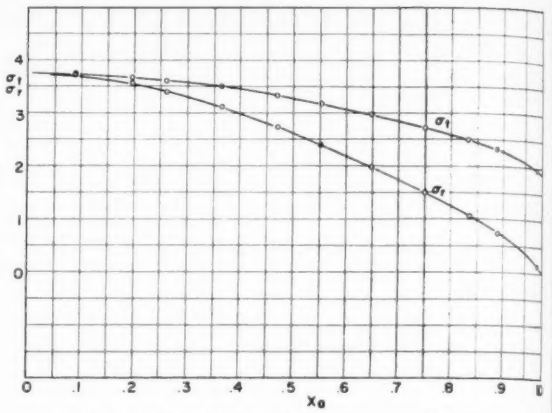

FIG. 6. Stress distribution, brass, $\epsilon_i = 0.3348$.

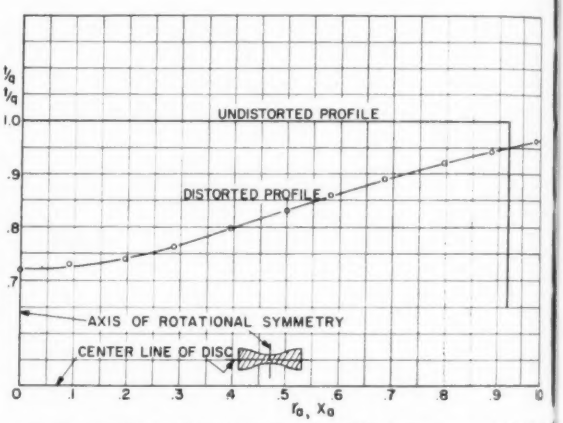

FIG. 7. Undistorted and distorted profile, brass, $\epsilon_i = 0.3348$.

For $c_b < r_{bi}'$, a profile with increased edge thickness results as shown in Fig. 3. Since this generally leads to a weaker disc, little attention was given to it.

(VIII) Special Solutions

In all the following solutions it is assumed that the disc is brought up to speed in such a manner as to keep the strain rate as nearly constant as possible. However, in many cases this will be of small concern, since there is usually small variance of the stress-strain curves with respect to strain rate.[9]

(1) *Solid Center and Stress-Free Outer Edge*

(*A*) *Brass.*—(*i*) *Flat disc:* The true stress-strain curve is shown in reference 8. For purposes of evaluation it is well to calculate $D = f(\epsilon)$ by use of Eq. (25), numerically smoothing this data to avoid erratic behavior in the difference equations.

Values of ϵ_i and T are then assumed, and the solution is obtained numerically with the aid of Eqs. (13) and (31). $T = 10$ is a convenient assumption. The use of a flat profile leads to d/dx_b (ln t_0) $= 0$ and the resultant simplification of J in Eq. (29). The starting condi-

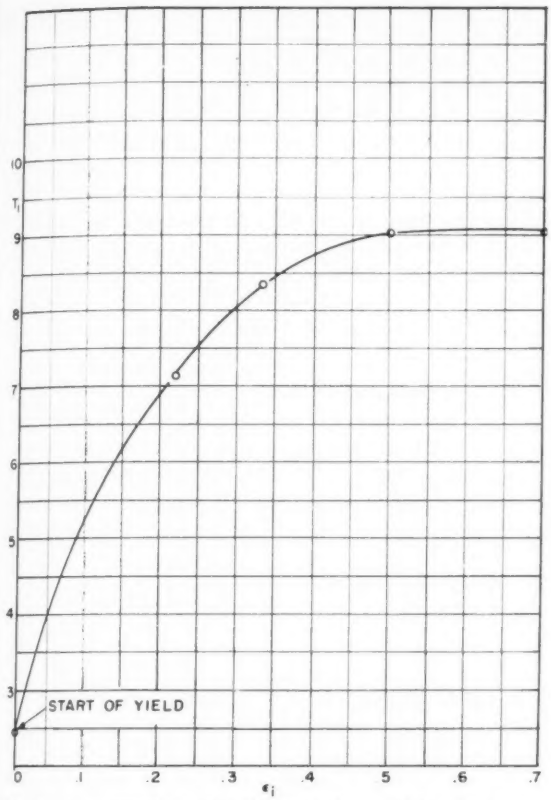

FIG. 8. T_1 vs. maximum effective strain in a solid flat disc, brass.

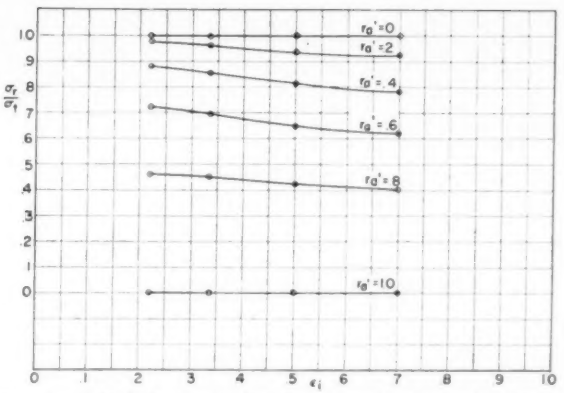

FIG. 9. Principal stress ratios of various elements as loading is increased.

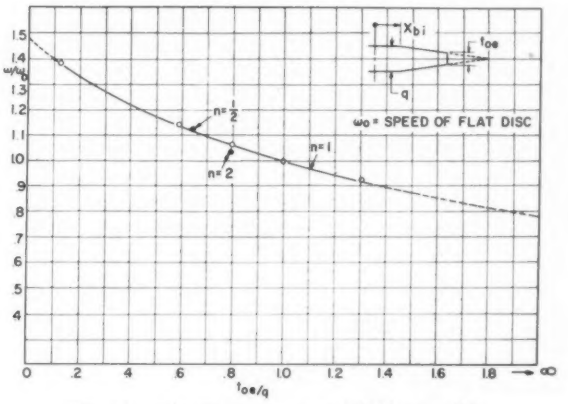

FIG. 10. ω/ω_0 vs. t_{0e}/q. $x_{bi} = 0.1916$, $\epsilon_i = 0.5$.

tions are given by Eqs. (39) and (40), and the final condition of $\phi_r = 0$ is shown in Fig. 1.

Fig. 4 illustrates a typical strain path, while Figs. 5, 6, and 7 show strain, stress, and half-profile distortion versus the normalized instantaneous radius. More results are shown in the original thesis.[8]

During the course of the investigation it was found that, if a small error were made at one point in the numerical evaluation the next line would compensate almost completely so as to wipe out this error. This happened so consistently that it is felt the equations must lead to a stable solution, which is important in numerical work. To test this idea, a large error was introduced early in the calculations, and the work was then correctly completed. Although the strain error did not completely vanish, the relative error in x_b did sensibly vanish. Since the most important quantity is T_1, which is only dependent on x_b, we can conclude that even a reasonably large error in calculations should not affect the final result adversely.

Fig. 8 is a plot of T_1 (normalized speed) versus the strain at the center of the disc (ϵ_i). Unrestrained plastic flow is taken to be the maximum value of T_1 or to occur when ϵ_i increases without an increase in speed. In the case considered, $T_1 \approx 9$.

Fig. 9 shows a plot of σ_r/σ_t vs. ϵ_i for elements at various initial radii. To derive this, it is first necessary to plot $r_{a'}$ vs. x_a, where a' is the initial outside radius of the disc. Then for various values of $r_{a'}$ = constant, x_a is obtained and, hence, the stress ratio at the particular ϵ_i. To evaluate $r_{a'}$, write $r_{a0}(a/a') = 1$. That is at the rim $r_0 = a'$, where $r_{a0} = r_0/a$. Then,

$$a/a' = (1/x_{a0})e^{\epsilon_{t0}} = e^{\epsilon_{t0}},$$

since $x_{a0} = 1$. But

$$r_a(a/a') = r_{a'} = x_a(e^{\epsilon_{t0}}/e^{\epsilon_t}) \tag{54}$$

Taking various values of $r_{a'}$ = constant for different ϵ_i (different loadings), we see in Fig. 9 that $\sigma_r/\sigma_t \approx$ constant and $\sigma_z/\sigma_t = 0$. Thus we expect the flow and deformation theories to yield nearly the same results.

(ii) Variable profile: In the variable profile and central hole solutions, it was decided to minimize the work by solving only for one ϵ_i. This allows for a more concise investigation of various profiles and inside to outside diameter ratios. In all cases a value of ϵ_i sufficiently large to ensure a bursting speed was taken. In an actual case this would finally be checked by taking a slightly larger and smaller ϵ_i to confirm this fact. Reference to Fig. 8 will show that this means ϵ_i must be large enough to make $T_1 \approx$ constant, independent

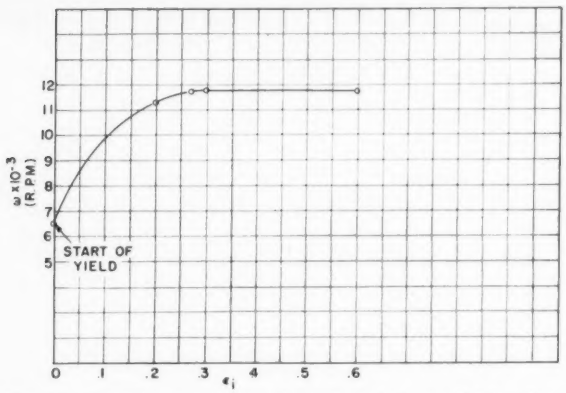

FIG. 11. Speed vs. maximum effective strain in a solid flat disc, steel.

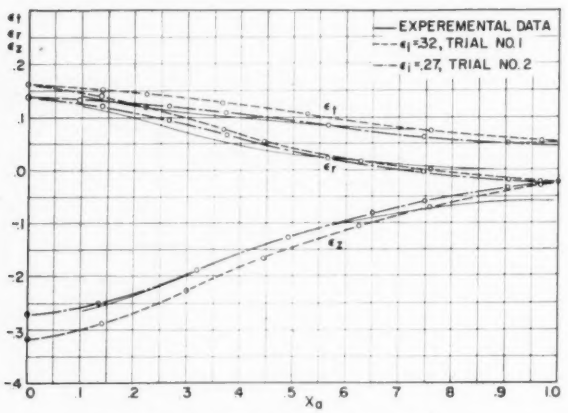

FIG. 12. Strain distributions, steel.

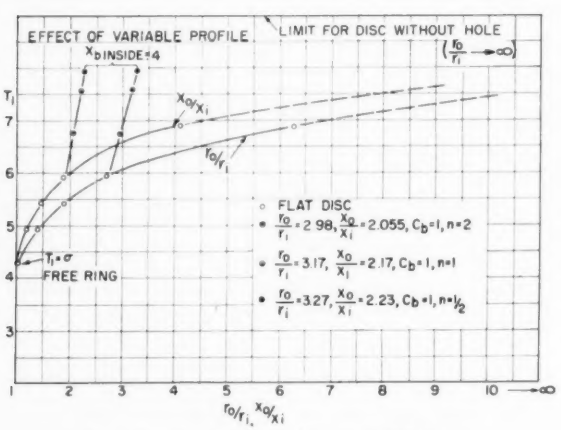

FIG. 13. T_1 vs. r_0/r_i, x_0/x_i. $\epsilon_i = 0.5$, brass.

of ϵ_i. With this in mind, $\epsilon_i = 0.5$ was selected for all solutions.

Fig. 10 indicates the results as ω/ω_0 vs. $t_{0\epsilon}/q$, where ω is the "bursting" speed of the variable profile, ω_0 is that of the flat disc, $t_{0\epsilon}$ is the rim thickness, and q is the center thickness. The curve applies to the linear case with two points for the concave ($n = 1/2$) and convex ($n = 2$) profiles. It is seen that the removal of metal closer to the rim increases the bursting speed.

(*B*) *Steel.*—Published in a paper by MacGregor and Tierney[10] are results of experimental work with high-speed rotating discs. Only flat discs were investigated, and one of them, identified as disc No. 11, had essentially the boundary conditions of solid center and stress-free outer edge. The material was steel, of which the average true stress-strain curve of many specimens is shown in Fig. 35 of reference 8. The disc diameter was 26 in., and the bursting speed was 11,800 r.p.m. Strain patterns of that paper are reproduced here for the purpose of comparison.

Fig. 11 shows a curve of $\omega \times 10^{-3}$ (r.p.m.) vs. ϵ_i with the speed for unrestrained flow being 11,700 r.p.m. This compares within 1 per cent of the experimental figure obtained. Fig. 12 compares the experimental and theoretical strain distribution. Other comparisons are given in reference 8.

(2) *Center and Edge Stress Free*

(*A*) *Brass.*—(*i*) *Flat disc and varied profile:* Fig. 13 illustrates the graph of T_1 vs. rim to hole ratio. The x_0/x_i is the instantaneous value, whereas r_0/r_i is in terms of the original radii. This graph includes the flat and variable profile. As with the discs lacking a central hole, the removal of metal increases the bursting speed. Also, there seems to be no stress concentrating effect, but instead the flat disc with central hole shows a definite tendency toward the solution for the disc without central hole as the hole diameter decreases.

Fig. 14 shows typical strain paths.

(*ii*) *Thin ring:* From Fig. 14, it is seen that, as the ring thickness decreases, the strain path decreases and becomes tangent to $\phi_r = 0$. This is also apparent from the fact that for the thin ring ϕ_r = constant throughout. Taken with the boundary conditions, $\phi_r = 0$ everywhere in the ring. Further, as in previous work, the integration is started at $\phi_r = 0$ and stopped as soon as it again reaches $\phi_r = 0$. Thus the strain path lies on the line $\phi_r = 0$ and is specified by two neighboring points that approach each other in the limit.

From the above and Eq. (28),

$$d\epsilon_r = (-A/B)d\epsilon_t$$

$$2\epsilon_r = -\epsilon_t \text{ (everywhere)}$$

Taking the differential of the second equation, we find

$$A/B = 1/2$$

Introducing this into Eq. (29), there finally results

$$Tx_b^2 = \epsilon_t/D = \epsilon/D = \sigma$$

But, from Eq. (46) and the fact that $x_{bi} = x_b = x_{b0}$,

$$T_1 = \omega^2 a^2 \gamma / s_0 = \sigma \qquad (55)$$

or

$$\omega^2 a^2 \gamma = s \tag{56}$$

where a is the instantaneous radius of the ring. For small strains, $a \rightarrow r$ and Eq. (56) reduces to the known equation for a thin ring.[3]

In order to find the original radius r, it is only necessary to use Eq. (36), which can be written as

$$a = re^{\epsilon} \tag{57}$$

while the change in thickness becomes

$$t/t_0 = e^{-\epsilon/2} \tag{58}$$

from Eq. (20) and assumption (2).

Eqs. (55) to (58) inclusive completely specify the free thin ring. As an example for $\epsilon = 0.5$, $x/r = 1.649$, $t/t_0 = 0.779$ and $T_1 = \sigma$.

(iii) Ideally plastic material: For this $\epsilon = D\sigma_0$, where σ_0 = constant = 1. Thus, $d\epsilon = dD$, which slightly simplifies the calculations. Examples have been worked for this case and are shown in detail in reference 8. Comparison with the small strain solution of Nadai and Donnell[2] shows similar stress and strain diagrams.

(3) *Residual Stresses*

The problem of finding residual stresses is usually complicated; however, if unloading and reloading is assumed to be perfectly elastic without a hysteresis loop and if the Bauschinger effect is ignored, these stresses can be evaluated. In this case, the residual stresses are equal to the plastic stress less the stress obtained by assuming elastic behavior of the disc at the same speed.

$$\sigma_{r'} = \sigma_p - \sigma_e \tag{59}$$

Only one such case was investigated, and this was taken for a disc that becomes flat at the prescribed speed. The elastic solution for this case is then greatly simplified and well known.[1]

For the plastic solution, t = constant will lead to further simplifications in the equilibrium equation and, hence, in the basic Eq. (31). These are basically in the coefficient of A and B. Such an analysis is shown in the original thesis.[8] Fig. 15 illustrates the result of a calculation for these stresses for brass with central strain $\epsilon_i = 0.22$.

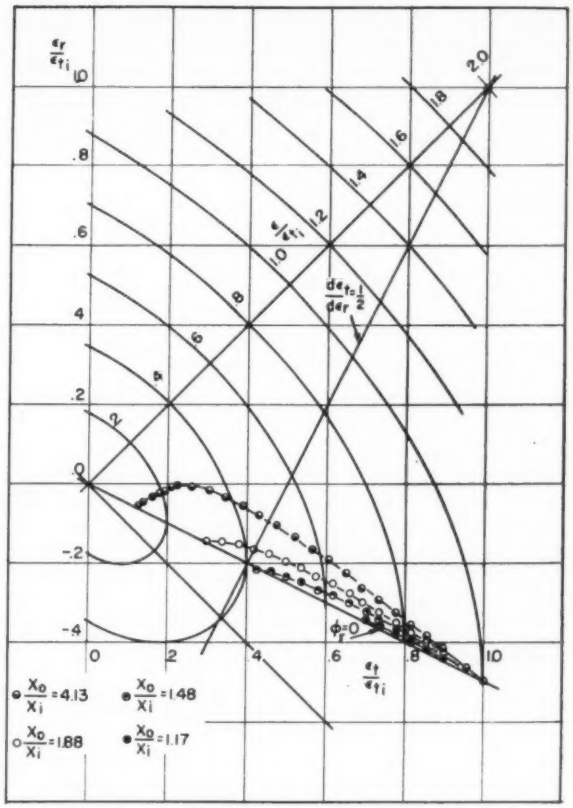

FIG. 14. Strain paths. Flat discs, brass.

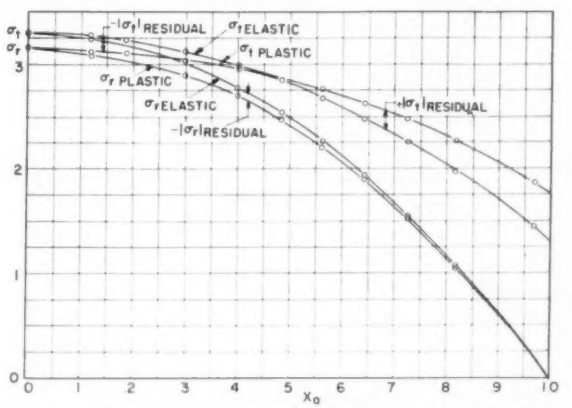

FIG. 15. Elastic, plastic, and residual stresses. t/q = 1, brass, $\epsilon_i = 0.22$.

REFERENCES

[1] Timoshenko, S. P., and Goodier, J. N., *Theory of Elasticity;* McGraw-Hill Book Company, Inc., New York, 1951.

[2] Nadai, A., and Donnell, L. H., *Stress Distribution in Rotational Disks of Ductile Material After the Yield Point Has Been Reached,* Transactions, ASME, APM-51-16, 1929.

[3] Nadai, A., *Theory of Flow and Fracture of Solids;* McGraw-Hill Book Company, Inc., New York, 1950.

[4] Hill, R., *The Mathematical Theory of Plasticity,* Oxford at the Clarendon Press, 1950.

[5] Hodge, P. G., Jr., *An Introduction to the Mathematical Theory of Perfectly Plastic Solids,* A11-SZ/396, Graduate Division of Applied Mathematics, Brown University, Providence, R.I., 1950.

[6] Zaid, M., *Partially Plastic Rotating Discs,* Journal of the Aeronautical Sciences, Vol. 19, No. 10, p. 697, October, 1952.

[7] Ludwick, P., *Elements der Technologischer Mechanik;* Verlag Julius Springer, Berlin, 1909.

[8] Zaid, M., *The Plastic Flow of Thin Rotating Discs with Large Strains,* Thesis for Sc.D. degree, M.I.T., 1951.

[9] MacGregor, C. W., and Fisher, J. C., *Tension Tests at Constant True Strain Rates,* Journal of Applied Mechanics, 45-A-8, 1945.

[10] MacGregor, C. W., and Tierney, W. D., *Developments in High Speed Rotating Disc Research at M.I.T.,* The Welding Journal Research Supplement, June, 1948.

An Investigation of the Flow About Cones and Wedges at and Beyond the Critical Angle

G. W. JOHNSTON*

Institute of Aerophysics, University of Toronto

SUMMARY

An experimental investigation has been carried out in the Institute of Aerophysics' 16- by 16-in. supersonic wind tunnel to determine the extent and general nature of the subsonic field produced ahead of wedge and cone models during bow-wave detachment and beyond, where the free-stream Mach Number lies in the supersonic régime. All tests were carried out at a nominal Mach Number of 2.5 under conditions of zero lift. The extent and growth, both lateral and forward, of the imbedded subsonic field has been measured for both models at the critical angle and beyond from a series of schlieren and shadow flow photographs. The general nature of the associated subsonic field was determined over the same range from a series of pressure distributions taken at the model surface and from the measured shock-wave geometry. The pressure measurements have also been used to determine the forebody pressure drag of cones and wedges at the detachment angle and throughout the critical position of the detached region. A method has been developed which allows a complete theoretical solution for the detached subsonic flow about a wedge model This method does not rely on a preliminary knowledge of the bow-wave geometry but is carried out in the hodograph plane.

The salient characteristics of the detached flow about both the cone and wedge models are shown in Fig. 1. These characteristics are similar to those occurring at transonic Mach Numbers.[1,2]

DISCUSSION

THE RESULTS OBTAINED for both models are qualitatively similar throughout; however, in all cases the flow changes introduced by wave detachment were found to be more violent (i.e., occur over a smaller range of model angles) for the two-dimensional wedge flow. It was found that the important parameters governing the position and growth of the subsonic field were S_2/t and S_3/t. It is noted that the parameter S_2/t (Fig. 2) decreases rapidly when the detachment angle is just moderately exceeded and then rapidly approaches a constant value. This confirms the theoretical prediction of Busemann[3] and others that the detached flow is, in fact, relatively insensitive to the conditions existing at the nose of the body (i.e., nose angle) so long as conditions are sufficiently far removed from the critical angle (defined as the body angle that just produces sonic conditions at the body surface). Hence, the important quantity governing the position of the subsonic field is the location of sonic velocity in the flow, and flow disturbances occurring near the position of sonic velocity (model shoulder) are thus relatively more important than similar disturbances occurring near the position of zero velocity (model nose).

The parameter S_1/t was found to increase throughout the whole range for both models used (see Fig. 2). The continued increase at the larger angles, from what has been said, must then be attributed to the movement of the model tip rather than a large movement of the bow wave itself. It was found that the lateral width of the subsonic field, $S3/t$, always increases rapidly just as the critical angle is exceeded and then soon approaches a constant value.

In conclusion, it was found that beyond the critical angle the subsonic field rapidly shrinks in the axial direction but grows, also rapidly, in the lateral direction. A stable position is approached for both models

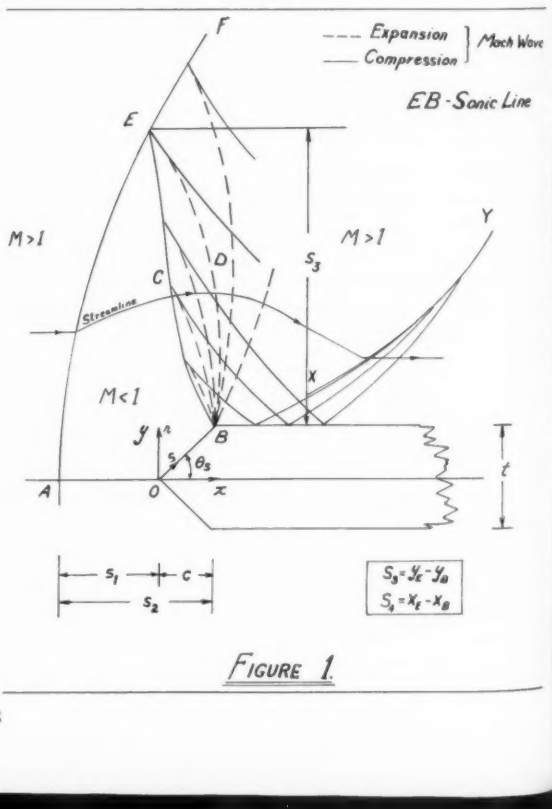

FIGURE 1.

Received February 23, 1953.

* Now Research Engineer, Ford Scientific Laboratory, Dearborn, Mich.

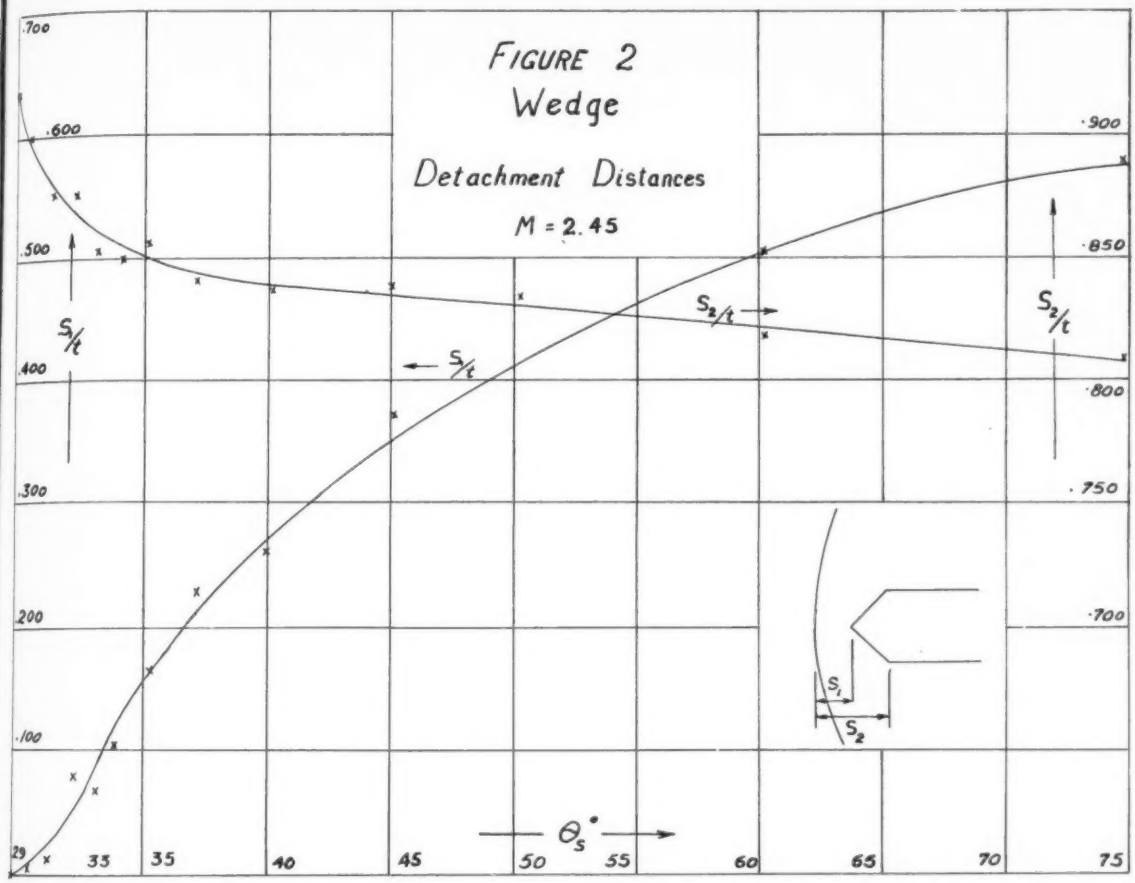

somewhat above the critical angle, so that no large change in the location of the subsonic field occurs in this region. This approach is more rapid in the two-dimensional case.

Along any given stream line in the subsonic field, it was found that the fluid particles encounter two distinct regions in which flow gradients exist. The magnitude of these gradients is greatest at the model surface and is rapidly attenuated at moderate distances from the model surface. Downstream from the bow wave, the fluid particles are first decelerated through a region of rising pressure. Next, the stream-line particle arrives at a position where the fluid pressure attains a maximum value. Finally, a region of falling pressure is encountered as the sonic line is approached.

From the pressure measurements taken with the wedge model, it was found (as had been theoretically predicted by Busemann) that the detachment process is a smooth and continuous one except in the neighborhood of the model tip, where flow changes were found to be violent (a much reduced velocity gradient exists during detachment at the cone tip). In fact, from the measurements that were taken, it was found that, at all positions of the model chord except the tip, the flow changes introduced during wave detachment (and beyond) are less severe than those occurring just before the critical angle is reached. It was found from the plotted distribution curves that the velocity in the immediate vicinity of the model leading edge, just as detachment begins, could be qualitatively expressed by

$$q_s = K_1 S^n$$

(see Fig. 1), where K_1 and n are positive constants with n less than unity. This type of velocity distribution is seen to be equivalent to that found in a sharp potential concave corner of angle $(180 - 2\theta s)$. Thus a simple analogy to the flow existing at the wedge tip, just at detachment, is possible. This qualitative formula indicates that the flow singularity at the tip possesses an infinite velocity and pressure gradient. The reason such a strong singularity may exist in a real fluid is due (it is believed) to the fact that the effect of the boundary layer at the extreme tip will be extremely small. Conceivably, the wedge angle may be altered slightly by the growth of the boundary layer, but the stream lines in the immediate vicinity of the tip must still retain an extremely small radius of curvature. Strong pressure gradients were also measured just ahead of the wedge corner once the flow became detached.

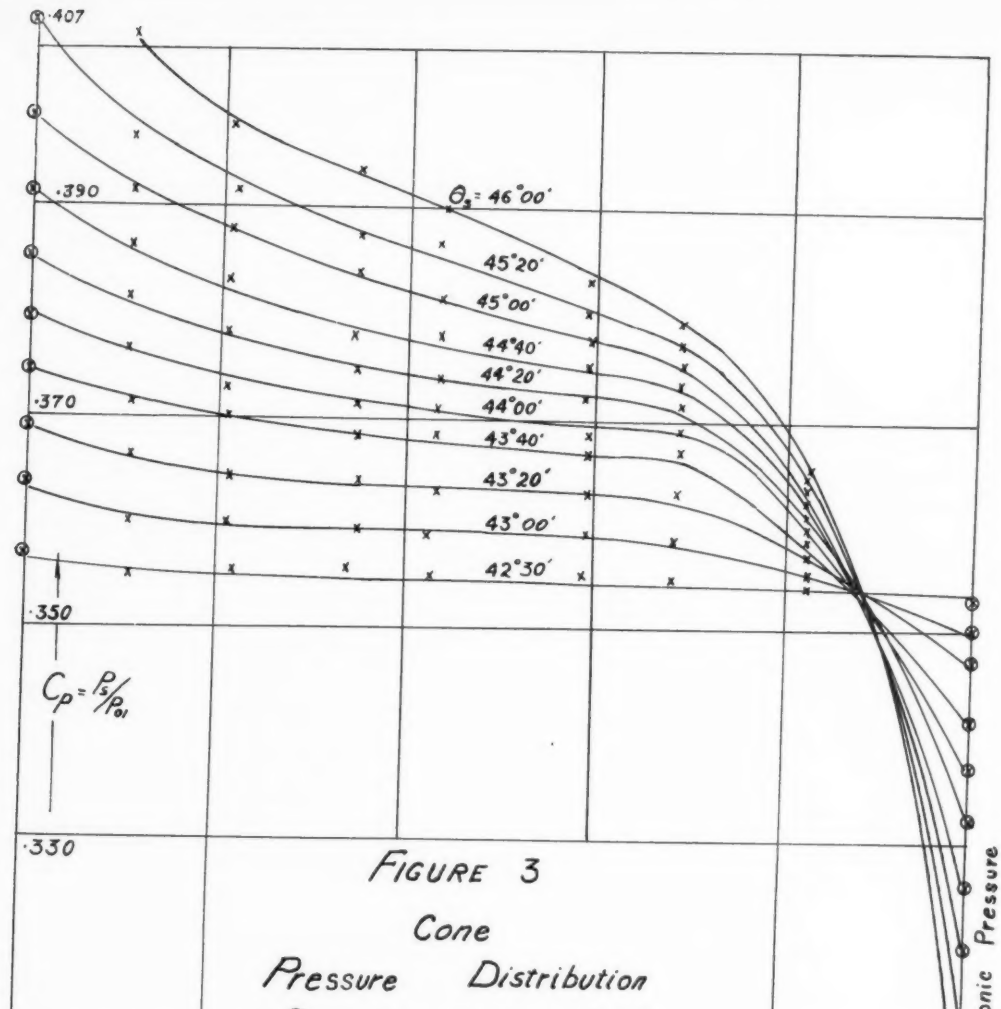

FIGURE 3
Cone
Pressure Distribution
Beyond the Critical Angle

The pressure distributions obtained during wave detachment with the cone model are shown in Fig. 3. The actual detachment angle for the cone model is of some interest, since a theoretical method of determining this angle does not exist at present. From the measurements, it was found that wave detachment does not occur until an angle slightly greater than θ_M is attained (θ_M being the maximum cone angle permitting an attached shock based on an infinite model chord). Thus detachment occurred at 46°, while θ_M was calculated as 45° 40′.

The pressure distributions (Fig. 3) indicate that conical flow (constant surface pressure) is maintained until sonic velocity is attained at the model surface (i.e., when the critical angle of 42° 30′ is reached). For all angles greater than the critical, the flow ahead of the model shoulder is affected by the presence of the shoulder and the effects of a finite chord are then felt.

The two end points of all pressure curves (Fig. 3) were obtained on the basis of the following assumptions: It was assumed that the pressure at the very tip would be identical to that on a model of infinite chord—

i.e., the expansion at the corner would not appreciably alter the pressure at the tip. (Since wave detachment is not complete throughout the range of angles shown, the tip does not experience stagnation conditions.) At the model corner it was assumed that sonic velocity was attained. The "fit" of the end points of the curves calculated in this manner with the remaining experimental points is seen to be good in all cases. It is noted that, as soon as the critical cone angle is exceeded, the shoulder of the model experiences decreasing pressure as the cone angle is increased (because of the increasing bow-wave curvature). The remainder of the model chord, however, experiences slowly increasing pressure as the detachment angle is approached. It is seen that, with the growth of the subsonic field, the deviations from conical flow become more pronounced at all positions of the model chord.

The pressure measurements taken were found to be, on the whole, relatively unaffected by the associated model boundary layer. It was found, however, that this layer can play an important role in the vicinity of the model corner. When no favorable potential pressure gradient acts on the boundary layer ahead of the wedge corner (i.e., before the critical angle is reached), the effective flow corner was moved ahead approximately 15 boundary-layer thicknesses. This effect is attributed to the rounding off of the geometric corner by the boundary layer and to the upstream propagation through the boundary layer of the low pressure encountered just downstream from the corner. Concerning this latter effect, little is known at the present time, so that even a rough check on the propagation distance cannot be made. It is known that moderate compression waves can be propagated upstream through a laminar boundary layer for distances equal to 20 times the above value.[4] (For the model used, the boundary layer at the shoulder was certainly laminar.) Once detachment occurred, however, this difficulty was avoided, and a pressure close to the actual sonic value was measured at the model shoulder. This fact is apparently explained by the development of a favorable potential pressure gradient on the boundary layer at the wedge corner by wave detachment.

The forebody pressure drag coefficient has been determined for both models in the neighborhood of the critical angle (Fig. 4). For both models this coefficient rises at an increasing rate as detachment approaches. At the detachment angle no sudden increase is obtained; rather, this angle appears as an inflection point on the drag curve. Thus the high-pressure region encountered at the tip of both models is confined to such a small portion of the model chord that no discontinuous drag rise occurs. For the finite cone model, a considerable reduction in drag coefficient is attained over that predicted for an infinite cone as soon as conical flow is destroyed.

The solution used for the detached flow about a wedge model is carried out in the hodograph plane.

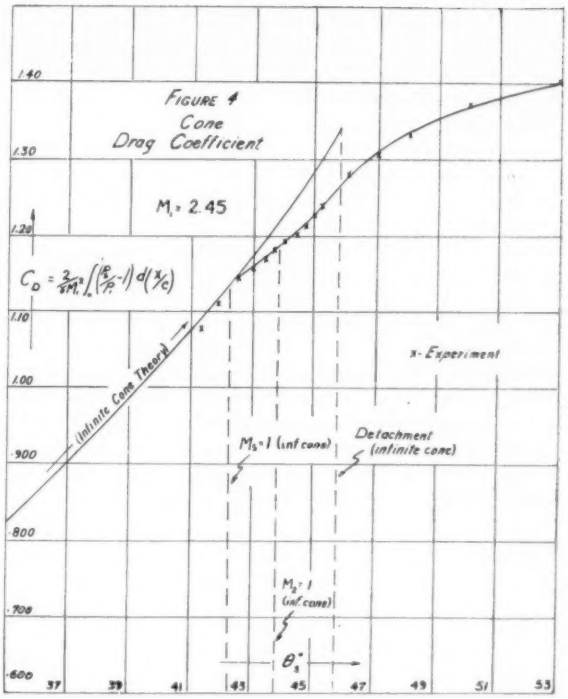

In this plane the boundary-value problem as originally proposed by Frankl[5] and Guderley[6] has been solved numerically. The stream function for the detached subsonic flow was found as a power series of the type

$$\psi(\tau, \theta) = \sum_n A_n \sin 2n\theta \tau^n y_n(\tau)$$

where

τ = (local velocity/limit velocity)^2
θ = inclination of velocity vector to wedge axis
$y_n(\tau)$ = hypergeometric integral
A_n = constants determined from the flow boundary conditions

The necessary constants A_n were obtained numerically from boundary conditions along the shock polar and along the supersonic expansion at the wedge shoulder. The supersonic boundary conditions are related to the subsonic-flow solution along the sonic line by means of an equation given originally by Tricomi.[7] This solution is only an approximate one, since only a limited number of constants A_n are determined for a corresponding number of prescribed boundary conditions. However, the accuracy may always be improved if required. The pressure distribution at the wedge surface calculated from a typical application of this method (using an eight-term expansion for ψ) was found to be in good agreement with that measured experimentally (Fig. 5). Further details on this entire problem may be obtained from reference 8.

References

[1] Liepmann, H. W., and Bryson, A. F., *Transonic Flow Past Wedge Sections*, Journal of the Aeronautical Sciences, Vol. 17, No. 12, p. 745, December, 1950.

[2] Griffith, W. C., *Transonic Flow*, Princeton University Technical Report II-7.

[3] Busemann, Adolf, *A Review of Analytical Methods for the Treatment of Flows with Detached Shocks*, N.A.C.A. T.N. No. 1858, 1949.

[4] Lee, J. D., *The Influence of High Adverse Pressure Gradients on Boundary Layers in Supersonic Flows*, U.T.I.A. Report No. 21, 1952.

[5] Frankl, F., *On the Problems of Chaplygin for Mixed Sub and Supersonic Flows*, N.A.C.A. T.M. No. 1155, 1947.

[6] Guderley, *Considerations of the Structure of Mixed Subsonic and Supersonic Flow Patterns*, Technical Report No. F-T.R. 2168-N.D., Air Materiel Command, October, 1947.

[7] Tricomi, *On Linear Partial Differential Equations of the Second Order of the Mixed Type*, Trans. A9-T-26, Graduate Division of Applied Mathematics, Brown University, 1948.

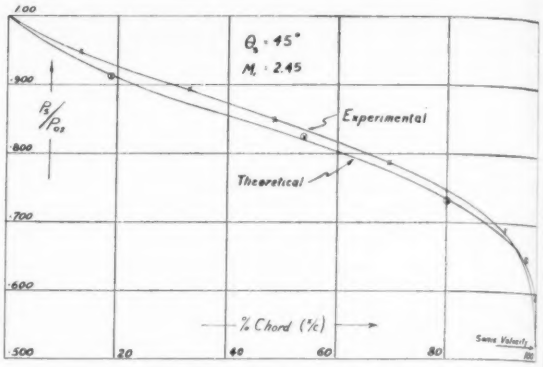

FIGURE 5 - Theoretical and Experimental Detached Wedge Pressure Distributions

[8] Johnston, G. W., *An Investigation of the Flow about Cones and Wedges At and Beyond the Critical Angle*, U.T.I.A. Report No. 24, December, 1952.

Changes of Address

Since the Post Office Department does not as a rule forward magazines to forwarding addresses, it is important that the Institute be notified of changes in address 30 days in advance of publishing date to ensure receipt of every issue of the JOURNAL and REVIEW.

Notices should be printed legibly and sent directly to:

Institute of the Aeronautical Sciences, Inc.
2 East 64th Street, New York 21, New York

IAS Twenty-Second Annual Meeting

Authors wishing to have papers considered for presentation at this meeting should submit outlines or short abstracts to the Meetings Committee, 2 East 64th St., New York 21, N.Y., no later than September 15, 1953.

The Upwash Correction for an Oscillating Wing in a Wind Tunnel*

THEODORE R. GOODMAN†

Cornell Aeronautical Laboratory, Inc.

SUMMARY

The upwash correction has been calculated for an oscillating three-dimensional wing in a circular wind tunnel at incompressible speeds. The upwash is given both at the wing itself and at downstream positions where, conceivably, a tail may be located. The tunnel upwash is calculated numerically for the entire frequency range.

SYMBOLS

φ = perturbation velocity potential
ω = frequency of oscillation
x, y, z = rectilinear coordinates (x in direction of free stream, y in spanwise direction)
u_0 = x component of perturbation velocity in $z = 0$ plane
l = typical tunnel dimension
Γ_k = circulation
k = reduced frequency $= \omega l/V$
V = free-stream velocity
$2s, 2c$ = wing span and chord, respectively
ψ = acceleration potential
ρ = free-stream density
A = wing area
C_L = lift coefficient $[= \text{lift}/(1/2)\rho V^2 A]$
r = radial dimension $(= \sqrt{y^2 + z^2})$
θ = cylindrical coordinate $(= \tan^{-1} y/z)$
δ = downwash parameter $[= (\partial\varphi_k^*/\partial z)(\pi l^2/A C_L)]$

NOTE: Other symbols of less importance are explained at the point where they are introduced.

INTRODUCTION

THE PROBLEMS WITH WHICH THIS PAPER is concerned have been attacked by two other writers to the author's knowledge. Jones[1] has solved the case of a finite-aspect-ratio wing placed at the center of a rectangular tunnel; Reissner[2] has solved the two-dimensional case.

The present report deals with a geometrical tunnel configuration hitherto unexplored—namely, the tunnel of circular cross section. It is a lifting wing that experiences the interference. In addition to finding the upwash correction at the wing itself, the upwash is also calculated at various tail positions downstream of the wing. The problems are solved under the assumptions of incompressibility and linearization of the equations of motion. The author has superficially explored the effects of compressibility, but the results are expressed in terms of untabulated functions of two variables. Moreover, the upwash downstream of the wing itself in a rectangular tunnel also involves untabulated functions of two variables even for incompressible flow. However, for the geometrical configuration with which this report is concerned, the upwash may readily be computed at the wing and at downstream positions.

One may ask the question: Under what conditions is it necessary to apply wind-tunnel wall corrections to an oscillating wing? The author has solved elsewhere[3] the case of the lifting wing midway between two vertical walls and also midway between two horizontal walls. In fact, the present paper is a condensation of reference 3. Now if the results of these two cases, as well as the present case (the circular tunnel), are considered to exemplify such corrections, a sufficient condition for applying these corrections is obtained in general—namely, if the corrections would not have been applied in the steady case, then for the nonsteady case of congruent geometry they need not be applied. The converse is not necessarily true, however. Again, taking the three cases as typical, it is found that, for the high frequencies encountered in flutter testing, the corrections are negligible, but for the low frequencies encountered in stability testing, the corrections are of the same order of magnitude as the steady corrections.

It should be emphasized that the reduced frequency, $\omega l/V$ encountered in wall corrections in general involves a length, l, which is a typical tunnel dimension (e.g., tunnel radius) and not a wing dimension (e.g., wing chord).

Among aeronautical engineers, it may be well to point out that the corrections here obtained involve the same assumptions (aside from nonsteady flow) as those obtained by Glauert.[4]

GENERAL CONSIDERATIONS OF ANALYSIS

For incompressible flow, the velocity potential φ satisfies Laplace's equation, $\Delta\varphi = 0$. Now let φ be the potential of the wing in free air, and let φ^* be the potential of the additional flow appearing because of the tunnel walls. Then, $\Delta\varphi^* = 0$. There must be no normal flow at the tunnel wall so that

$$(\partial/\partial n)(\varphi + \varphi^*) = 0 \qquad (1)$$

where n is the normal to the wall.

Received June 5, 1952.

* This work was performed under the sponsorship of the U.S. Air Force, Contract No. AF-33(038)-17848.

† Now on leave at Cornell University.

The first problem at hand is that of finding an expression for φ in the case of the oscillating wing which corresponds to a horseshoe vortex of zero span in the steady case. Since this is not general knowledge, a brief derivation will now follow.

Let $\varphi = \varphi_k(x, y, z)e^{i\omega t}$; then $\partial\varphi_k/\partial x$ may be represented according to lifting-surface theory by [see, for example, Eq. (57), reference 5]

$$\frac{\partial\varphi_k}{\partial x} = \frac{1}{2\pi}\int\int \frac{u_0 z\, d\xi d\eta}{[(x-\xi)^2 + (y-\eta)^2 + z^2]^{3/2}} \quad (2)$$

where integration extends over the wing and the wake and all lengths are made dimensionless by dividing by l, a typical tunnel dimension. From reference 5 the following equations are also obtained. In the wake

$$\varphi_k = (1/2)\Gamma_k(y)e^{-ik[x - x_t(y)]} \quad (3)$$

where

$$(1/2)\Gamma_k = \int_{x_l}^{x_t} u_0\, dx \quad (4)$$

and x_t, x_l are equations of the trailing and leading edges, respectively.

Now assume u_0 is constant and that the planform is rectangular (chord $= 2c$; span $= 2s$). Then from Eq. (4), Γ_k is constant and equal to

$$\Gamma_k = 4u_0 c \quad (5)$$

or

$$u_0 = \Gamma_k/4c \quad (6)$$

Differentiating Eq. (3) with respect to x, the expression for u_0 in the wake is

$$u_0 = -ik\Gamma_k e^{-ik(x-c)}/2 \quad (7)$$

Upon substituting Eqs. (6) and (7) into Eq. (2), there is obtained the following expression for $\partial\varphi_k/\partial x$ in space.

$$\frac{\partial\varphi_k}{\partial x} = \frac{z\Gamma_k}{8\pi c}\int_{-c}^{c} d\xi \int_{-s}^{s} \frac{d\eta}{[(x-\xi)^2 + (y-\eta)^2 + z^2]^{3/2}} - \frac{ikz}{4\pi}\Gamma_k e^{ikc}\int_{c}^{\infty} e^{-ik\xi}\, d\xi \int_{-s}^{s} \frac{d\eta}{[(x-\xi)^2 + (y-\eta)^2 + z^2]^{3/2}} \quad (8)$$

As $s \to 0$ and $c \to 0$, this reduces to

$$\frac{\partial\varphi_k}{\partial x} = \frac{s\Gamma_k z}{2\pi}\left\{\frac{1}{(x^2 + y^2 + z^2)^{3/2}} - ik\int_0^{\infty} \frac{e^{-ik\xi}\, d\xi}{[(x-\xi)^2 + y^2 + z^2]^{3/2}}\right\} \quad (9)$$

From this, it is readily ascertained that

$$\frac{\partial^2\varphi_k}{\partial x^2} + ik\frac{\partial\varphi_k}{\partial x} = \frac{-3s\Gamma_k x}{2\pi(x^2 + y^2 + z^2)^{5/2}} \quad (10)$$

Upon integrating with respect to x from $-\infty$ to x, there is obtained

$$\frac{\partial\varphi_k}{\partial x} + ik\varphi_k = \frac{s\Gamma_k z}{2\pi(x^2 + y^2 + z^2)^{3/2}} \quad (11)$$

Now define the acceleration potential, ψ, such that

$$\psi(x, y, z) = \frac{\partial\varphi_k}{\partial x}(x, y, z) + ik\varphi_k(x, y, z)$$

Solving this first-order differential equation with the condition that φ_k vanishes at $x = -\infty$, there is obtained

$$\varphi_k = \int_0^{\infty} e^{-ik\xi}\psi(x - \xi, y, z)\, d\xi \quad (12)$$

The acceleration potential for the oscillating doublet is clearly

$$\psi = s\Gamma_k z/2\pi(x^2 + y^2 + z^2)^{3/2} \quad (13)$$

It will be recognized that this expression is identical to the steady-state acceleration potential for a horseshoe vortex of zero span. If an acceleration potential ψ^* corresponding to φ^* is introduced, then it is easily seen that $\Delta\psi^* = 0$ and the boundary condition, Eq. (1), is also valid for the acceleration potential,

$$(\partial/\partial n)(\psi + \psi^*) = 0 \quad (14)$$

Hence, in order to solve the oscillating case, merely find the acceleration potential for the steady case of congruent geometry and then convert to velocity potential via Eq. (12).

Before proceeding to particular cases, it is necessary to find an expression for Γ_k in terms of the lift. By utilizing Eqs. (31) and (86) of reference 5, as well as Eq. (6) of the present report, there is found

$$\text{lift} = 2\rho V^2 l^2 s\Gamma_k(1 + ikc) \quad (15)$$

With the conventional definition of lift coefficient, there is found

$$s\Gamma_k = AC_L/4l^2(1 + ikc) \quad (16)$$

where A is the area of the wing. As $c \to 0$, this becomes

$$s\Gamma_k = AC_L/4l^2 \quad (17)$$

This is the well-known Kutta-Joukowski theorem for lift and is valid only to the first order in the chord in the nonsteady case.

It should be pointed out that the assumptions that the plan form is rectangular and u_0 constant are not essential to the results thus far obtained. The charac-

ter of the planform shape and u_0 distribution are lost when s and c are allowed to approach zero.

The Circular Tunnel

Fortunately, the steady-state acceleration potential, ψ^*, has already been obtained by von Baranoff[6] by Fourier integral analysis. The solution he obtains is (the notation has been made to conform with this report)

$$\psi^* = \frac{s\Gamma_k \cos\theta}{\pi^2} \int_0^\infty \cos qxI(qr) \frac{f(q)}{q}\, dq \tag{18}$$

where

$$f(q) = [qK_1(q) - q^2K_2(q)]/I_1'(q) \tag{19}$$

The Bessel functions appearing in Eqs. (18) and (19) are in conformity with the definitions given by Watson.[7] Also, the length, l, is taken as the tunnel radius.

Substituting Eq. (18) into Eq. (12), there is found, for the velocity potential,

$$\varphi_k^* = \frac{s\Gamma_k \cos\theta}{\pi^2} \int_0^\infty e^{-ik\xi}\, d\xi \int_0^\infty \cos q(x - \xi)I(qr) \frac{f(q)}{q}\, dq \tag{20}$$

The radial component of velocity is

$$\frac{\partial \varphi_k^*}{\partial r} = \frac{s\Gamma_k \cos\theta}{\pi^2} \int_0^\infty e^{-ik\xi}\, d\xi \int_0^\infty \cos q(x - \xi)I'(qr)f(q)\, dq \tag{21}$$

Writing $e^{-ik\xi} \cos k\xi - i \sin k\xi$ and after some manipulation, there is obtained, at the center of the tunnel $r = 0$, the upwash, as follows:

$$\frac{\partial \varphi_k^*}{\partial z} = \frac{s\Gamma_k}{4\pi^2} \int_0^\infty d\xi \left\{ \int_0^\infty \cos [qx + \xi(k - q)]f(q)\, dq + \int_0^\infty \cos [qx - \xi(k + q)]f(q)\, dq - i \int_0^\infty \sin [qx + \xi(k - q)]f(q)\, dq - i \int_0^\infty \sin [\xi(k + q) - qx]f(q)\, dq \right\} \tag{22}$$

Now each of these integrals may be simplified according to the Appendix, and the result is

$$\frac{\partial \varphi_k^*}{\partial z} = \frac{s\Gamma_k}{2\pi^2} \left[\frac{\pi}{2} f(k)e^{-ikx} + \int_0^\infty \frac{q \sin qxf(q)\, dq}{q^2 - k^2} + ik \int_0^\infty \frac{\cos qxf(q)\, dq}{q^2 - k^2} \right] \tag{23}$$

Let $s\Gamma_k = AC_L/4l^2$ according to Eq. (17) and define (see reference 4)

$$\delta = (\partial \varphi_k^*/\partial z)(\pi l^2/AC_L) \tag{24}$$

Then it is found that

$$\delta = \frac{1}{8} \left[\frac{f(k)}{2} e^{-ikx} + \frac{1}{\pi} \int_0^\infty \frac{q \sin qxf(q)\, dq}{q^2 - k^2} + \frac{ik}{\pi} \int_0^\infty \frac{\cos qxf(q)\, dq}{q^2 - k^2} \right] \tag{25}$$

at the wing ($x = 0$), this becomes

$$\delta = \frac{1}{8} \left[\frac{f(k)}{2} + \frac{ik}{\pi} \int_0^\infty \frac{f(q)\, dq}{q^2 - k^2} \right] \tag{26}$$

For purposes of numerical integration, it is convenient to rewrite Eqs. (25) and (26), respectively, as follows:

$$\delta = \frac{1}{8} \left[f(k)e^{-ikx} + \frac{1}{\pi} \int_0^\infty \frac{q \sin qx[f(q) - f(k)]\, dq}{q^2 - k^2} + \frac{ik}{\pi} \int_0^\infty \frac{\cos qx[f(q) - f(k)]}{q^2 - k^2} \right] \tag{27}$$

$$\delta = \frac{1}{8} \left[\frac{f(k)}{2} + \frac{ik}{\pi} \int_0^\infty \frac{[f(q) - f(k)]\, dq}{q^2 - k^2} \right] \tag{28}$$

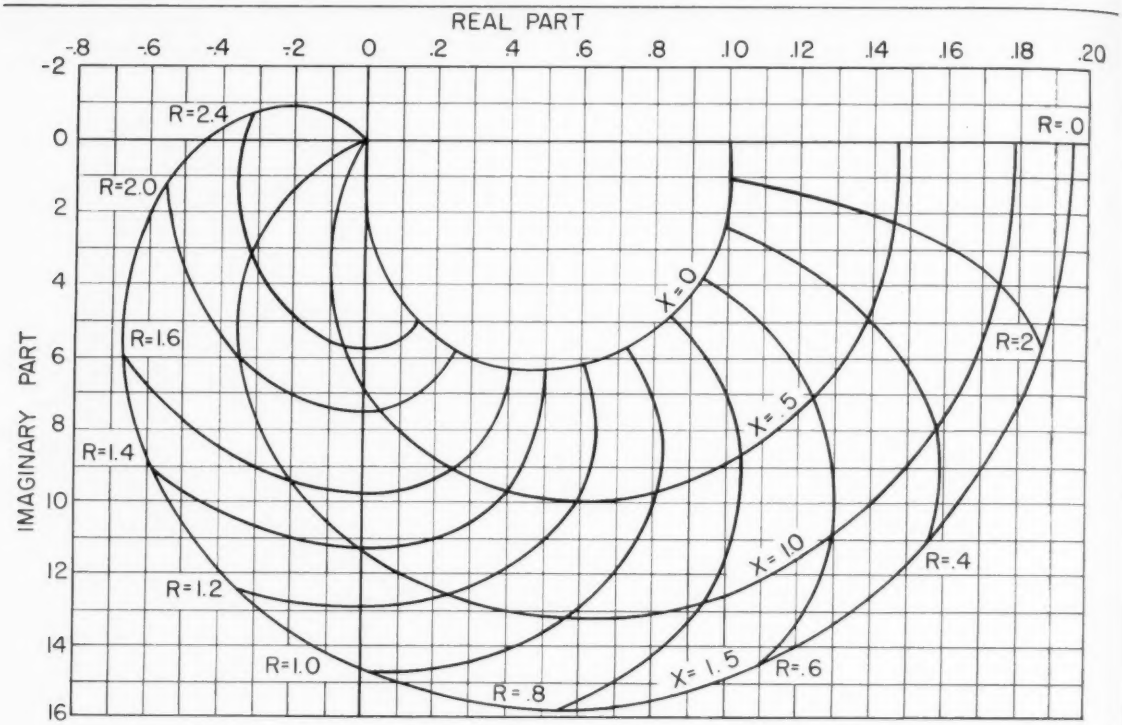

FIG. 1. Complex upwash (8δ) at wing and tail positions over the frequencey spectrum.

There is a theorem derived by Riemann[8] from which it can be shown that as $x \to \infty$, the integrals appearing in Eq. (27) vanish. Hence, if one were to make a graph in which the abscissa is the real part of δ and the ordinate the imaginary part, then, for large x, δ would appear as a circle with radius $f(k)/8$. Such a graph is given in Fig. 1 for a useful variation of x and k. Instead of δ, however, 8δ is charted so that, for $x = 0$ and $k = 0$, the value is unity. This value is in agreement with that obtained by Glauert[4] for this case.

REFERENCES

[1] Jones, W. Prichard, *Wind Tunnel Interference Effect on the Values of Experimentally Determined Derivative Coefficients for Oscillating Aerofoils*, British R. & M. No. 1912, 1943.

[2] Reissner, Eric, *Wind Tunnel Corrections for the Two-Dimensional Theory of Oscillating Airfoils*, Cornell Aeronautical Laboratory Report No. SB-318-S-3, 1947.

[3] Goodman, Theodore R., *The Upwash Correction for an Oscillating Wing in a Wind Tunnel*, Cornell Aeronautical Laboratory Report No. AD-744-W-1, July, 1951.

[4] Glauert, H., *The Elements of Aerofoil and Airscrew Theory*, pp. 189–198; The Macmillan Company, New York, 1944.

[5] Reissner, Eric, *On the General Theory of Thin Airfoils for Non-Uniform Motion*, NACA TN No. 946, 1944.

[6] von Baranoff, A., *Zur Frage der Kanalkorrektur bei kompressibler Unterschallströmung*, Deutsche Luftfahrtforschung, Forschungsbericht, Nr. 1272, 1940. (Also appears in English translation as: *Tunnel Correction for Compressible Subsonic Flow*, NACA TM No. 1162, 1947.)

[7] Watson, G. N., *A Treatise on the Theory of Bessel Functions*, 2nd Ed.; The Macmillan Company, New York, 1945. (In particular, see pp. 172, 416, and 537–550.)

[8] Franklin, Philip, *A Treatise on Advanced Calculus*, pp. 480–481; John Wiley & Sons, Inc., New York, 1940.

[9] Whittaker, E. T., and Watson, G. N., *A Course of Modern Analysis*, 4th Ed., pp. 73–74; Cambridge University Press, 1940.

APPENDIX

This section is devoted to the simplification of integrals which are of the form

$$\int_0^\infty d\xi \int_0^\infty \begin{Bmatrix} \sin (q \pm k)\xi \\ \cos (q \pm k)\xi \end{Bmatrix} f(q)\, dq$$

A theorem on Riemann integration[9] justifies the writing of this as

$$\lim_{\mu \to 0} \int_0^\infty e^{-\mu\xi}\, d\xi \int_0^\infty \begin{Bmatrix} \sin (q \pm k)\xi \\ \cos (q \pm k)\xi \end{Bmatrix} f(q)\, dq$$

The order of integration may be interchanged and the integration on ξ performed. There is then obtained

$$\lim_{\mu \to 0} \int_0^\infty \frac{f(q) \begin{Bmatrix} q \pm k \\ \mu \end{Bmatrix} dq}{\mu^2 + (q \pm k)^2}$$

If $q \pm k$ appears in the numerator, then, as $\mu \to 0$, this becomes

(*Concluded on page 406*)

Stress Analysis of Sheet-Stringer Panels with Cutouts*

HARVEY G. McCOMB, JR.†

Langley Aeronautical Laboratory, NACA

ABSTRACT

A method is presented for determining the stresses in axially loaded sheet-stringer panels having cutouts. The method is based on the use of so-called "unit perturbation" solutions that are appropriately superposed to give the effects of the cutout on the stress distribution that would exist with no cutout. The analysis of stringer reinforcements and doubler plates is carried out in a similar fashion.

SYMBOLS

A	= cross-sectional area of stringers
B	= $(E/G)\,(A/bt)\,(b^2/L^2)$
E	= Young's modulus of elasticity
G	= shear modulus of elasticity
L	= distance between ribs
P_{ij}	= stringer load at station ij (the intersection of stringer j and rib i), positive in tension
$P_{ij}(k, l)$	= stringer load at station i, j due to a concentrated unit perturbation load at station k, l
$P_{ij}[k, l]$	= stringer load at station i, j due to a unit shear perturbation load about shear panel k, l
$P_{ij}\{k, l\}$	= stringer load at station i, j due to a distributed unit perturbation load on stringer l between rib k and rib $k + 1$
b	= distance between stringers
i, j	= indices for stringers, ribs, and shear panels; i horizontal and j vertical
k, l	= general integers
$\bar{p}_{kl}$	= concentrated perturbation load (lbs.) applied at station k, l
$\bar{q}_{kl}$	= distributed perturbation load (lbs. per in.) applied to stringer l between ribs k and $k + 1$
$\bar{q}_{kl}$	= shear perturbation load (lbs. per in.) applied about shear panel k, l
q_{ij}	= shear flow in panel i, j
$q_{ij}(k, l)$	= shear flow in shear panel i, j due to a concentrated unit perturbation load at station k, l
$q_{ij}[k, l]$	= shear flow in shear panel i, j due to a unit shear perturbation load about shear panel k, l
$q_{ij}\{k, l\}$	= shear flow in shear panel i, j due to a distributed unit perturbation load on stringer l between rib k and rib $k + 1$
t	= thickness of sheet
t'	= thickness of the additional portion of a reinforced shear panel
$\overline{P}$	= external load per stringer applied to a tension panel
δ_{jl}	= Kronecker delta, takes the value 1 when $j = l$ and takes the value 0 when $j \neq l$
$\gamma(x)$	= $[-3B + 2(\cos x - 1)]/[3B + (\cos x - 1)]$
$\lambda(x)$	= $\cosh^{-1}\lvert\gamma(x)\rvert$
μ_{ij}	= Lagrangian multiplier
π^*	= complementary energy
ρ_{ij}	= $P_{i+1,\,j} + 4\,P_{ij} + P_{i-1,\,j}$
Δ_{ii}, Δ_{jj}	= operators indicating the second difference in the i and j directions, respectively

INTRODUCTION

STRESS CONCENTRATIONS occur in the neighborhood of cutouts in semimonocoque structures. Analysis of these stress concentrations is beyond the scope of elementary theories, and the development of more powerful methods has been in progress for a number of years. The solution of the cutout in a flat sheet stiffened longitudinally with stringers and transversely with ribs is of interest not only for the stress analysis of such simplified structures but also for the fact that it may indicate methods of analysis for the cutout in more general types of semimonocoque structures.

An approximate solution for cutouts in axially loaded skin-stringer panels is presented in references 1 and 2. This solution is based on the shear lag theory of Kuhn. In reference 3, this type of analysis is extended to the case where the coaming stringers, the stringers bordering the cutout, are reinforced. In reference 4, a solution is obtained for a cutout in the center bay of a three-bay panel under plane loading.

This report presents a different approach to the stress analysis of cutouts in flat stiffened sheet under axial load. The fundamental idea is that the final stress distribution in the structure is a superposition of (a) the stress distribution that would exist in the structure if there were no cutout and (b) the stress perturbations due to the cutout. This concept was suggested by Cicala.[5]

The method can account for the effects of reinforcing the stringers bounding the cutouts—the so-called coaming stringers—and of reinforcing shear panels around the cutout.

BASIC ASSUMPTIONS

The structure to be considered is illustrated in Fig. 1. It consists of a thin flat sheet stiffened by stringers in longitudinal direction and by ribs in the transverse direction. The cutout is located in the center of the panel. It removes an arbitrary number of shear panels

Presented at the Structures Session, Twenty-First Annual Meeting, I.A.S., New York, January 26–29, 1953.

* The author acknowledges the assistance of the following members of the Structures Research Division, NACA: Dr. John E. Duberg, who initiated this investigation, and Dr. Bernard Budiansky.

† Aeronautical Research Scientist.

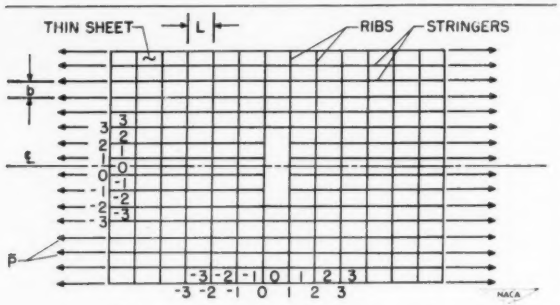

FIG. 1. Cutout in skin-stringer panel.

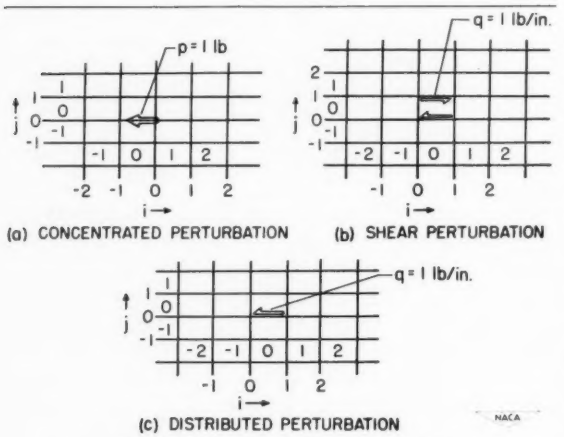

FIG. 2. Types of perturbation loads.

and interrupts the corresponding number of stringers and is not limited to one bay in length. The loading is axial and uniform at the ends of the panel. The following assumptions are made:

(a) The ribs prevent transverse displacements of the sheet, but they offer no restraint to longitudinal displacements of the stringers.

(b) The stringers have zero bending stiffness and finite axial stiffness.

(c) The cross-sectional area of the stringers and the thickness of the sheet are constant.

(d) The sheet carries only shear stresses, and the stringers carry only direct stresses.

(e) The shear flow in each shear panel is constant throughout that panel.

As a result of assumption (e), the variation of direct stress in the stringers is linear between rib stations. The relationship between this structural model and an actual panel will be discussed later.

METHOD OF ANALYSIS

The final stress distribution in a sheet-stringer panel with a cutout can be thought of as a superposition of the stress distribution that would exist in the panel without the cutout and certain perturbation stress distributions that arise because of the cutout. The first step in the analysis, then, is to consider the structure as though it did not have a cutout—the "basic" structure. The stress distribution that exists in the basic structure because of the external loads will be called the "basic" stress distribution. The second step in the analysis is to superpose perturbation stress distributions on the basic stress distribution in the basic structure in such a way as to annihilate the effects of that portion of the basic structure which lies within the cutout.

The Unit Perturbation Solutions

Three types of perturbation stress distributions provide the necessary tools for this method of analyzing rectangular cutouts in sheet-stringer panels with or without reinforcement. These perturbation stress distributions are: (1) the stress distribution caused by a concentrated force, $p = 1$, applied to a stringer at its intersection with a rib and acting in the direction of the stringer, Fig. 2(a); (2) the stress distribution caused by a uniformly distributed shear flow, $q = 1$, applied to the stringers bordering one shear panel in such a way as to cause shear in the panel, Fig. 2(b); and (3) the stress distribution due to one uniformly distributed shear flow, $q = 1$, applied to a stringer between two ribs, Fig. 2(c). For identification, these three types of loadings will be called, respectively, the concentrated perturbation loading, the shear perturbation loading, and the distributed perturbation loading. Note that the shear perturbation stress distribution is simply a superposition of the stress distribution due to two distributed perturbation loads, one on either side of a shear panel.

Solutions have been obtained for these perturbation loadings applied to a sheet-stringer panel that extends to infinity in both directions. Derivations of the stress distributions due to concentrated and distributed perturbation loadings are given in the Appendix, and the shear perturbation solution is obtained by superposing two distributed perturbation solutions. The perturbation solutions depend on one parameter only, defined as $B = (E/G)\,(A/bt)\,(b^2/L^2)$. The perturbation solutions for values of B equal to 3, 5, 7, 9, and 11 are given in Tables 1 to 5. Part (a) of each table contains the values of P_{ij} and $q_{ij}L$ due to a concentrated unit perturbation load $p = 1$ at station (0, 0), where P_{ij} is the stringer load at station (i, j)—the intersection of stringer j and rib i—and q_{ij} is the shear flow in panel (i, j)—the shear panel having station (i, j) in its lower left-hand corner [see Fig. 2(a)]. Part (b) of each table gives the values of P_{ij}/L and q_{ij} due to a distributed unit perturbation $q = 1$ between stations (0, 0) and (1, 0) [see Fig. 2(c)]; part (c) of each table gives P_{ij}/L and q_{ij} due to a unit shear perturbation $q = 1$ on shear panel (0, 0) [see Fig. 2(b)].

The positive direction of the concentrated, distributed, and shear perturbation loads are as shown in

TABLE 1(a)

Perturbation Distribution Due to Concentrated Unit Perturbation Load At Station (0,0)

B = 3

Stringer Loads: P_{ij}

j	i = 0	1	2	3	4
0	0.5000	0.2507	0.1165	0.0778	0.0723
1	0	0.0674	0.0748	0.0674	0.0580
2	0	0.0216	0.0343	0.0390	0.0393
3	0	0.0101	0.0181	0.0232	0.0259
4	0	0.0058	0.0109	0.0149	0.0177
5	0	0.0038	0.0073	0.0103	0.0126
6	0	0.0027	0.0052	0.0075	0.0094
7	0	0.0020	0.0039	0.0057	0.0073
8	0	0.0016	0.0031	0.0045	0.0059
9	0	0.0013	0.0025	0.0037	0.0048
10	0	0.0011	0.0021	0.0031	0.0041
11	0	0.0009	0.0018	0.0027	0.0035
12	0	0.0008	0.0016	0.0023	0.0031

Panel Shears: q_{ij}

j	i = 0	1	2	3
0	0.1246	0.0521	0.0243	0.0128
1	0.0572	0.0448	0.0317	0.0221
2	0.0356	0.0321	0.0270	0.0212
3	0.0255	0.0262	0.0218	0.0172
4	0.0197	0.0190	0.0178	0.0154
5	0.0159	0.0156	0.0149	0.0140
6	0.0132	0.0130	0.0126	0.0120
7	0.0112	0.0111	0.0108	0.0104
8	0.0096	0.0096	0.0094	0.0091
9	0.0084	0.0083	0.0082	0.0080
10	0.0073	0.0073	0.0072	0.0070
11	0.0064	0.0064	0.0063	0.0062
12	0.0056	0.0056	0.0055	0.0055

TABLE 1(b)

Perturbation Distribution Due to Distributed Unit Perturbation Load On Stringer 0 In Bay 0

B = 3

Stringer Loads: $\frac{P_{ij}}{L}$

j	i = 1	2	3	4
0	0.3578	0.1920	0.1195	0.0839
1	0.0416	0.0732	0.0714	0.0627
2	0.0115	0.0288	0.0372	0.0394
3	0.0052	0.0143	0.0209	0.0248
4	0.0029	0.0084	0.0130	0.0164
5	0.0019	0.0056	0.0088	0.0115
6	0.0013	0.0040	0.0064	0.0085
7	0.0010	0.0030	0.0048	0.0065
8	0.0008	0.0023	0.0038	0.0052
9	0.0006	0.0019	0.0031	0.0043
10	0.0005	0.0016	0.0026	0.0036
11	0.0004	0.0014	0.0022	0.0031
12	0.0004	0.0012	0.0019	0.0027

Panel Shears: q_{ij}

j	i = 0	1	2	3
0	0.1422	0.0829	0.0363	0.0178
1	0.0589	0.0514	0.0380	0.0266
2	0.0359	0.0341	0.0296	0.0244
3	0.0256	0.0249	0.0230	0.0205
4	0.0197	0.0194	0.0185	0.0171
5	0.0159	0.0158	0.0152	0.0144
6	0.0132	0.0131	0.0128	0.0123
7	0.0112	0.0112	0.0110	0.0106
8	0.0097	0.0096	0.0095	0.0092
9	0.0084	0.0084	0.0083	0.0080
10	0.0073	0.0073	0.0072	0.0071
11	0.0064	0.0064	0.0064	0.0062
12	0.0056	0.0056	0.0056	0.0055

TABLE 1(c)

Perturbation Distribution Due to Unit Shear Perturbation Load About Shear Panel (0,0)

B = 3

Stringer Loads: $\frac{P_{ij}}{I}$

j \ i	1	2	3	4
1	-0.3162	-0.1188	-0.0480	-0.0212
2	-0.0302	-0.0444	-0.0343	-0.0233
3	-0.0063	-0.0145	-0.0163	-0.0146
4	-0.0022	-0.0059	-0.0079	-0.0084
5	-0.0010	-0.0029	-0.0042	-0.0049
6	-0.0006	-0.0016	-0.0024	-0.0030
7	-0.0003	-0.0010	-0.0015	-0.0020
8	-0.0002	-0.0006	-0.0010	-0.0013
9	-0.0001	-0.0004	-0.0007	-0.0009
10	-0.0001	-0.0003	-0.0005	-0.0007
11	-0.0001	-0.0002	-0.0004	-0.0005
12	0.0000	-0.0002	-0.0003	-0.0004

Panel Shears: q_{ij}

j \ i	0	1	2	3
0	-0.2844	-0.1558	-0.0725	-0.0356
1	-0.0833	-0.0315	-0.0117	-0.0088
2	-0.0330	-0.0173	-0.0084	-0.0022
3	-0.0203	-0.0092	-0.0066	-0.0039
4	-0.0059	-0.0055	-0.0046	-0.0034
5	-0.0038	-0.0036	-0.0032	-0.0027
6	-0.0027	-0.0026	-0.0024	-0.0021
7	-0.0020	-0.0020	-0.0019	-0.0017
8	-0.0016	-0.0016	-0.0015	-0.0014
9	-0.0013	-0.0013	-0.0012	-0.0012
10	-0.0011	-0.0010	-0.0010	-0.0010
11	-0.0009	-0.0009	-0.0009	-0.0008
12	-0.0008	-0.0008	-0.0008	-0.0008

TABLE 2(a)

Perturbation Distribution Due to Concentrated Unit Perturbation Load at Station (0,0)

B = 5

Stringer Loads: P_{ij}

j \ i	0	1	2	3	4
0	0.5000	0.2913	0.1853	0.1283	0.0955
1	0	0.0590	0.0738	0.0724	0.0662
2	0	0.0175	0.0297	0.0364	0.0390
3	0	0.0080	0.0148	0.0200	0.0236
4	0	0.0045	0.0087	0.0123	0.0152
5	0	0.0030	0.0058	0.0083	0.0105
6	0	0.0021	0.0041	0.0060	0.0077
7	0	0.0016	0.0031	0.0045	0.0059
8	0	0.0012	0.0024	0.0036	0.0047
9	0	0.0010	0.0020	0.0029	0.0038
10	0	0.0008	0.0016	0.0024	0.0032
11	0	0.0007	0.0014	0.0021	0.0028
12	0	0.0006	0.0012	0.0018	0.0024

Panel Shears: $q_{ij}L$

j \ i	0	1	2	3
0	0.1044	0.0530	0.0285	0.0164
1	0.0453	0.0383	0.0298	0.0226
2	0.0278	0.0260	0.0232	0.0200
3	0.0198	0.0192	0.0180	0.0165
4	0.0153	0.0150	0.0144	0.0136
5	0.0124	0.0122	0.0118	0.0114
6	0.0103	0.0101	0.0100	0.0097
7	0.0087	0.0086	0.0085	0.0083
8	0.0075	0.0074	0.0074	0.0072
9	0.0065	0.0064	0.0064	0.0063
10	0.0057	0.0056	0.0056	0.0055
11	0.0050	0.0049	0.0049	0.0049
12	0.0044	0.0043	0.0043	0.0043

TABLE 2(b)

Perturbation Distribution Due to Distributed Unit Perturbation Load on Stringer 0 In Bay 0

B = 5

Stringer Loads: $\frac{P_{ij}}{L}$

j \ i	1	2	3	4
0	0.3840	0.2328	0.1541	0.1105
1	0.0349	0.0684	0.0738	0.0695
2	0.0091	0.0242	0.0335	0.0380
3	0.0040	0.0115	0.0176	0.0219
4	0.0023	0.0067	0.0106	0.0138
5	0.0015	0.0044	0.0071	0.0094
6	0.0010	0.0031	0.0051	0.0069
7	0.0008	0.0023	0.0038	0.0052
8	0.0006	0.0018	0.0030	0.0041
9	0.0005	0.0015	0.0024	0.0034
10	0.0004	0.0012	0.0020	0.0028
11	0.0003	0.0010	0.0017	0.0024
12	0.0003	0.0009	0.0015	0.0021

Panel Shears: q_{ij}

j \ i	0	1	2	3
0	0.1160	0.0756	0.0394	0.0218
1	0.0461	0.0421	0.0340	0.0261
2	0.0280	0.0270	0.0247	0.0216
3	0.0199	0.0195	0.0187	0.0172
4	0.0153	0.0152	0.0148	0.0140
5	0.0123	0.0123	0.0120	0.0116
6	0.0102	0.0102	0.0101	0.0098
7	0.0087	0.0087	0.0086	0.0084
8	0.0074	0.0075	0.0074	0.0073
9	0.0064	0.0065	0.0064	0.0063
10	0.0056	0.0057	0.0056	0.0056
11	0.0049	0.0050	0.0049	0.0049
12	0.0043	0.0044	0.0043	0.0043

TABLE 2(c)

Perturbation Distribution Due to Unit Shear Perturbation Load About Shear Panel (0,C)

B = 5

Stringer Loads: $\frac{P_{ij}}{L}$

j \ i	1	2	3	4
1	-0.3491	-0.1644	-0.0803	-0.0410
2	-0.0258	-0.0443	-0.0403	-0.0315
3	-0.0050	-0.0126	-0.0159	-0.0160
4	-0.0017	-0.0048	-0.0070	-0.0081
5	-0.0008	-0.0023	-0.0035	-0.0044
6	-0.0004	-0.0013	-0.0020	-0.0026
7	-0.0003	-0.0008	-0.0012	-0.0016
8	-0.0002	-0.0005	-0.0008	-0.0011
9	-0.0001	-0.0004	-0.0006	-0.0007
10	-0.0001	-0.0002	-0.0004	-0.0006
11	-0.0001	-0.0002	-0.0003	-0.0004
12	-0.0000	-0.0001	-0.0002	-0.0003

Panel Shears: q_{ij}

j \ i	0	1	2	3
0	0.2320	0.1512	0.0787	0.0436
1	-0.0698	-0.0335	-0.0054	0.0043
2	-0.0182	-0.0151	-0.0093	-0.0045
3	-0.0081	-0.0075	-0.0060	-0.0044
4	-0.0046	-0.0044	-0.0039	-0.0032
5	-0.0030	-0.0029	-0.0027	-0.0024
6	-0.0021	-0.0020	-0.0020	-0.0018
7	-0.0016	-0.0015	-0.0015	-0.0014
8	-0.0012	-0.0012	-0.0012	-0.0011
9	-0.0010	-0.0010	-0.0010	-0.0009
10	-0.0008	-0.0008	-0.0008	-0.0008
11	-0.0007	-0.0007	-0.0007	-0.0007
12	-0.0006	-0.0006	-0.0006	-0.0006

Fig. 2; stringer loads are assumed positive in tension, and the sign convention for shear flows is the same as that for shear perturbation loadings. The perturbation solutions for arbitrary locations of the perturbation loadings are readily obtained from the tables by means of changes of indices.

Analytical Procedure

Unreinforced Cutout.—Suppose the basic stress distribution is known. In a tension panel under uniform load, this basic distribution simply states that the stringer load everywhere is equal to the applied stringer load and that the shear flow everywhere is zero. The stress distribution in the panel with a cutout is determined in the following manner: Concentrated perturbation loads are imposed on the *basic* structure at stations where stringers will be interrupted by the cutout, and distributed perturbation loads are imposed along stringers that will bound the cutout. The magnitudes of these perturbation loads are adjusted so that simultaneous removal of the cutout material and the perturbation loads would leave the structure outside of the cutout unaffected. Then, with this condition satisfied, the stresses in the structure with the cutout subjected to the basic loading only are precisely those in the *basic* structure due to the basic loading, together with the perturbation loadings.

Consider the case where the cutout is only one bay long, as in Fig. 1. At each pair of stations in the basic structure where a stringer would be interrupted by the cutout, there is placed a pair of concentrated perturbations equal in magnitude and acting in opposite directions. Fig. 3 shows these perturbations applied to a basic structure for the cutout of Fig. 1. It is to be noted that, under these perturbation loads, as well as under the basic loading, no shear flow is introduced into the shear panels of bay 0.

At each point where a concentrated perturbation load is applied there is a discontinuity of stringer load equal in magnitude to the perturbation load. Thus, in the stringers that will be interrupted by the cutout, a distinction must be made between the stringer load just inside of the proposed cutout and that just outside of the proposed cutout. Consider the stringer load

TABLE 3(a)

Perturbation Distribution Due to Concentrated Unit Perturbation Load at Station (0,0)

B = 7

Stringer Loads: P_{ij}

i \ j	0	1	2	3	4
0	0.5000	0.3158	0.2121	0.1514	0.1142
1	0	0.0534	0.0713	0.0738	0.0702
2	0	0.0151	0.0266	0.0338	0.0377
3	0	0.0068	0.0129	0.0178	0.0216
4	0	0.0039	0.0075	0.0108	0.0135
5	0	0.0025	0.0049	0.0072	0.0092
6	0	0.0018	0.0035	0.0051	0.0067
7	0	0.0013	0.0026	0.0039	0.0051
8	0	0.0010	0.0020	0.0030	0.0040
9	0	0.0008	0.0017	0.0025	0.0033
10	0	0.0007	0.0014	0.0021	0.0027
11	0	0.0006	0.0012	0.0018	0.0023
12	0	0.0005	0.0010	0.0015	0.0020

Panel Shears: $q_{ij}L$

i \ j	0	1	2	3
0	0.0921	0.0519	0.0304	0.0186
1	0.0387	0.0339	0.0278	0.0222
2	0.0236	0.0228	0.0206	0.0164
3	0.0168	0.0164	0.0156	0.0146
4	0.0129	0.0128	0.0124	0.0119
5	0.0104	0.0103	0.0101	0.0098
6	0.0087	0.0086	0.0085	0.0083
7	0.0074	0.0073	0.0072	0.0071
8	0.0063	0.0063	0.0062	0.0062
9	0.0055	0.0055	0.0054	0.0054
10	0.0048	0.0048	0.0047	0.0047
11	0.0042	0.0042	0.0042	0.0041
12	0.0037	0.0037	0.0036	0.0036

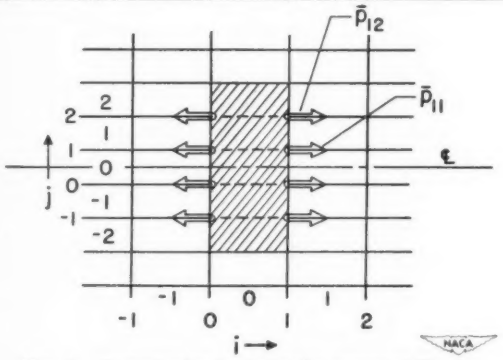

FIG. 3. Perturbation loads for the cutout of Fig. 1.

TABLE 3(b)

Perturbation Distribution Due to Distributed Unit Perturbation Load on Stringer 0 in Bay 0

B = 7

Stringer Loads: $\frac{P_{ij}}{L}$

i \ j	1	2	3	4
0	0.3991	0.2593	0.1792	0.1314
1	0.0308	0.0442	0.0433	0.0422
2	0.0078	0.0212	0.0306	0.0360
3	0.0034	0.0099	0.0155	0.0198
4	0.0019	0.0057	0.0092	0.0122
5	0.0013	0.0037	0.0060	0.0082
6	0.0009	0.0026	0.0043	0.0059
7	0.0006	0.0020	0.0033	0.0045
8	0.0005	0.0015	0.0025	0.0035
9	0.0004	0.0013	0.0021	0.0029
10	0.0004	0.0010	0.0017	0.0024
11	0.0003	0.0009	0.0015	0.0021
12	0.0002	0.0008	0.0013	0.0018

Panel Shears: q_{ij}

i \ j	0	1	2	3
0	0.1009	0.0699	0.0400	0.0239
1	0.0392	0.0366	0.0309	0.0250
2	0.0237	0.0231	0.0216	0.0195
3	0.0169	0.0166	0.0160	0.0152
4	0.0130	0.0128	0.0126	0.0122
5	0.0105	0.0104	0.0102	0.0100
6	0.0087	0.0086	0.0086	0.0084
7	0.0074	0.0073	0.0073	0.0072
8	0.0064	0.0063	0.0063	0.0062
9	0.0056	0.0054	0.0054	0.0054
10	0.0048	0.0048	0.0048	0.0047
11	0.0042	0.0042	0.0042	0.0042
12	0.0038	0.0036	0.0037	0.0036

TABLE 3(c)

Perturbation Distribution Due to Unit Shear Perturbation Load about Shear Panel (0,0)

B = 7

Stringer Loads: $\frac{P_{ij}}{L}$

i \ j	1	2	3	4
1	-0.3683	-0.1951	-0.1059	-0.0592
2	-0.0230	-0.0430	-0.0427	-0.0362
3	-0.0084	-0.0113	-0.0151	-0.0162
4	-0.0045	-0.0062	-0.0083	-0.0076
5	-0.0007	-0.0020	-0.0031	-0.0040
6	-0.0004	-0.0011	-0.0018	-0.0023
7	-0.0002	-0.0006	-0.0010	-0.0014
8	-0.0001	-0.0004	-0.0007	-0.0009
9	-0.0001	-0.0003	-0.0005	-0.0006
10	-0.0001	-0.0002	-0.0004	-0.0005
11	-0.0001	-0.0002	-0.0002	-0.0003
12	0.0000	-0.0001	-0.0002	-0.0003

Panel Shears: q_{ij}

i \ j	0	1	2	3
0	0.2017	0.1398	0.0801	0.0478
1	-0.0616	-0.0334	-0.0091	0.0010
2	-0.0155	-0.0134	-0.0094	-0.0055
3	-0.0068	-0.0065	-0.0056	-0.0043
4	-0.0039	-0.0038	-0.0034	-0.0030
5	-0.0025	-0.0025	-0.0023	-0.0021
6	-0.0018	-0.0017	-0.0017	-0.0016
7	-0.0013	-0.0013	-0.0013	-0.0012
8	-0.0010	-0.0010	-0.0010	-0.0010
9	-0.0008	-0.0008	-0.0008	-0.0008
10	-0.0007	-0.0007	-0.0007	-0.0007
11	-0.0006	-0.0006	-0.0006	-0.0006
12	-0.0005	-0.0005	-0.0005	-0.0005

just outside of the proposed cutout in a stringer that will be interrupted by the cutout. When the magnitudes of the concentrated perturbation loads are adjusted to give, together with the basic loading, zero stringer loads at these points, the portion of the structure lying within the cutout can be removed from the basic structure, and, simultaneously, the perturbation loads themselves can be removed from the basic structure without affecting the rest of the structure. Thus, in this problem of a one-bay-long cutout, distributed perturbation loads along the coaming stringer are not needed.

The conditions that the concentrated perturbation loads must satisfy are expressed mathematically in the following manner: Let $\bar{p}_{kl}$ represent the magnitude of the perturbation load at k, l. Let $P_{ij}(k, l)$ represent the stringer load at i, j toward the outside of the cutout due to a unit concentrated perturbation load at

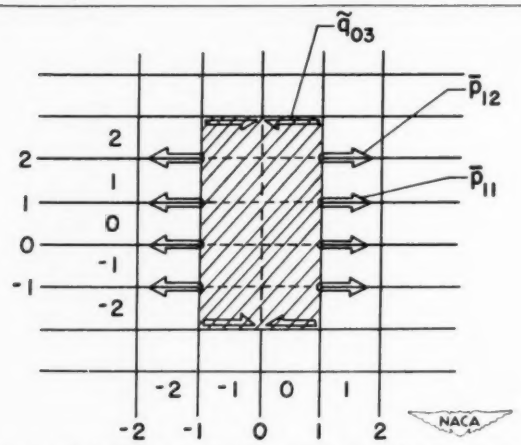

FIG. 4. Perturbation loads for a cutout extending two bays in length.

TABLE 4(a)

Perturbation Distribution Due to Concentrated Unit Perturbation Load at Station (0,0)

B = 9

Stringer Loads: P_{ij}

j \ i	0	1	2	3	4
0	0.5000	0.3328	0.2322	0.1699	0.1300
1	0	0.0493	0.0687	0.0738	0.0722
2	0	0.0135	0.0243	0.0317	0.0362
3	0	0.0060	0.0115	0.0162	0.0200
4	0	0.0034	0.0067	0.0097	0.0123
5	0	0.0022	0.0044	0.0064	0.0083
6	0	0.0016	0.0031	0.0046	0.0060
7	0	0.0012	0.0023	0.0034	0.0045
8	0	0.0009	0.0018	0.0027	0.0036
9	0	0.0007	0.0015	0.0022	0.0029
10	0	0.0006	0.0012	0.0018	0.0024
11	0	0.0005	0.0010	0.0016	0.0021
12	0	0.0005	0.0009	0.0014	0.0018

Panel Shears: $q_{ij}L$

j \ i	0	1	2	3
0	0.0836	0.0503	0.0312	0.0199
1	0.0343	0.0309	0.0261	0.0215
2	0.0209	0.0201	0.0187	0.0170
3	0.0148	0.0146	0.0140	0.0133
4	0.0114	0.0113	0.0110	0.0107
5	0.0092	0.0091	0.0090	0.0088
6	0.0077	0.0076	0.0075	0.0074
7	0.0065	0.0065	0.0064	0.0063
8	0.0056	0.0056	0.0055	0.0055
9	0.0048	0.0048	0.0048	0.0048
10	0.0042	0.0042	0.0042	0.0042
11	0.0037	0.0037	0.0036	0.0037
12	0.0033	0.0033	0.0032	0.0032

k, l. Let $\bar{P}$ represent the basic stringer load. The conditions on the $\bar{p}_{kl}$ are expressed as

$$\sum_k \sum_l \bar{p}_{kl} P_{ij}(k, l) + \bar{P} = 0 \quad \ldots\ldots\ldots (1)$$

where the summation is carried over the k, l for all perturbation loads and where the equations are written for each station i, j at which the cutout will interrupt a stringer.

TABLE 4(b)

Perturbation Distribution Due to Distributed Unit Perturbation Load on Stringer 0 in Bay 0

B = 9

Stringer Loads: $\frac{P_{ij}}{L}$

j \ i	1	2	3	4
0	0.1094	0.2785	0.1987	0.1485
1	0.0280	0.0606	0.0720	0.0733
2	0.0069	0.0192	0.0283	0.0342
3	0.0030	0.0089	0.0140	0.0182
4	0.0017	0.0050	0.0082	0.0110
5	0.0011	0.0033	0.0054	0.0073
6	0.0008	0.0023	0.0038	0.0053
7	0.0006	0.0017	0.0029	0.0040
8	0.0005	0.0014	0.0023	0.0031
9	0.0004	0.0011	0.0018	0.0025
10	0.0003	0.0009	0.0015	0.0021
11	0.0003	0.0008	0.0013	0.0018
12	0.0002	0.0007	0.0011	0.0016

Panel Shears: q_{ij}

j \ i	0	1	2	3
0	0.0906	0.0654	0.0399	0.0251
1	0.0347	0.0328	0.0285	0.0238
2	0.0209	0.0205	0.0194	0.0179
3	0.0148	0.0147	0.0143	0.0137
4	0.0114	0.0113	0.0112	0.0109
5	0.0092	0.0092	0.0091	0.0089
6	0.0077	0.0076	0.0076	0.0075
7	0.0065	0.0065	0.0065	0.0064
8	0.0056	0.0056	0.0055	0.0055
9	0.0049	0.0048	0.0048	0.0048
10	0.0042	0.0042	0.0042	0.0042
11	0.0037	0.0037	0.0037	0.0037
12	0.0032	0.0033	0.0032	0.0032

In case the cutout does extend more than one bay in length, distributed perturbation loads must be imposed on the basic structure on the stringers bounding the edges of the cutout (the coaming stringers) within the bays where the cutout exists. Fig. 4 illustrates the application of perturbation loads when the cutout extends two bays. The magnitudes of the distributed perturbation loads must be adjusted so that, in each of the shear panels adjacent to these perturbation loads on the inside of the proposed cutout, the sum of the shear flows due to all the perturbation loadings just cancels the distributed perturbation loading at that shear panel. The conditions on the stringers at stations where they are interrupted by the cutout remain the same as before. When these conditions on the distributed and concentrated perturbation loads hold, the boundary conditions at the cutout are satisfied, and the portion of the basic structure within the proposed cutout can be removed along with the perturbation loads without affecting the rest of the structure.

The mathematical formulation of the problem now becomes as follows: Let $P_{ij}\{k, l\}$ mean the stringer load at i, j due to a distributed unit perturbation load on stringer l between rib k and rib $k + 1$. Let $q_{ij}(k, l)$

TABLE 4(c)

Perturbation Distribution Due to Unit Shear Perturbation Load about Shear Panel (0,0)

B = 9

Stringer Loads: $\frac{P_{ij}}{l}$

i / j	1	2	3	4
1	-0.3814	-0.2179	-0.1267	-0.0752
2	-0.0211	-0.0414	-0.0437	-0.0357
3	-0.0039	-0.0103	-0.0143	-0.0160
4	-0.0013	-0.0038	-0.0058	-0.0072
5	-0.0006	-0.0018	-0.0028	-0.0036
6	-0.0003	-0.0010	-0.0015	-0.0021
7	-0.0002	-0.0006	-0.0010	-0.0013
8	-0.0001	-0.0004	-0.0006	-0.0008
9	-0.0001	-0.0002	-0.0004	-0.0006
10	-0.0001	0.0002	-0.0003	-0.0004
11	-0.0000	0.0001	-0.0002	-0.0003
12	-0.0000	0.0001	-0.0002	-0.0002

Panel Shears: q_{ij}

i / j	0	1	2	3
0	0.1813	0.1309	0.0798	0.0502
1	-0.0559	-0.0326	-0.0114	-0.0013
2	-0.0138	-0.0123	-0.0091	-0.0059
3	-0.0060	-0.0058	-0.0051	-0.0042
4	-0.0034	-0.0034	-0.0031	-0.0028
5	-0.0022	-0.0022	-0.0021	-0.0020
6	-0.0016	-0.0015	-0.0015	-0.0014
7	-0.0012	-0.0011	-0.0011	-0.0011
8	-0.0009	-0.0009	-0.0009	-0.0009
9	-0.0008	-0.0007	-0.0007	-0.0007
10	-0.0006	-0.0006	-0.0006	-0.0006
11	-0.0005	-0.0005	-0.0005	-0.0005
12	-0.0004	-0.0005	-0.0004	-0.0005

represent the shear flow in panel i, j due to a concentrated unit perturbation load at station k, l, and let $q_{ij}\{k, l\}$ represent the shear flow in shear panel i, j due to a distributed unit perturbation load on stringer l between rib k and rib $k + 1$. If $\bar{q}_{kl}$ represents the magnitude of the distributed perturbation load on stringer l between rib k and rib $k + 1$, the equations that must hold are

$$\sum_k \sum_l \bar{p}_{kl} P_{ij}(k, l) + \sum_k \sum_l \bar{q}_{kl} P_{ij}\{k, l\} + \bar{P} = 0 \quad (2)$$

$$\sum_k \sum_l \bar{p}_{kl} q_{ij}(k, l) + \sum_k \sum_l \bar{q}_{kl} q_{ij}\{k, l\} = \bar{q}_{ij} \quad (3)$$

where the summations over k and l are extended over all the concentrated perturbation loads and all the distributed perturbation loads. Eqs. (2) are written for every station i, j where the cutout will interrupt a stringer. Eqs. (3) are written for each shear panel i, j adjacent to a coaming stringer and inside of the proposed cutout.

Solution of the system in Eq. (1) for a cutout one bay long or solution of Eqs. (2) and (3) for cutouts extending more than one bay in length yields the required magnitudes of the concentrated and distributed perturbation loads $\bar{p}_{kl}$ and $\bar{q}_{kl}$. The quantities $P_{ij}(k, l)$ and $q_{ij}(k, l)$ in Eqs. (1) to (3) are obtained from parts

TABLE 5(a)

Perturbation Distribution Due to Concentrated Unit Perturbation Load at Station (0,0)

B = 11

Stringer Loads: P_{ij}

i / j	0	1	2	3	4
0	0.5000	0.3456	0.2481	0.1852	0.1435
1	0	0.0460	0.0663	0.0731	0.0732
2	0	0.0123	0.0225	0.0299	0.0348
3	0	0.0055	0.0106	0.0150	0.0186
4	0	0.0031	0.0061	0.0088	0.0113
5	0	0.0020	0.0040	0.0058	0.0076
6	0	0.0014	0.0028	0.0041	0.0054
7	0	0.0010	0.0021	0.0031	0.0041
8	0	0.0008	0.0016	0.0024	0.0032
9	0	0.0007	0.0013	0.0020	0.0026
10	0	0.0006	0.0011	0.0017	0.0022
11	0	0.0005	0.0009	0.0014	0.0019
12	0	0.0004	0.0008	0.0012	0.0016

Panel Shears: $q_{ij}L$

i / j	0	1	2	3
0	0.0772	0.0487	0.0315	0.0209
1	0.0312	0.0285	0.0247	0.0208
2	0.0189	0.0183	0.0172	0.0159
3	0.0134	0.0132	0.0128	0.0123
4	0.0103	0.0102	0.0100	0.0098
5	0.0083	0.0083	0.0082	0.0080
6	0.0069	0.0069	0.0068	0.0067
7	0.0059	0.0058	0.0058	0.0058
8	0.0050	0.0050	0.0050	0.0050
9	0.0044	0.0044	0.0044	0.0043
10	0.0038	0.0038	0.0038	0.0038
11	0.0034	0.0033	0.0033	0.0033
12	0.0029	0.0029	0.0029	0.0029

(a) of Tables 1–5; $P_{ij}\{k, l\}$ and $q_{ij}\{k, l\}$ are found in parts (b) of these tables. The stresses about the cutout are then obtained by superposing the perturbation stress distribution in the basic structure on the basic stress distribution.

The unit perturbation solutions presented in the tables apply to panels that extend to infinity in both directions; they can be applied directly to a finite panel without serious error if the cutout does not come too close to the edge of the panel. A refinement in the analysis to account for edge effect will be discussed later.

To illustrate the method of analysis, the solution for a cutout in a tension panel will be presented. The case to be analyzed is that of a long panel with 16 stringers having a cutout one bay long which interrupts four stringers and removes five shear panels. (See Fig. 1.) Other pertinent properties of the panel are taken as follows:

b = 3.125 in.
L = 3.00 in.
t = 0.0331 in.
A = 0.2516 sq.in.
A/bt = 0.2516/0.1035 = 2.43

UNIVERSITY OF MICHIGAN LIBRARIES

TABLE 5(b)

Perturbation Distribution Due to Distributed Unit Perturbation Load on Stringer 0 in Bay 0

B = 11

Stringer Loads: $\frac{P_{ij}}{L}$

j \ i	1	2	3	4
0	0.4169	0.2933	0.2145	0.1630
1	0.0258	0.0576	0.0705	0.0735
2	0.0063	0.0176	0.0264	0.0325
3	0.0027	0.0080	0.0128	0.0169
4	0.0016	0.0046	0.0075	0.0101
5	0.0010	0.0030	0.0049	0.0067
6	0.0007	0.0021	0.0035	0.0048
7	0.0005	0.0016	0.0026	0.0036
8	0.0004	0.0012	0.0020	0.0028
9	0.0003	0.0010	0.0016	0.0023
10	0.0003	0.0008	0.0014	0.0019
11	0.0002	0.0007	0.0012	0.0016
12	0.0002	0.0006	0.0010	0.0014

Panel Shears: q_{ij}

j \ i	0	1	2	3
0	0.0831	0.0618	0.0394	0.0258
1	0.0315	0.0300	0.0266	0.0227
2	0.0189	0.0186	0.0178	0.0166
3	0.0134	0.0133	0.0130	0.0126
4	0.0103	0.0103	0.0101	0.0100
5	0.0084	0.0083	0.0082	0.0081
6	0.0070	0.0069	0.0069	0.0068
7	0.0059	0.0058	0.0058	0.0058
8	0.0051	0.0050	0.0050	0.0050
9	0.0045	0.0044	0.0043	0.0044
10	0.0039	0.0038	0.0038	0.0039
11	0.0035	0.0033	0.0033	0.0034
12	0.0031	0.0029	0.0029	0.0030

TABLE 5(c)

Perturbation Distribution Due to Unit Shear Perturbation Load about Shear Panel (0,0)

B = 11

Stringer Loads: $\frac{P_{ij}}{L}$

j \ i	1	2	3	4
1	-0.3910	-0.2356	-0.0440	-0.0895
2	-0.0196	-0.0400	-0.0441	-0.0410
3	-0.0035	-0.0096	-0.0136	-0.0156
4	-0.0012	-0.0035	-0.0054	-0.0068
5	-0.0006	-0.0016	-0.0026	-0.0034
6	-0.0003	-0.0009	-0.0014	-0.0019
7	-0.0002	-0.0005	-0.0008	-0.0012
8	-0.0001	-0.0004	-0.0006	-0.0008
9	-0.0001	-0.0002	-0.0004	-0.0005
10	-0.0001	-0.0002	-0.0003	-0.0004
11	0.0000	-0.0001	-0.0002	-0.0003
12	0.0000	-0.0001	-0.0002	-0.0002

Panel Shears: q_{ij}

j \ i	0	1	2	3
0	0.1663	0.1236	0.0788	0.0515
1	-0.0517	-0.0318	-0.0128	-0.0030
2	-0.0125	-0.0114	-0.0088	-0.0061
3	-0.0055	-0.0053	-0.0048	-0.0041
4	-0.0031	-0.0030	-0.0029	-0.0026
5	-0.0020	-0.0020	-0.0019	-0.0018
6	-0.0014	-0.0014	-0.0014	-0.0013
7	-0.0011	-0.0010	-0.0010	-0.0010
8	-0.0008	-0.0008	-0.0008	-0.0008
9	-0.0007	-0.0007	-0.0007	-0.0007
10	-0.0005	-0.0006	-0.0006	-0.0005
11	-0.0005	-0.0005	-0.0005	-0.0005
12	-0.0004	-0.0004	-0.0004	-0.0004

$$b^2/L^2 = (3.125/3.00)^2 = 1.085$$
$$B = (E/G)\,(A/bt)\,(b^2/L^2) = 6.99$$

Fig. 3 illustrates the perturbation loads to be applied to the basic structure; the perturbations are doubly symmetric about the cutout.

Application of Eq. (1) in order to liquidate the load in stringer 2 just outside of the cutout at (1, 2) (see Fig. 3) gives

$$\bar{p}_{1,}P_{12}(1, 2) + \bar{p}_{11}P_{12}(1, 1) + \bar{p}_{10}P_{12}(1, 0) + \bar{p}_{1,\,-1}P_{12}(1, -1) + \bar{p}_{02}P_{12}(0, 2) + \bar{p}_{01}P_{12}(0, 1) + \bar{p}_{00}P_{12}(0, 0) + \bar{p}_{0,\,-1}P_{12}(0, -1) + \bar{P} = 0 \quad (4)$$

From the conditions of symmetry,

$$\bar{p}_{12} = -\bar{p}_{02} = -\bar{p}_{0,\,-1} = \bar{p}_{1,\,-1}$$
$$\bar{p}_{11} = -\bar{p}_{01} = -\bar{p}_{00} = \bar{p}_{10}$$

With the assumption $B = 7$ it is found from Table 3(a) that

$$P_{12}(1, 2) = 0.5000$$
$$P_{12}(1, 1) = P_{12}(1, 0) = P_{12}(1, -1) = 0$$
$$P_{12}(0, 2) = 0.3158$$
$$P_{12}(0, 1) = 0.0534$$
$$P_{12}(0, 0) = 0.0151$$
$$P_{12}(0, -1) = 0.0068$$

Substituting these values into Eq. (4) yields

$$\bar{P} - 0.1774\bar{p}_{12} + 0.0685\bar{p}_{11} = 0 \quad (5)$$

Similarly, liquidation of the load in stringer 1 at (1, 1) requires that

$$\bar{P} + 0.0685\bar{p}_{12} - 0.1308\bar{p}_{11} = 0 \quad (6)$$

TABLE A

Stringer Loads		Shear Flows	
Intersection of Rib and Stringer	Load	Shear Panel	Shear Flow
(1, 3)	$1.906\bar{P}$	(1, 0)	$0\bar{P}/L$
(1, 4)	$1.331\bar{P}$	(1, 1)	$-0.176\bar{P}/L$
(1, 5)	$1.176\bar{P}$	(1, 2)	$-0.515\bar{P}/L$
(1, 6)	$1.113\bar{P}$	(1, 3)	$-0.074\bar{P}/L$
		(1, 4)	$-0.021\bar{P}/L$

Because of symmetry, Eqs. (5) and (6) are the only independent equations. That is, if equations are written stating the liquidation of the load at any of the other points where a stringer is cut, they will turn out to be identical to either Eq. (5) or Eq. (6).

The solution to the system of Eqs. (5) and (6) yields

$$\bar{p}_{12} = 10.75\bar{P}, \qquad \bar{p}_{11} = 13.28\bar{P}$$

Stringer loads and shear flows in the neighborhood of the cutout are obtained with this solution in conjunction with Table 3(a). Some results are shown in Table A.

Reinforced Cutout.—The analysis is easily extended to include the problem of shear reinforcement about the cutout. Assume that some of the shear panels in the neighborhood of a cutout are reinforced by the addition of a certain thickness of sheet (i.e., a doubler plate). Then, the procedure consists of adding shear perturbations to each of the panels of the basic structure which is reinforced in the actual structure. On the doubler plate, or the added portion of skin which is the shear reinforcement of the panel, place the same perturbation with the opposite sign. Then, for each reinforced panel, write an equation that states the requirement that the shear stress in the shear panel of the basic structure shall equal the shear stress in the excess portion of skin used to reinforce that panel. When this condition is satisfied, the loaded excess portions of sheet (the doubler plates) can be considered inserted in the basic structure without disturbing continuity. The shear flows on the upper and lower edges of the excess portions of sheet cancel the shear perturbation loads on the basic structure, and the shear flows on the vertical edges of the excess portions of sheet go directly into the rigid ribs.

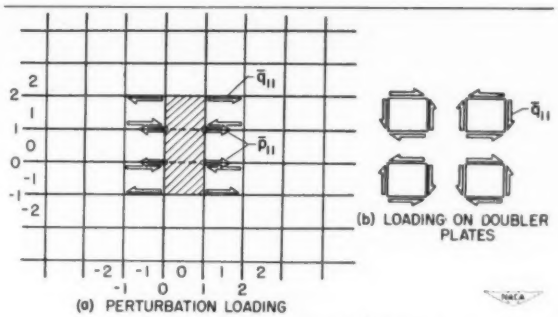

FIG. 5. Panel with shear reinforcement.

As an example, consider for simplicity a tension panel with a cutout interrupting only two stringers and removing three shear panels as indicated in Fig. 5(a). The solution for this panel without reinforcement shows that the most highly loaded shear panels are (1, 1), (−1, 1), (1, −1), and (−1, −1). Suppose now that these shear panels are reinforced by the addition of plates of thickness t' to the skin of thickness t so that the total thickness in these panels is $t + t'$. The perturbation loadings to be placed on the basic structure are those shown in Fig. 5(a). In Fig. 5(b) are shown the four reinforcing plates or the excess material used for reinforcement. These plates are of thickness t'. They are loaded with shear flows whose magnitudes are the same as the shear perturbation in the corresponding panels in the basic structure but with opposite sign.

The conditions that must be satisfied are:

(a) The stringer load must be zero at (1, 0), (1, 1), (0, 0), and (0, 1) toward the outside of the cutout.

(b) The shear flow in panels (0, −1) and (0, 1) must cancel any distributed perturbation load applied to the coaming stringers bounding these panels. (In this problem there are no distributed perturbation loads applied here, and this condition is automatically satisfied.)

(c) The shear stress in each of the panels (1, 1), (1, −1), (−1, 1), and (−1, −1) in the basic structure must equal the shear stress in the corresponding reinforcing plates shown in Fig. 5(b).

Assuming $B = 7$ and referring to Tables 3(a) and 3(c) yields, for condition (a),

$$\bar{P} - 0.5000\bar{p}_{11} + 0.3158\bar{p}_{11} + 0.0534\bar{p}_{11} - 0.3683\bar{q}_{11}L - 0.1951\bar{q}_{11}L - 0.0230\bar{q}_{11}L - 0.0430\bar{q}_{11}L = 0$$

Condition (b) is automatically satisfied by symmetry. Condition (c) is expressed by the equation

$$[-0.0921\,(\bar{p}_{11}/L) + 0.0519(\bar{p}_{11}/L) - 0.0387\,(\bar{p}_{11}/L) + 0.0339\,(\bar{p}_{11}/L) + 0.2017\bar{q}_{11} - 0.0801\bar{q}_{11} + 0.0155\bar{q}_{11} - 0.0094\bar{q}_{11}]\,(1/t) = -\bar{q}_{11}(1/t')$$

These equations become

$$0.1308\bar{p}_{11} + 0.6294\bar{q}_{11}L = \bar{P}$$

$$-0.0451\bar{p}_{11} + [0.1279 + (t/t')]\bar{q}_{11}L = 0$$

For any given ratio t/t' this set of equations can be solved for the unknown perturbations $\bar{p}_{ij}$ and $\bar{q}_{ij}$. The stresses due to these perturbations are superposed on the basic stress distribution to give the stress distribution about the cutout.

The analysis is also easily extended to handle the problem of reinforced coaming stringers. It is assumed that the stringer load is distributed immediately into the added portion of the coaming stringer such that the stress is always given by the force divided by the cross-sectional area. Consider again the tension panel with a cutout interrupting two stringers and removing three shear panels. Assume the coaming stringers have reinforcements of constant area extending one bay on either side of the cutout. Let the cross-sectional area of the added portion be A' so that the total cross-sectional area of the reinforced portions of the coaming stringers is $A + A'$.

In Fig. 6(a) are shown the perturbation loads that are to be placed on the structure. The symbol $\bar{q}_{ij}$ represents the magnitude of the distributed perturbation load applied to that portion of stringer j lying between rib i and rib $i + 1$. In Fig. 6(b) are shown the loads on the added portions of the coaming stringers which have a cross-sectional area A'. The following conditions must hold:

(a) The stringer load at (1, 1), (1, 0), (0, 0), and (0, 1) toward the outside of the cutout must vanish.

(b) The shear flow in panels (0, −1) and (0, 1) must cancel any distributed perturbation loading applied to the coaming stringers bounding these panels. (There are no perturbation loadings applied here, and this condition is automatically satisfied.)

(c) The stress in the basic coaming stringer must equal the stress in the excess reinforcing portion at the points (1, 2), (0, 2), (1, −1), and (0, −1) and at the following points on the side toward the reinforcement: (2, 2), (−1, 2), (−1, −1), and (2, −1).

When condition (c) is satisfied, the excess portions of the coaming stringers (of area A') can be added to the basic structure without violating continuity and can thus replace the perturbation loads on their corresponding portions in the basic structure.

To satisfy condition (a), the following equation must hold [assuming $B = 7$, see Tables 3(a) and 3(b)]:

$$\bar{P} - 0.5000\bar{p}_{11} + 0.3158\bar{p}_{11} + 0.0534\bar{p}_{11} - 0.0534\bar{p}_{22} - 0.0151\bar{p}_{22} - 0.0713\bar{p}_{22} - 0.0266\bar{p}_{22} - 0.0308\bar{q}_{11}L - 0.0642\bar{q}_{11}L - 0.0078\bar{q}_{11}L - 0.0212\bar{q}_{11}L = 0$$

Condition (b) is automatically satisfied by symmetry. Condition (c) is satisfied by the following equations:

At (2, 2) on the side toward the reinforcement

$$(\bar{P} - 0.5000\bar{p}_{22} - 0.1514\bar{p}_{22} - 0.0178\bar{p}_{22} - 0.0534\bar{p}_{11} - 0.0151\bar{p}_{11} + 0.0713\bar{p}_{11} + 0.0266\bar{p}_{11} + 0.3991\bar{q}_{11}L - 0.1792\bar{q}_{11}L + 0.0034\bar{q}_{11}L - 0.0155\bar{q}_{11}L)\,(1/A) = \bar{p}_{22}(1/A')$$

and at (1, 2)

$$(\bar{P} - 0.3158\bar{p}_{22} - 0.2121\bar{p}_{22} - 0.0129\bar{p}_{22} - 0.0068\bar{p}_{22} + 0.0534\bar{p}_{11} + 0.0151\bar{p}_{11} - 0.3991\bar{q}_{11}L - 0.2593\bar{q}_{11}L - 0.0034\bar{q}_{11}L - 0.0099\bar{q}_{11}L)1/A = (\bar{p}_{22} + \bar{q}_{11}L)\,(1/A')$$

These three equations reduce to

$$0.1664\bar{p}_{22} + 0.1308\bar{p}_{11} + 0.1240\bar{q}_{11}L = \bar{P}$$

$$[0.6692 + (A/A')]\bar{p}_{22} - 0.0294\bar{p}_{11} - 0.2079\bar{q}_{11}L = \bar{P}$$

$$[0.5476 + (A/A')]\bar{p}_{22} - 0.0685\bar{p}_{11} + [0.6718 + (A/A')]\bar{q}_{11}L = \bar{P}$$

For given values of A/A' these equations can be solved for the unknown perturbations $\bar{p}_{22}$, $\bar{p}_{11}$, and $\bar{q}_{11}$. The stresses due to these perturbations are then superposed on the basic stress distribution to give the stress distribution about the cutout.

Some calculated results for the reinforced cutouts just considered are compared in Table B with results for the same cutout without reinforcement. The reinforced shear panels were taken to have sheet twice as thick as the uniform sheet; the reinforced coaming stringers were assumed to have twice the cross-sectional area of the uniform stringers.

On comparing the results for the reinforced structures with those for the unreinforced structure, the following is noted: In the case of shear reinforcement, although the shear flow in shear panel (1, 1) is greater in the reinforced structure the shear stress in shear panel (1, 1) is less, and the shear reinforcement tends to increase the stringer load at station (1, 2). In the case of coaming stringer reinforcement, the stringer load at station (1, 2) is greater in the reinforced structure, but the stringer stress at (1, 2) is less, and the coaming stringer reinforcement tends to increase slightly the shear flow in shear panel (1, 1).

TABLE B

Stringer Loads		Shear Flows	
Intersection of Rib and Stringer	Stringer Load	Shear Panel	Shear Flow
Unreinforced Cutout			
(1, 2)	$1.524\bar{P}$	(1, 0)	$0 \quad \bar{P}/L$
(1, 3)	$1.168\bar{P}$	(1, 1)	$-0.345\bar{P}/L$
(1, 4)	$1.082\bar{P}$	(1, 2)	$-0.046\bar{P}/L$
(1, 5)	$1.049\bar{P}$	(1, 3)	$-0.012\bar{P}/L$
Cutout with Shear Reinforcement ($t' = t$)			
(1, 2)	$1.581\bar{P}$	(1, 0)	$0 \quad \bar{P}/L$
(1, 3)	$1.156\bar{P}$	(1, 1)	$-0.514\bar{P}/L$
(1, 4)	$1.072\bar{P}$	(1, 2)	$-0.051\bar{P}/L$
(1, 5)	$1.042\bar{P}$	(1, 3)	$-0.011\bar{P}/L$
Cutout with Reinforced Coaming Stringers ($A' = A$)			
(1, 2)	$1.842\bar{P}$	(1, 0)	$0 \quad \bar{P}/L$
(1, 3)	$1.024\bar{P}$	(1, 1)	$-0.348\bar{P}/L$
(1, 4)	$1.028\bar{P}$	(1, 2)	$-0.019\bar{P}/L$
(1, 5)	$1.020\bar{P}$	(1, 3)	$0.000\bar{P}/L$

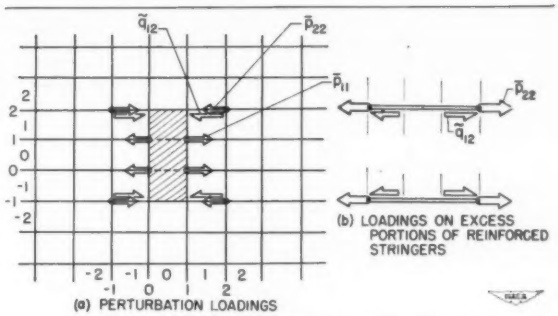

FIG. 6. Panel with reinforced coaming stringers.

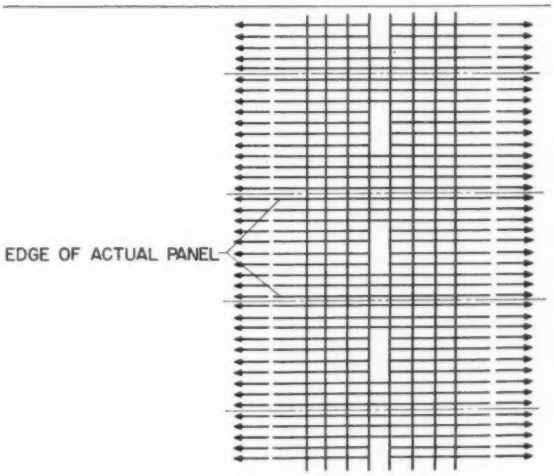

FIG. 7. Typical structural model for solution of wide cutout.

Wide Cutouts.—If the cutout extends close to the edge of the panel, application of the perturbation solutions computed for the infinitely wide panel will not give accurate results. A simple device is proposed to refine the analysis for this problem. The procedure is to reflect the panel about its edges and solve the problem of an infinitely wide panel with a series of cutouts as shown in Fig. 7. This does not increase the number of equations in the systems (1) or (2) and (3) but merely increases the number of points k, l over which the summations must be extended. The shear flows in the shear panels just off the edge of the actual panel all vanish because of symmetry.

The number of image cutouts required is dictated by the desired accuracy. For most problems it will probably be sufficient to consider one image cutout on either side of the actual cutout.

RELATION OF MODEL TO ACTUAL STRUCTURE

In an actual structure the sheet does carry some direct stress, contrary to assumption (d) under the section "Basic Assumptions." To account for this, an effective area of skin is added to the cross-sectional area of each stringer; this effective area usually consists of the cross-sectional area of sheet halfway to the adjacent stringer on each side of the given stringer, so long as the sheet has not buckled. Thus, the stringer area, A, to be used in the calculations is taken as the actual stringer area plus bt.

Ordinarily, within the bay or bays where a cutout exists, the sheet is removed all the way to the coaming stringer. For the portion of the coaming stringer within these bays, the effective area of sheet is that area extending halfway to the adjacent stringer on one side only. Thus there is a discontinuity in the effective area of the coaming stringer. This can be taken into account in the following manner: Assume that the coaming stringer has a reinforcement of *negative* area $bt/2$, and apply the procedure described for analyzing cutouts with reinforced coaming stringers. However, a simpler but more approximate procedure would be to compute the stringer *loads* and shear flows neglecting this discontinuity in coaming stringer effective area and then take it into account when computing stringer *stresses*.

In the structural model the ribs or transverse stiffeners can be placed where the ribs in the actual structure are located. However, if the shear panels are very long relative to the spacing between stringers, the transverse stiffness of the skin itself acts as continuously distributed ribs of finite stiffness and causes the shear flow to vary within the panel. When such is the case, it is possible that a better approximation to the stress distribution will result if fictitious ribs are inserted between the actual ribs. The ribs in the structural model are rigid, thus further investigation is required to determine just how to locate discrete rigid ribs so as best to approximate continuously distributed ribs of finite stiffness. Tentatively, it is suggested that it is convenient to have fictitious ribs spaced so that the cutout length is an integral multiple of rib spacing. Also, it is felt that it is good to have the fictitious rib spacing about equal to the stringer spacing so that the shear panels are roughly square.

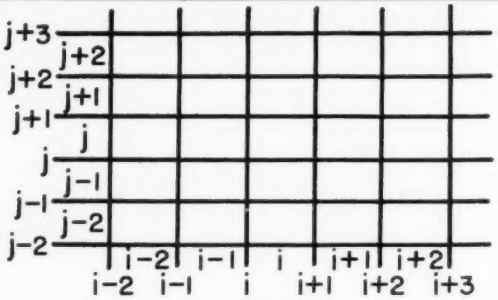

FIG. 8. Index system

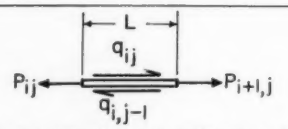

(a) STATICS OF STRINGER j BETWEEN RIB i AND RIB i+1

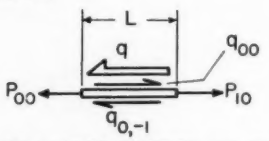

(b) STATICS OF LOADED PORTION OF STRINGER j=0 IN FIGURE 2(c)

NACA

FIG. 9. Statics of stringers.

Appendix

THE UNIT PERTURBATION SOLUTIONS

Derivation of Difference Equation

The principle of minimum complementary energy will be used to derive the homogeneous partial difference equations that govern the stringer loads and shear flows in a sheet-stringer panel with rigid transverse members. Then the loadings of Figs. 2(a) and 2(c) will be applied to the structure in the form of boundary conditions.

Fig. 8 illustrates the notation for the stringers and shear panels. Fig. 9(a) shows the forces and shear flows on the portion of stringer j, which is between rib i and rib $i+1$. The equilibrium of this portion of the stringer gives

$$P_{i+1,\,j} - P_{ij} + (q_{ij} - q_{i,\,j-1})L = 0 \qquad \text{(A1)}$$

The principle of minimum complementary energy states that, of all stress distributions satisfying the boundary conditions on stress, the stress distribution that exists in an elastic structure is the one that minimizes the complementary energy π^*, where π^* = (internal energy) − (work done by surface stresses acting through the prescribed surface displacements). No displacements are prescribed anywhere on the structure in this problem so the second term in the complementary energy vanishes. The transverse stiffeners or ribs are assumed rigid. The shear flow is constant within any shear panel, and the stringer load varies linearly between ribs. For a sheet-stringer panel of this type, the internal energy or stress energy is given by

$$\text{S.E.} = \sum_i \sum_j [(L/6AE)\,(P_{i+1,\,j}{}^2 + P_{ij}P_{i+1,\,j} + P_{ij}{}^2) + (bL/2Gt)q_{ij}{}^2] \qquad \text{(A2)}$$

where the integration over the length of the stringer between ribs has been carried out.

The stringer equilibrium of Eq. (A1) must be maintained. Thus, it is required to minimize S.E. with respect to P_{ij} and q_{ij} with the constraint relationships given by Eq. (A1). This can be accomplished by use of the Lagrangian multiplier technique. Let μ_{ij} represent a Lagrangian multiplier. Then the function that is to be minimized with respect to P_{ij} and q_{ij} is

$$\Phi = \text{S.E.} - \sum_i \sum_j \mu_{ij}\,[P_{i+1,\,j} - P_{ij} + (q_{ij} - q_{i,\,j-1})L] \qquad \text{(A3)}$$

Differentiating with respect to P_{ij} and then with respect to q_{ij} and equating the derivatives to zero gives

$$\partial\Phi/\partial P_{ij} = (L/6AE)\,(2P_{ij} + P_{i+1,\,j} + P_{i-1,\,j} + 2P_{ij}) - (\mu_{i-1,\,j} - \mu_{ij}) = 0$$

$$\partial\Phi/\partial q_{ij} = (bL/2Gt)\cdot 2q_{ij} - [\mu_{ij}L - \mu_{i,\,j+1}\,L] = 0$$

These equations, along with Eq. (A1), become

$$P_{i+1,\,j} + 4P_{ij} + P_{i-1,\,j} = (6AE/L)\,(\mu_{i-1,\,j} - \mu_{ij}) \qquad \text{(A4)}$$

$$q_{ij} = (Gt/b)\,(\mu_{ij} - \mu_{i,\,j+1}) \qquad \text{(A5)}$$

$$P_{i+1,\,j} - P_{ij} + (q_{ij} - q_{i,\,j-1})L = 0 \qquad \text{(A1)}$$

The μ's can be eliminated between Eqs. (A4) and (A5) to obtain

$$(L/6AE)\,(P_{i+1,\,j+1} + 4P_{i,\,j+1} + P_{i-1,\,j+1} - P_{i+1,\,j} - 4P_{ij} - P_{i-1,\,j}) = (b/Gt)(q_{ij} - q_{i-1,\,j}) \qquad \text{(A6)}$$

Now the q's can be eliminated between Eq. (A6) and Eq. (A1). This results in

$$6B\Delta_{ii}P_{ij} + \Delta_{jj}\,(P_{i+1,\,j} + 4P_{ij} + P_{i-1,\,j}) = 0 \qquad \text{(A7)}$$

where

$$B = (E/G)\,(A/bt)\,(b^2/L^2)$$

Or the P's can be eliminated between Eq. (A6) and Eq (A1), resulting in

$$6B\Delta_{ii}\,q_{ij} + \Delta_{jj}(q_{i+1,\,j} + 4q_{ij} + q_{i-1,\,j}) = 0 \qquad \text{(A8)}$$

Eqs. (A7) or (A8) are the homogeneous partial difference equations that govern the stringer loads and the shear flows in a sheet-stringer panel with rigid ribs. The solution to only one of these equations is required, for, if the stringer loads are known, the shear flows can be obtained by statics and vice versa. Solutions to

Eq. (A7) will be obtained in this report. Eq. (A8) will not be used.

Solution for Concentrated Perturbation Load

One method of obtaining the solution to Eq. (A7) for the loading of Fig. 2(a) will be presented. Define the function

$$h_i(x) = \sum_{j=-\infty}^{\infty} P_{ij} \cos jx \tag{A9}$$

Multiply Eq. (A9) by cos lx and integrate from 0 to π. This gives

$$\int_0^\pi h_i(x) \cos lx \, dx = \sum_{j=-\infty}^{\infty} \int_0^\pi P_{ij} \cos jx \cos lx \, dx \tag{A10}$$

The orthogonality relation is

$$\int_0^\pi \cos jx \cos lx = \frac{\pi}{2} \delta_{jl}$$

for j and $l \neq 0$. When $j = l = 0$,

$$\int_0^\pi \cos jx \cos lx \, dx = \int_0^\pi dx = \pi$$

By symmetry, it is seen from Fig. 2(a) that

$$P_{ij} = P_{i,-j}$$

Therefore, the sum on the right-hand side of Eq. (A10) is simply πP_{il}. A contribution of $(\pi/2)P_{il}$ is obtained at $-l$ and, similarly, at $+l$. At $l = 0$, the sum is the full πP_{il} immediately. Thus, Eq. (A10) becomes

$$\int_0^\pi h_i(x) \cos jx \, dx = \pi P_{ij} \tag{A11}$$

The function $h_i(x)$ is determined in the following manner: Multiply the difference equation, Eq. (A7), by cos jx and sum over j from $-\infty$ to ∞.

$$\sum_{j=-\infty}^{\infty} 6B\Delta_{ii}P_{ij} \cos jx + \sum_{j=-\infty}^{\infty} \Delta_{jj} (P_{i+1,\,j} + 4P_{ij} + P_{i-1,\,j}) \cos jx = 0 \tag{A12}$$

Let

$$\rho_{ij} = P_{i+1,\,j} + 4P_{ij} + P_{i-1,\,j}$$

Using the following equations,

$$\sum_{j=-\infty}^{\infty} \rho_{i,\,j+1} \cos jx = \sum_{j=-\infty}^{\infty} \rho_{ij} \cos (j-1)x = \sum_{j=-\infty}^{\infty} \rho_{ij} (\cos jx \cos x + \sin jx \sin x)$$

$$\sum_{j=-\infty}^{\infty} \rho_{i,\,j-1} \cos jx = \sum_{j=-\infty}^{\infty} \rho_{ij} \cos (j+1)x = \sum_{j=-\infty}^{\infty} \rho_{ij} (\cos jx \cos x - \sin jx \sin x)$$

Eq. (A12) can be written

$$6B\Delta_{ii}h_i(x) + 2(\cos x - 1) \times [h_{i+1}(x) + 4h_i(x) + h_{i-1}(x)] = 0$$

or

$$h_{i+1}(x) + h_i(x) \cdot 2\gamma(x) + h_{i-1}(x) = 0 \tag{A13}$$

where

$$\gamma(x) = \frac{-3B + 2(\cos x - 1)}{3B + (\cos x - 1)} \tag{A14}$$

The general solution to Eq. (A13) is

$$h_i = c_i(-\gamma + \sqrt{\gamma^2 - 1})^i + c_2(-\gamma - \sqrt{\gamma^2 - 1})$$

Inspection of Eq. (A14) shows that $|\gamma| \geq 1$. Further, the condition

$$\lim_{i \to \infty} h_i(x) = 0$$

must hold. So the required solution of Eq. (A13) is, for $\gamma \geq 1$,

$$h_i = c_1(-\gamma + \sqrt{\gamma^2 - 1})^i$$

for $\gamma \leq -1$,

$$h_i = c_2(-\gamma - \sqrt{\gamma^2 - 1})^i$$

For convenience this solution can be written in the equivalent form: for $\gamma \geq 1$,

$$h_i = (-1)^i Ce^{-\lambda i}$$

for, $\gamma \leq -1$,

$$h_i = Ce^{-\lambda i} \tag{A15}$$

where

$$\lambda = \cosh^{-1} |\gamma| \tag{A16}$$

where the positive value of the inverse hyperbolic cosine is taken.

For all of the values of B in Tables 1–5, the values of $\gamma(x)$ are less than -1; thus, the second of Eqs. (A15) is used exclusively.

The coefficient $C(x)$ can be determined from the conditions at rib 0, the rib at which the load is applied. Along rib 0, stringer loads are zero everywhere except for $j = 0$. At $j = 0$ the stringer load is $p/2$. Along rib $i = 0$; then, Eq. (A9) gives

$$h_0(x) = p/2$$

From Eq. (A15),

$$h_0(x) = p/2 = C(x)e^{-\lambda(x) \cdot 0}$$

So,

$$C(x) = p/2, \text{ a constant}$$

Then,

$$h_i(x) = (p/2)e^{-\lambda(x)i}$$

and P_{ij} is given by Eq. (A11) as

$$P_{ij} = \frac{p}{2\pi} \int_0^{\pi} e^{-\lambda(x)i} \cos jx \, dx \qquad \text{(A17)}$$

Using

$$e^{-\lambda(x)} = \cosh \lambda(x) - \sinh \lambda(x) = -\gamma(x) - \sqrt{\gamma^2(x) - 1}$$

Eq. (A17) can be written in the form

$$P_{ij} = \frac{p}{2\pi} \int_0^{\pi} \left[\frac{1}{3B + 2 \sin^2 (x/2)} \left(3B + 4 \sin^2 \frac{x}{2} - 2 \sin (x/2) \sqrt{9B + 3 \sin^2 \frac{x}{2}} \right) \right]^i \cos jx \, dx \qquad \text{(A18)}$$

Solution for Distributed Perturbation Load

In order to obtain the solution for a loading of the type shown in Fig. 2(c), the effect of this load on Eq. (A7) must be examined. From Fig. 9(b), equilibrium of the loaded portion of stringer 0 gives

$$P_{10} - P_{00} + (q_{00} - q_{0,-1})L = qL \qquad \text{(A19)}$$

Eq. (A1) holds in the balance of the panel. Writing Eq. (A6) for $i = 1$, $j = 0$ and eliminating the q's between the resulting equation and Eq. (A19) yields

$$6B\Delta_{ii}P_{10} + \Delta_{jj}(P_{20} + 4P_{10} + P_{00}) = -6BqL \qquad \text{(A20)}$$

Similarly, writing Eq. (A6) for $i = 0$, $j = 0$ and combining with Eq. (A19) yields

$$6B\Delta_{ii}P_{00} + \Delta_{jj}(P_{10} + 4P_{00} + P_{-1,0}) = 6BqL \qquad \text{(A21)}$$

It is permissible to consider $i > 0$ because the solution for $i \leq 0$ is exactly the same as that for $i > 0$ except the sign is reversed throughout the region $i \leq 0$. Eq. (A7) now becomes, for $i = 1$,

$$6B\Delta_{ii}P_{1j} + \Delta_{jj}(P_{2j} + 4P_{1j} + P_{0j}) = -6BqL\delta_{j0} \qquad \text{(A22)}$$

and for $i > 1$,

$$6B\Delta_{ii}P_{ij} + \Delta_{jj}(P_{i+1,j} + 4P_{ij} + P_{i-1,j}) = 0 \qquad \text{(A23)}$$

Define

$$k_i(x) = \sum_{j=-\infty}^{\infty} P_{ij} \cos jx \qquad \text{(A24)}$$

similar to the $h_i(x)$ of Eq. (A9). As before, the equation

$$\pi P_{ij} = \int_0^{\pi} k_i(x) \cos jx \, dx \qquad \text{(A25)}$$

is obtained. Using Eq. (A23) as before, the difference equation

$$k_{i+1}(x) + k_i(x) \cdot 2\gamma(x) + k_{i-1}(x) = 0 \qquad \text{(A26)}$$

results. The solution to Eq. (A26) can be written as the second of Eqs. (A15)

$$k_i(x) = C'(x)e^{-\lambda(x)\,i} \qquad \text{(A27)}$$

where $\lambda(x)$ is given by Eq. (A16).

The coefficient $C'(x)$ is found by use of Eq. (A22). Multiply Eq. (A22) by $\cos jx$ and sum from $-\infty$ to ∞. This yields

$$\sum_{j=-\infty}^{\infty} 6B\Delta_{ii}P_{ij} \cos jx + 2(\cos x - 1) \sum_{j=-\infty}^{\infty} (P_{2j} + 4P_{1j} + P_{0j}) \cos jx = -6BqL$$

which can be written as

$$6B\Delta_{ii}k_i(x) + 2(\cos x - 1)\,[k_2(x) + 4k_1(x) + k_0(x)] = -6BqL \qquad \text{(A28)}$$

From Fig. 2(c) it is seen that

$$P_{1j} = -P_{0j}$$

by symmetry. Therefore, from Eq. (A24),

$$k_1(x) = -k_0(x)$$

Using this symmetry relation in Eq. (A28) gives

$$6B[k_2(x) - 3k_1(x)] + 2(\cos x - 1)\,[k_2(x) + 3k_1(x)] = -6BqL$$

Substituting from Eq. (A27), the coefficient $C'(x)$ is obtained

$$C'(x) = \frac{-6BqL}{e^{-\lambda}\{e^{-\lambda}[6B + 2(\cos x - 1)] + 6(\cos x - 1) - 18B\}}$$

Substituting back into Eq. (A25),

$$P_{ij} = \frac{1}{\pi}\int_0^{\pi} \frac{-6BqLe^{-\lambda\cdot(i-1)}\cos jx\,dx}{e^{-\lambda}\,[6B + 2(\cos x - 1)] + 6\,(\cos x - 1) - 18B}$$

which can be transformed to

$$P_{ij} = \frac{3BqL}{2\pi}\int_0^{\pi} \frac{e^{-\lambda\cdot(i-1)}\cos jx\,dx}{3B + \sin^2(x/2) + \sin(x/2)\sqrt{9B + 3\sin^2(x/2)}} \qquad \text{(A29)}$$

It is possible to carry out the integration of Eqs. (A18) and (A29) in terms of elementary functions for the special case of $i = 1$ and for all j. However, the resulting expressions are not practical for computations when j is greater than 5 or 6 because they involve small differences of large numbers, and, consequently, there is a drastic loss in the number of significant figures. Integration of these expressions [Eqs. (A18) and (A29)] for other values of i is difficult.

These obstacles can be avoided, however. From Eq. (A17), for instance, note that the P_{ij}'s for a concentrated perturbation can be thought of, except for a constant factor, as coefficients of the Fourier cosine series in the interval 0 to 2π of the function that takes the values

$$e^{-\lambda(x)\cdot i} \qquad \text{(A30)}$$

between 0 and π and is constructed symmetric about π. Similarly, for the distributed perturbation loading, the P_{ij}'s are essentially coefficients of the Fourier cosine series in the interval 0 to 2π of the function that takes the values

$$\frac{e^{-\lambda(x)\cdot(i-1)}}{3B + \sin^2(x/2) + \sin(x/2)\sqrt{9B + 3\sin^2(x/2)}} \qquad \text{(A31)}$$

between 0 and π and is symmetric about π.

The stringer loads in parts (a) and (b) of Tables 1–5 were computed by means of harmonic analysis of the functions (A30) and (A31) based on a collocation procedure utilizing 24 points in the interval 0 to π (or 48 points in the interval 0 to 2π). This procedure was adapted from reference 6. Shear flows were obtained from statics with the use of Eqs. (A1) and (A19). Parts (c) of Tables 1–5 were obtained by the appropriate superposition of the solutions for distributed perturbation loads.

References

[1] Kuhn, Paul, and Moggio, Edwin M., *Stresses Around Rectangular Cutouts in Skin-Stringer Panels Under Axial Loads—I*, NACA Wartime Report L-399, June, 1942.

[2] Kuhn, Paul, Duberg, John E., and Diskin, Simon H., *Stresses Around Rectangular Cutouts in Skin-Stringer Panels Under Axial Loads—II*, NACA Wartime Report L-368, October, 1943.

[3] Kuhn, Paul, Rafel, Norman, and Griffith, George E., *Stresses Around Rectangular Cutouts with Reinforced Coaming Stringers*, NACA TN 1176, January, 1947.

[4] Morley, L. S. D., *Load Distribution and Relative Stiffness Parameters for a Reinforced Flat Plate Containing a Rectangular Cutout Under Plane Loading*, Rep. S.347. Nationaal Luchtvaartlaboratorium, Amsterdam, Reports and Transactions, Vol. XV, 1949.

[5] Cicala, P., *Effects of Cutouts in Semimonocoque Structures*, Journal of the Aeronautical Sciences, Vol. 15, No. 3, pp. 171–179, March, 1948.

[6] Whittaker, E. T., and Robinson, G., *The Calculus of Observations*, Chapt. X; Blackie and Son, Ltd., London and Glasgow, 1932.

Oscillating Airfoils at High Mach Number

M. J. LIGHTHILL*

University of Manchester, England

SUMMARY

A simple formula is given for the pressure distribution on an oscillating airfoil in two-dimensional flow at high Mach Number. The formula is expected to be reasonably accurate if the pressure on the surface remains within the range 0.2 to 3.5 times the mainstream pressure. To illustrate the application of the formula, some results for symmetrical airfoils performing pitching oscillations are obtained and compared with results obtained from existing theories in the case of high Mach Number.

NOTATION

x	= coordinate parallel to undisturbed stream
y	= coordinate perpendicular to undisturbed stream, measured *away* from airfoil on each side of it
y	= $Y(x, t)$ = equation of airfoil surface (upper or lower) at time t
U	= velocity of undisturbed stream
p_1, ρ_1, a_1	= pressure, density, velocity of sound, respectively, in undisturbed stream
M	= U/a_1 = Mach Number of undisturbed stream
w	= "effective piston velocity" = $(\partial Y/\partial t) + (U\partial Y \div \partial x)$
ϵ	= maximum displacement in airfoil oscillation
$\omega/2\pi$	= frequency of airfoil oscillation
c	= airfoil chord
δ	= maximum inclination of airfoil surface to the stream
p	= pressure at point on airfoil surface
γ	= ratio of specific heats (assumed constant)
y	= $Y_s(x) \pm Y_t(x, t)$ = equation of $\left(\begin{smallmatrix}\text{lower}\\ \text{upper}\end{smallmatrix}\right)$ surface of symmetrical oscillating airfoils
w_s, w_t	= values of w resulting from Y_s, Y_t, respectively
Δp	= pressure on lower surface minus pressure at same point on upper surface
$\alpha(t)$	= variable angle of attack (in pitching oscillations)
m	= nose-up moment of aerodynamic forces per unit span about axis of pitching oscillations
m_α, $m_{\dot\alpha}$	= coefficients defined as $(1/\rho_1 U_1^2 c^2)\ (\partial m/\partial\alpha)_{\alpha=\dot\alpha=0}$ and $(1/\rho_1 U_1 c^3)\ (\partial m/\partial\dot\alpha)_{\alpha=\dot\alpha=0}$
τ	= thickness-chord ratio
x_θ	= distance of axis of pitching oscillations behind leading edge
h	= ratio of x_θ to c

Basic formula: In motions with M large and $M[\delta + (\epsilon/c) \times (\omega c/U)] < 1$, the surfaces pressures are given to good approximation by the equation

$$\frac{p}{p_1} = 1 + \gamma\frac{w}{a_1} + \frac{\gamma(\gamma+1)}{4}\left(\frac{w}{a_1}\right)^2 + \frac{\gamma(\gamma+1)}{12}\left(\frac{w}{a_1}\right)^3$$

(1) INTRODUCTION

A THEORY OF OSCILLATING AIRFOILS in supersonic flow is needed, but a completely linearized theory has proved too inaccurate. Some second-order terms (part of an ascending series for them, in powers of the frequency parameter) have been found by Wylly[1] and by Van Dyke,[2] but their methods are complicated, and unfortunately their answers do not agree. The method of Jones and Skan[3] takes the thickness of the airfoil into account to higher order but not the amplitude of the oscillations; this method calls for an extensive program of computation in any one case. In this state of affairs it seems worth pointing out that, in the special case of high Mach Number, there is a simple theory that should give fairly accurate results (better than second-order) even when disturbances are rather large.

In two-dimensional flow past an airfoil at high Mach Number, say $M \geq 4$, the shock waves and expansion waves are set at small angles to the undisturbed flow. Two consequences of this are worth special notice.

(a) Gradients in the direction of the undisturbed flow are small compared with gradients perpendicular to it.

(b) Because velocity components parallel to shock waves or expansion waves are not changed by them, the velocity components perpendicular to the flow are large compared with the *disturbances* to components parallel to it.

Both these facts contribute to the truth of Hayes's result[4] that, to a good approximation, *any plane slab of fluid, initially perpendicular to the undisturbed flow, remains so as it is swept downstream and moves in its own plane under the laws of one-dimensional unsteady motion.*

Goldsworthy[5] showed that the relative error in this result of Hayes should be of order $1/M^2$, both causes (a) and (b) above contributing a factor $1/M$. Here it is assumed that $M\delta$ is bounded, say less than 1, where δ is the maximum inclination (in radians) of the airfoil surface to the stream. This condition, he points out, would in most practical applications need to be satisfied from considerations of drag.

Now the result in italics must remain true even if the whole flow is unsteady—for example, if the airfoil oscillates. This is so evident physically from (a) and (b) above† that its mathematical deduction from the equations of motion, an easy extension of Goldsworthy's work, is here omitted.

Now as the slab of fluid moves downstream with approximately the velocity U of the undisturbed flow,

Received December 10, 1952.

* Professor of Applied Mathematics.

† Note that it is of little importance to such a slab of fluid, while it is being deformed by the wall, whether or not earlier slabs have been subjected to the same deformations.

the position of the piece of solid wall bounding it will move normal to the stream with a velocity

$$w = (\partial Y/\partial t) + U(\partial Y/\partial x) \tag{1}$$

where $y = Y(x, t)$ is the equation of the upper or lower surface of the airfoil, with y measured away from the airfoil in each case.

Accordingly, the problem of determining the forces on the oscillating airfoil at high Mach Number reduces, as in the steady case, to the one-dimensional flow problem of finding the pressure on a piston moved, with a given dependence of velocity w on time, into otherwise undisturbed fluid.

This, by comparison, is a not too complicated problem. It becomes particularly simple if a condition like Goldsworthy's is imposed (as indeed it must if the statement in italics is to be at all accurate)—namely, that the magnitude $|w|$ of the piston velocity, Eq. (1), never exceeds the speed of sound in the undisturbed fluid. In an oscillation with maximum displacement ϵ and frequency $\omega/2\pi$, this condition can be written

$$\epsilon\omega + U\delta < a_1 \tag{2}$$

where δ, as before, is the maximum inclination of the airfoil surface to the stream. This condition could be rewritten

$$M[\delta + (\epsilon/c)\ (\omega c/U)] < 1 \tag{3}$$

where $M = U/a_1$ is the Mach Number and c is the chord, so that $\omega c/U$ is the frequency parameter. Evidently, condition (3) might well be satisfied in practical problems. (The theory would still have value as a rough approximation even if the left-hand side somewhat exceeded 1.) As will be seen below, it permits compression up to three and one-half times and rarefaction down to one-fifth of the undisturbed pressure.

The advantage of imposing this condition is that the pressure on the piston then depends, with fair accuracy, only on its instantaneous velocity. The pressure distribution is in fact a simple function of the piston velocity w, given by Eq. (1).

When there is no shock wave, indeed, this is true *without* any restriction on amplitude, and the pressure is given by the "simple wave" condition

$$\frac{p}{p_1} = \left(1 + \frac{\gamma - 1}{2}\frac{w}{a_1}\right)^{2\gamma/(\gamma-1)} \tag{4}$$

where γ is the ratio of the specific heats (assumed constant). When there is an initial shock wave (because the piston moves initially with finite velocity into the fluid), Eq. (4) can be improved by use of the "shock-expansion" theory, which takes into account the exact pressure change at the shock [which is less than Eq. (4)] and assumes a simple wave (i.e., neglects lateral entropy *gradients*) behind the shock. But this theory gives pressures depending not only on the instantaneous value of w/a_1 but also on the value that w/a_1 had when the shock wave was produced.

TABLE 1

w/a_1	Simple Wave	Shock Expansion	Quadratic	Cubic
1	3.583	3.473	3.240	3.520
0.5	1.949	1.916	1.910	1.945
0	1.000	1.000	1.000	1.000
−0.5	0.478	0.488	0.510	0.475
−1	0.210	0.220	0.440	0.160

In Table 1 is shown the dependence on w/a_1 (for $\gamma = 1.4$) of (a) the simple wave expression, Eq. (4), for p/p_1; (b) the value of p/p_1 on "shock-expansion" theory, taking the shock at its maximum permitted strength, corresponding to $w/a_1 = 1$; (c) the "Busemann" quadratic approximation—namely, the first three terms of the binomial expansion of Eq. (4); (d) the cubic approximation (first four terms of the expansion)—namely,

$$\frac{p}{p_1} = 1 + \gamma\frac{w}{a_1} + \frac{\gamma(\gamma+1)}{4}\left(\frac{w}{a_1}\right)^2 + \frac{\gamma(\gamma+1)}{12}\left(\frac{w}{a_1}\right)^3 \tag{5}$$

Since for a given value of w/a_1 the value of p/p_1 may vary continuously between the extremes of the "simple wave" and "shock-expansion" values (as the value of w/a_1 at the shock varies from 0 to 1), any approximate value that always lies reasonably close to both is acceptable. The cubic approximation, for example, which is always within 0.06 p_1 of both values (not a great error where such large pressure differences are occurring), even if w/a_1 is as high as 1, is in many ways to be preferred even to the exact simple wave value, which is in error by 0.11 p_1 immediately behind the shock wave. Since, also, the cubic is reasonably simple, it will here be adopted. (Note that cubic terms in the expansion of pressure ratio in a simple wave have often been discarded on the grounds that their coefficient is not the same as in the expansion of the pressure ratio through a shock; however, the coefficient in the latter case is $\gamma(\gamma+1)^2/32$, which differs from that in Eq. (5) by only 10 per cent for $\gamma = 1.4$, so that the terms are well worth retaining.)

Finally, then, the pressure at any point on an oscillating airfoil will be taken as given by the cubic (5) in w/a_1, where w is defined in terms of the equation $y = Y(x, t)$ of the airfoil surface by means of Eq. (1).*

It is unnecessary for the author to make extensive calculations here on the basis of the postulated pressure distribution, since it is a simple matter for anyone concerned in technical applications to make use of it to obtain any particular results he may need on the pres-

* It should be noted that a formula of somewhat similar character was suggested by Jones[6] as an empirical approximation for general M. The present work indicates that Jones's formula is right for large M, and so gives it some added support.

sure forces acting on oscillating airfoils under the conditions here treated. Some specimen results will, however, be displayed and compared with existing theories.

(2) Symmetrical Airfoils

Supersonic airfoils are usually symmetrical, so that at zero angle of attack the equation of both surfaces [with y measured away from the airfoil in each case, as in Section (1)] is the same, say $y = Y_s(x)$. Changes in y due to oscillations, whether pitching or bending, will have opposite sign on both sides, say $Y_i(x, t)$ on the lower surface and $-Y_i(x, t)$ on the upper surface. The full equation of both surfaces is then

$$y = Y_s(x) \pm Y_i(x, t) \quad \begin{cases} \text{lower surface} \\ \text{upper surface} \end{cases} \tag{6}$$

Hence, by Eq. (1),

$$w = UY_s'(x) \pm \left(\frac{\partial Y_i}{\partial t} + U\frac{\partial Y_i}{\partial x}\right) = w_s(x) \pm w_i(x, t) \tag{7}$$

Now in many problems one would wish to know not the pressure distribution, Eq. (5), on each surface but only the load distribution, obtained by subtracting the pressure distribution on the upper surface from that on the lower surface. This is

$$\frac{\Delta p}{p_1} = 1 + \gamma\frac{w_s + w_i}{a_1} + \frac{\gamma(\gamma+1)}{4}\left(\frac{w_s + w_i}{a_1}\right)^2 + \frac{\gamma(\gamma+1)}{12}\left(\frac{w_s + w_i}{a_1}\right)^3 - 1 + \gamma\frac{w_s - w_i}{a_1} - \frac{\gamma(\gamma+1)}{4}\left(\frac{w_s - w_i}{a_1}\right)^2 - \frac{\gamma(\gamma+1)}{12}\left(\frac{w_s - w_i}{a_1}\right)^3$$

$$= \left[2\gamma + \gamma(\gamma+1)\frac{w_s}{a_1} + \frac{\gamma(\gamma+1)}{2}\left(\frac{w_s}{a_1}\right)^2\right]\frac{w_i}{a_1} + \frac{1}{6}\gamma(\gamma+1)\left(\frac{w_i}{a_1}\right)^3 \tag{8}$$

As would be expected, there are no terms in the square of the oscillatory part w_i of w. The main effect of nonlinearity is to change the coefficient of w_i/a_1 by a factor depending on Mach Number and on the local slope of the airfoil contour.

It will be sufficient as an example to consider a pitching oscillation, say one about the axis $x = x_0$, $y = 0$, with variable angle of attack $\alpha(t)$. Then

$$Y_i(x, t) = \alpha(t)(x - x_0), \qquad w_i = \dot{\alpha}(x - x_0) + U\alpha \tag{9}$$

Substituting also for w_s in Eq. (8), it becomes

$$\frac{\Delta p}{p_1} = \left[2\gamma + \gamma(\gamma+1)MY_s'(x) + \frac{\gamma(\gamma+1)}{2}M^2Y_s'^2(x)\right]\left[\frac{\dot{\alpha}(x - x_0)}{a_1} + M\alpha\right] + \frac{\gamma(\gamma+1)}{6}\left[\frac{\dot{\alpha}(x - x_0)}{a_1} + M\alpha\right]^3 \tag{10}$$

The terms in (10) which are linear in α and $\dot{\alpha}$ are especially important for determining the aerodynamic stiffness and damping, respectively, of the oscillation. The stiffness is the coefficient of α, and the damping is that of $\dot{\alpha}$, in the nose-down moment,

$$-m = \int_0^c (x - x_0)\Delta p\, dx \tag{11}$$

of the load distribution about the axis $x = x_0$. (Here, c is the chord.)

Thus, by Eq. (10), the aerodynamic stiffness coefficient is

$$-m_\alpha = \frac{1}{\rho_1 U_1^2 c^2}\left(-\frac{\partial m}{\partial \alpha}\right)_{\alpha=\dot{\alpha}=0} = \frac{1}{Mc^2}\int_0^c (x - x_0)\left[2 + (\gamma+1)MY_s'(x) + \frac{\gamma+1}{2}M^2Y_s'^2(x)\right]dx \tag{12}$$

and the aerodynamic damping coefficient is

$$-m_{\dot{\alpha}} = \frac{1}{\rho_1 U_1 c^3}\left(-\frac{\partial m}{\partial \dot{\alpha}}\right)_{\alpha=\dot{\alpha}=0} = \frac{1}{Mc^3}\int_0^c (x - x_0)^2\left[2 + (\gamma+1)MY_s'(x) + \frac{\gamma+1}{2}M^2Y_s'^2(x)\right]dx \tag{13}$$

The latter is essentially positive—that is, there is always damping at high Mach Number. (This is obvious from the point of view of this paper, the damping being essentially the radiation damping of a piston in air.)

To fix the ideas still further, consider a biconvex airfoil of thickness-chord ratio τ, given by the equation

$$Y_s(x) = 2\tau[x - (x^2/c)] \tag{14}$$

(Note that, by the restriction (3), we must have $\tau < (2M)^{-1}$ even for small oscillations; somewhat less latitude can be allowed if the oscillations are large.) Then writing $x_0/c = h$ for the position of the axis of pitching oscillations relative to the chord, Eqs. (12) and (13) become

$$-m_\alpha = \frac{1}{M}\left\{1 - \frac{1}{3}(\gamma+1)M\tau + \frac{1}{3}(\gamma+1)M^2\tau^2 - h\left[2 + \frac{2}{3}(\gamma+1)M^2\tau^2\right]\right\} \tag{15}$$

$$-m_{\dot\alpha} = \frac{1}{M}\left\{\frac{2}{3} - \frac{1}{3}(\gamma+1)M\tau + \frac{4}{15}(\gamma+1)M^2\tau^2 - 2h\left[1 - \frac{1}{3}(\gamma+1)M\tau + \frac{1}{3}(\gamma+1)M^2\tau^2\right] + h^2\left[2 + \frac{2}{3}(\gamma+1)M^2\tau^2\right]\right\} \tag{16}$$

The value of h for which Eq. (15) vanishes, corresponding to the aerodynamic center, is tabulated against $M\tau$ for $\gamma = 1.4$ in Table 2. This table also gives the value of $-m_{\dot\alpha}$ in the special case ($h = 0.5$) of oscillations about an axis at mid-chord, when

$$-m_{\dot\alpha} = \frac{1}{M}\left(\frac{1}{6} + \frac{1}{10}(\gamma+1)M^2\tau^2\right) \tag{17}$$

Now the expression given by Wylly[1] for this last quantity is, in our notation,

$$-m_\alpha = \frac{M^2-2}{6(M^2-1)^{5/2}} + \frac{\tau}{6(M^2-1)^3}\left[4M^6 + (2\gamma-16)M^4 + (\gamma+19)M^2 - 4\right] \tag{18}$$

This gives, as $M \to \infty$ for fixed $M\tau$,

$$-m_{\dot\alpha} \sim (1/M)\,[(1/6) + (2/3)M\tau] \tag{19}$$

Now Wylly does not retain terms of high enough order to give a term in $M^2\tau^2$ in $-Mm_{\dot\alpha}$, but the coefficient of $M\tau$ ought to be correct. However, it is seen from Eq. (17) that, in this case of $h = 0.5$, the coefficient of $M\tau$ in $-Mm_{\dot\alpha}$ for large M should be zero.

The theory of Section (1), if no slip has been made (and it is very simple), must give correctly the asymptotic form as $M \to \infty$ of any term of second order in the disturbances, since there is no difference between the simple wave and shock-expansion theories to this order. (In contrast, the third-order terms, which have been retained, should merely improve the accuracy, without being mathematically exact.) Therefore, the conclusion seems inescapable that some error has crept into Wylly's calculations.

Van Dyke's expression[2] for the pressure on the upper surface may be written, in our notation, as

$$\frac{p}{p_1} = 1 + \frac{\gamma M}{(M^2-1)^{1/2}}\left(\frac{w_s - w_i}{a_1}\right) + \frac{(1/4)\gamma(\gamma+1)M^4 - \gamma M^2 + \gamma}{(M^2-1)^2}\left(\frac{w_s^2 - 2w_s w_i}{a_1^2}\right) + \frac{\gamma\dot\alpha}{a_1}\left\{\frac{M}{(M^2-1)^{1/2}}x + \frac{M^2[2+(\gamma-1)M^2]}{(M^2-1)^3}\left[MY_s(x) + \frac{1}{2}xMY_s'(x)\right]\right\} \tag{20}$$

To obtain this result, he neglects w_i^2 and all the third-order terms and takes the limit as the frequency parameter tends to zero. For large M the last term in Eq. (20) vanishes, and the rest becomes identical with the basic formula of this paper (which holds independently of frequency parameter) if, in it, all second-order terms except w_i^2, but no third-order terms, are included. This constitutes a valuable check on Van Dyke's work.

The greatest Mach Number for which Jones and Skan[3] have carried out their calculations is $M = 2$, at which poor agreement with the present theory would be expected. However, their results do agree with it in predicting that the dependence of $-m_{\dot\alpha}$ on the thickness-chord ratio τ for oscillations of a biconvex airfoil about a mid-chord axis becomes negligible (for moderate τ) at $M = 2$. Indeed, their actual values of $-m_{\dot\alpha}$ (from 0.062 to 0.072 as the frequency parameter varies from 0 to 0.75), do not differ enormously from Eq. (17), which has the value 0.084 (independent of frequency parameter). Since the Jones and Skan values for $-m_{\dot\alpha}$ are expected to have good accuracy, this result at a moderate Mach Number augurs well for the present

TABLE 2

Distance of Aerodynamic Center from Leading Edge as Fraction of Chord, and Aerodynamic Damping Coefficient for Pitching Oscillations About a Mid-Chord Axis, as Functions of the Product of Mach Number and Thickness-Chord Ratio for a Biconvex Airfoil at High Mach Number

$M\tau$	0	0.1	0.2	0.3	0.4	0.5
$[h]_{m_\alpha=0}$	0.500	0.460	0.422	0.388	0.358	0.333
$[-m_{\dot\alpha}]_{h=0.5}$	$\frac{0.167}{M}$	$\frac{0.169}{M}$	$\frac{0.176}{M}$	$\frac{0.188}{M}$	$\frac{0.205}{M}$	$\frac{0.227}{M}$

theory at the rather high Mach Numbers for which it was designed to work.

One may note, in conclusion, that of the cubic terms in α and $\dot{\alpha}$ in Eq. (10), not so far discussed, the one that will predominate when the frequency parameter is less than 1 is

$$(1/6)\gamma(\gamma + 1)M^3\alpha^3 \qquad (21)$$

This uniform load distribution along the airfoil constitutes a nonlinearity in the stiffness for a pitching oscillation, which will help to stabilize it when the axis is ahead of the mid-chord position (but may render possible some subharmonic resonance) and to destabilize it for axes to the rear of it.

References

[1] Wylly, A., *A Second-Order Solution for an Oscillating, Two-Dimensional, Supersonic Airfoil*, The RAND Corporation Report, California, 1951.

[2] Van Dyke, M., Private communication.

[3] Jones, W. P., and Skan, S. W., *Aerodynamic Forces on Bi-convex Aerofoils Oscillating in a Supersonic Airstream*, A.R.C. Reports 13162 and 14217 (limited circulation), to be published as A.R.C. R. & M. 2749.

[4] Hayes, W. D., Q. App. Math., Vol. 5, pp. 105–106, 1947.

[5] Goldsworthy, F. A., Q.J.M.A.M., Vol. 5, pp. 54–63, 1952.

[6] Jones, W. P., *The Influence of Thickness-Chord Ratio on Supersonic Derivatives for Oscillating Aerofoils*, A.R.C. Report 10871 (limited circulation), to be published as A.R.C. R. & M. 2679.

The Upwash Correction for an Oscillating Wing in a Wind Tunnel

(*Concluded from page 386*)

$$\int_0^\infty f(q)\, dq/(q \pm k)$$

If μ appears in the numerator and $(q + k)$ in the denominator, then, as $\mu \to 0$, the integral vanishes.

If μ appears in the numerator and $q - k$ in the denominator, then, as $\mu \to 0$, the integral vanishes everywhere except in a small region about $q = k$; here $f(q)$ may be replaced by $f(k)$ and brought outside the integral, provided $f(q)$ is continuous. The resulting integral may be evaluated, and then, as $\mu \to 0$ the result is $\pi f(k)$. This is a special case of Fourier's integral theorem.

The Contribution of Higher Mode Resonance to Helicopter Rotor-Blade Bending*

HAROLD HIRSCH†
Hughes Aircraft Company

ABSTRACT

Results obtained from flight tests of a family of main rotor blades, similar in all respects except flapwise bending stiffness, are reviewed with the objective of pointing out the role that resonant bending, particularly in the second and third bending modes, has been observed to play in determining the beam bending moments experienced by the test blades. It has been found that in certain critical conditions the contribution of higher mode bending to the total bending moment may be as great as the sum of the steady, first and second harmonic terms usually considered in current blade analysis methods. The source of the forces exciting the resonance has not been determined; however, it appears to be of aerodynamic origin.

The results call attention to the influence resonant bending may have in determining, from the fatigue point of view, the structural life of rotor blades. Since the blade resonant frequency in the second mode will, in general, lie between four and five times rotor speed and in the third mode between six and nine times rotor speed, the number of stress cycles experienced by the rotor blades will include corresponding multiples of the rotor rotation.

INTRODUCTION

DESPITE THE GREAT AMOUNT OF EFFORT already devoted to their study, there are many important helicopter problems that are still lacking final solution. Included among these are the interdependent problems of rotor dynamics, rotor-blade structural analysis, and helicopter stability and control. By applying mathematical methods and physical principles developed in the airplane and other fields, considerable progress has been made toward their solution. The principal shortcoming of methods for treating these problems is, in the present state of the art, a lack of adequate procedures for determining all important aerodynamic loads applied to the rotor. The practical problems that arise when attempting to predict realistically the aerodynamic loads result principally from two sources: the complexity of induced flow effects and the interdependent manner in which rotor-blade motions and structural deflections enter into the determination of the aerodynamic loads applied to the blade.

Recognizing the important role played by blade bending, several investigators have undertaken to introduce the effects of blade bending deflection into the analytical treatment of helicopter problems. Johnson and Mayne[1] have outlined two methods for introducing the inertial effects resulting from blade bending deflection into blade structural analyses. One method solves the problem by means of a lengthy "tabular-dynamic" method; the other obtains substantially the same results with much less work by multiplying the "static" blade moments by the amplification factor for a simple undamped single degree of freedom system. Winson[2] has proposed a method applicable to rigid rotor blades which takes into account the effect of first- and second-mode blade bending deflections in determining the blade aerodynamic loads. Flax and Goland[3] have described both tabular and amplification factor methods for introducing the additional inertia terms and the aerodynamic damping effects due to blade bending deflections into blade structural analysis procedures. Finally, Arnold and Goland[4] have developed a method that introduces the effects of blade flexibility into helicopter stability and control analyses.

Attention has been called to the foregoing references in order to show that awareness of the potential role that might be played by rotor-blade bending, particularly in the first bending mode, has existed for some time. However, the conclusions derived from these methods have been only as realistic as the assumptions on which they are based. In practice, this reduces to the fact that if knowledge of the important bending modes and their associated aerodynamic effects is not available—and that the role of these factors is, therefore, not included in the formulation of theory—theory will never, of itself, predict their existence. It is important, accordingly, that experimental information be made available which will show which effects are of practical importance and should be included in theoretical formulation. Further, if important phenomena are currently being overlooked because of the fact that they are not indicated by existing analytical methods, it is even more important that experimental programs be undertaken so that their existence will be discovered.

The research program from which the subject matter of this paper has been extracted was undertaken with the general objective of providing comprehensive experimental information that would satisfy the discussed need for factual data concerning rotors. Specific objectives of the program were to determine the

Presented at the Rotating Wing Aircraft Session, Twentieth Annual Meeting, I.A.S., New York, January 28–February 1, 1952. Revised and received March 13, 1953.

* This investigation was conducted under sponsorship of the Rotary Wing Branch, Propeller Laboratory, Wright Air Development Center.

† Work done while at Cornell Aeronautical Laboratory, Inc. Now Assistant Chief, Helicopter Research, Hughes.

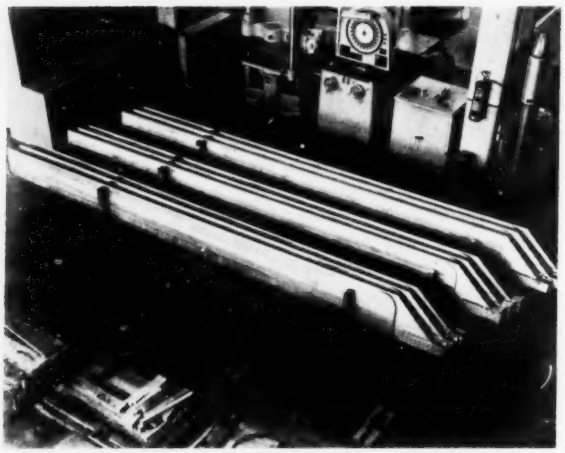

FIG. 1. The three sets of fiberglass skin and balsa-wood core blades flown in the program. Strain gages are wired through plastic tubes built into the blades.

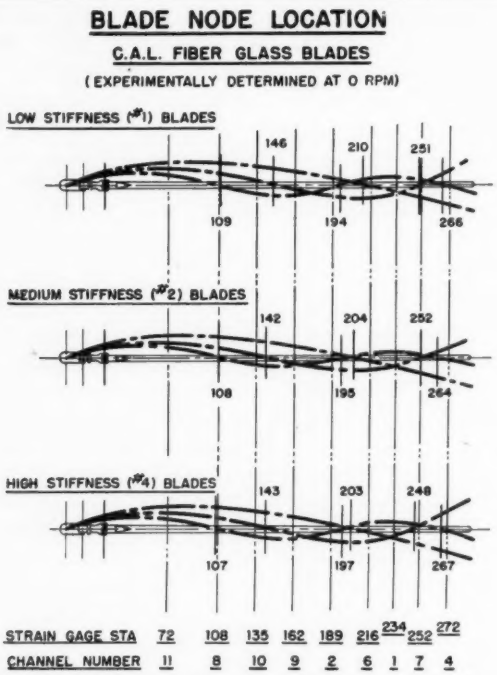

FIG. 2. Diagram showing node positions for each blade and giving blade spanwise stations for bending data channels. Stations are measured from the center of rotation.

bending moments and motions experienced in flight by articulated rotor blades and thereby to explore possible causes of a number of unexplained rotor-blade fatigue failures. It is believed that the program was highly successful in realizing its objectives, particularly since the fundamentally important rotor-blade resonance phenomenon described in this paper was disclosed in the course of the project. It is believed that the results obtained, in addition to clearly revealing the physical nature of the resonance problem, call attention to the need for re-evaluation, or extension, of current concepts of rotor dynamics and aerodynamics. Although the source of the forces exciting the measured resonances is not yet known, it is hoped that additional investigations will soon provide a satisfactory answer to this problem.

BACKGROUND

Program Initiation

The so-called "H-5 Variable Stiffness Blade Program," from which the results presented in this paper are extracted, was conceived and planned jointly by W.A.D.C. Rotary Wing Branch personnel and engineers of the Cornell Aeronautical Laboratory. Approaching the problem with the limited theoretical and experimental data then available, it is understandable that the existence of higher mode resonant bending was not foreseen at the time the program was undertaken. In fact, at the time there were no proved arguments to refute the popular opinion that the role of structural blade bending stiffness in determining blade motions and stresses was of secondary importance. This opinion, while now proved false as a generalization, can be justified with some logic for the case of first-mode bending by the fact that the centrifugal stiffening effect realized with normal blades will be four or five times as great as that due to their structural stiffness. In view of this fact and anticipating only quasi-static bending in the first bending mode, with some amplification, it was felt that the differences between data measured with blades possessing the limited amount of stiffness variation obtainable with conventional types of blade construction would be too small to be determined accurately. Design requirements were, therefore, established for blades that would provide a four-to-one stiffness range and still possess approximately the same mass and aerodynamic characteristics. Further, the blades were to possess one-half, one, and two times the stiffness of standard H-5 blades and be flyable on an H-5 helicopter. With a four-to-one stiffness range, it was anticipated that stiffness variation effects would be sufficiently large so that they could be measured.

Fiber-Glass Blade Design

Extensive preliminary studies[5] of various blade designs produced only one that met the four-to-one stiffness range requirement. The proposed design called for the development of three separate sets of blades, one of each stiffness, employing a fiber-glass shell, die molded integrally to a balsa-wood core. By employing the high strength-to-weight ratio of fiber glass, in conjunction with the ability to vary the elastic modulus of the fiber-glass skin by selectively orienting the fiber direction, the required stiffness range was provided. Whirl test blades were first constructed to prove the fiber-glass design, and, after they had successfully passed Propeller Laboratory tests, the three sets of

TABLE 1
Summary of Test Conditions Recorded

Blade	Flight Condition C.G. Position / Rotor r.p.m.	Level Flight						Climb		Autorotation	
		Forward				Aft		Forward	Aft	Forward	Aft
	μ	175	194	206	175	194	206	194	194	210	210
Medium-stiffness Cornell Aero. Lab. No. 2	0	X	X	X	X	X	X				
	0.05	X	X	X							
	0.10	X	O	X	X	X	X	X	X		
	0.15	X	X		X	X	X	X	X		X
	0.20	X	X	X	X	X	X	X	X		X
	0.25	X	X	X		X		X			
	0.30		X	X		X					
High-stiffness Cornell Aero. Lab. No. 4	0	X	X	X		X	X				
	0.05	X	X	X							
	0.10	X	O	X	X	X	X	X	X	X	X
	0.15	X	X	X		X		X	X	X	X
	0.20	X	X	X	X	X	X				
	0.25	X	X	X		X					
	0.30		X	X							
Low-stiffness Cornell Aero. Lab. No. 1	0	X	X	X	X	X	X				
	0.05		X			X					
	0.10	X	O	X	X	X	X				
	0.15	X	X	X	X	X					
	0.20	X			X						

X = test points recorded. O = Test points discussed in detail in this paper.

flight-test blades were fabricated. Detailed information concerning the design and manufacture of the fiberglass blades is given in references 6 and 7. A further description of the blades, together with an analysis of their mass, structural, and dynamic characteristics, is also available.[8] The finished appearance of the blades is shown in Fig. 1.

Flight-Test Program

In planning the flight program, an attempt was made to select a range of test variables sufficiently large so that the conditions investigated would be representative of both normal and abnormal operation. The steady-state program that was flown is shown by Table 1. Tests with the low-stiffness (No. 1) blades were not carried to high advance ratios or into climb and autorotation conditions. These tests were eliminated for reasons of safety, since resonant bending characteristics of the low-stiffness blades were particularly pronounced.

One blade of each stiffness was instrumented to measure bending at nine spanwise stations. The stations selected are shown in Fig. 2, which also shows experimentally determined stationary node locations for first-, second-, and third-mode bending. In addition to the beam bending traces, the test records contain traces for the pitch, flap, and lag motions of the instrumented blade. The load developed in the lag damper of the instrumented blade and the load due to blade pitching moment developed in the vertical control rod to each of the blades was also recorded. Only the blade bending data are considered in this paper.

Instrumentation

Since the variable stiffness program was largely concerned with interpretation of the differences between measured quantities rather than the absolute magnitude of the quantities, an important and effort-consuming part of the program consisted of the design, development, and accuracy investigations required to provide adequate instrumentation. Realizing that the program results would only be as reliable as the instrumentation, studies were undertaken for the purpose of evaluating alternative instrumentation possibilities. In these studies, emphasis was placed on devising a system that could simultaneously record as many as 28 channels of dynamic data measured on the rotating components of the rotor system. Results of the studies indicated that a multiplexing system—with the subcarrier oscillators, bridges, and amplifiers mounted on the rotating head—would satisfy the program requirements. In the completed system, the measured data, after being amplified and multiplexed, were transmitted to a ground-located receiving station where they were fed into analyzer circuits that resolved the combined signal into the individual data channels. Each channel was passed through a low-pass electrical filter to reduce hash and then was recorded on an

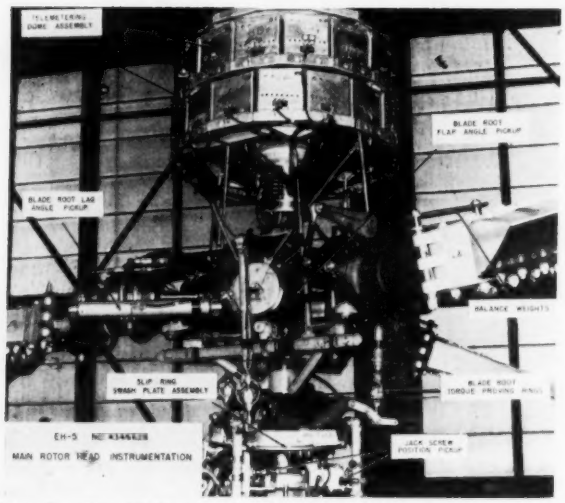
BLADE ROOT FLAP ANGLE PICKUP
BLADE ROOT LAG ANGLE PICKUP
BALANCE WEIGHTS
SLIP RING SWASH PLATE ASSEMBLY
BLADE ROOT TORQUE PROVING RING
EH-5 NO. 61345628
MAIN ROTOR HEAD INSTRUMENTATION
JACK SCREW POSITION PICKUP

FIG. 3. The 28-channel rotating telemetering dome assembly and blade root data pickups.

oscillograph. A view of the rotor head, telemetering dome assembly, and several data pickups is shown in Fig. 3. Detailed discussion of the design, operation, and accuracy of the instrumentation can be found in references 8 and 9.

The instrumentation developed was successfully employed in the program, contributing the following advantages:

(1) Substantial reduction in weight and size of airborne equipment.

(2) Elimination of unamplified signal transmission through slip rings.

(3) Reduction in number of slip rings required per channel.

(4) Simultaneous recording of a large number of channels.

(5) Continuous telemetering of flight information to the ground station, where engineers could observe the data that were being recorded. Malfunctioning equipment, off-scale traces, loss of signal, and excessive strains were often detected by ground observers while the flight was in progress, and corrective action was taken before data were recorded.

Disadvantages of the system consisted primarily of the need for excessive maintenance due to lack of ruggedness and temperature instability. Both of these shortcomings are attributed to the fact that the program did not allow for complete development of the system, rather than to any inherent system characteristic. In the program, correction for temperature drift was introduced in the data reduction procedure, using correction factors obtained from "calibrate inject" signals recorded before, during, and after each flight. Temperature instability was, however, a serious problem with the instrumentation. Experience based on this and other programs indicates that too much atten-

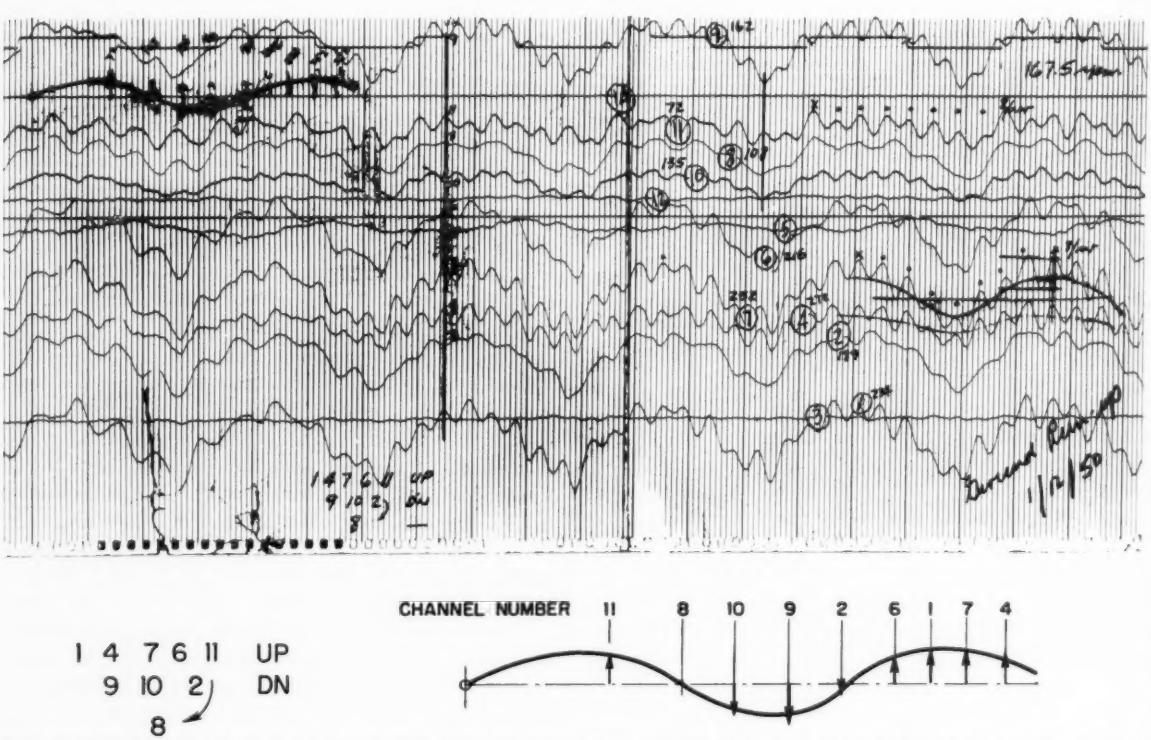

FIG. 4. Reproduction of blade shakedown oscillogram for the medium-stiffness blade from which higher (third-) mode resonant bending was first identified.

tion cannot be given to anticipating and eliminating temperature effects when designing flight-test instrumentation.

Discovery of Resonance Phenomenon

Prior to installation of the test instrumentation, each set of blades was subjected to ground and flight shakedown tests. Lacking instrumentation, these preliminary tests were evaluated on the basis of pilot's opinion. It was reported that the medium-stiffness (No. 2) blades appeared to possess normal characteristics. The high-stiffness (No. 4) blades were reported to be more responsive to the controls but, at times, somewhat "rough." The low-stiffness (No. 1) blades were judged to be slow to respond to control inputs and to be generally rough, often producing a cyclic stick "chatter" during the application of control motions and occasionally producing cyclic stick shake at high frequencies.

Being concerned with these observations concerning flight characteristics of the blades, it was decided that additional blade shakedown tests would be conducted when installation of the instrumentation was completed. Instrumentation was subsequently completed, and a ground run-up was made with the medium-stiffness blades. A section of the blade bending records obtained is reproduced in Fig. 4.

Glancing over the run-up record, it was observed that a periodic oscillation, prominent in the figure, was found to appear and disappear throughout the records. Noting the regularity of the oscillation and its uniform appearance, it was presumed that the instrumentation was malfunctioning. Since the oscillation appeared to be common to all bending channels, it was anticipated that the difficulty would be located in some part of the instrumentation carrying the multiplexed signal, such as the master amplifier or the radio links. A check showed, however, that all instrumentation was operating properly.

The oscillograph records were then more critically re-examined, revealing that in reality only nine of the 14 recording channels were oscillating. This might have been rationalized on the basis that the sensitivities of the remaining channels were too low to show the oscillation. It was also discovered, however, that at least one of the channels (No. 9) was unquestionably out of phase with the others, and it appeared that channel No. 10 was similarly out of phase.

Becoming aware that something unanticipated was taking place, an intuitive step was taken. Picking an instant, indicated by the vertical line drawn on the oscillogram, when the periodic trace displacements were maximum, the displacement direction of each trace was tabulated. It was noted that the higher order content of trace No. 2 was small and that trace No. 8 appeared to be relatively free of higher order components. It was also observed that the higher order component in all cases appeared to be eighth order.

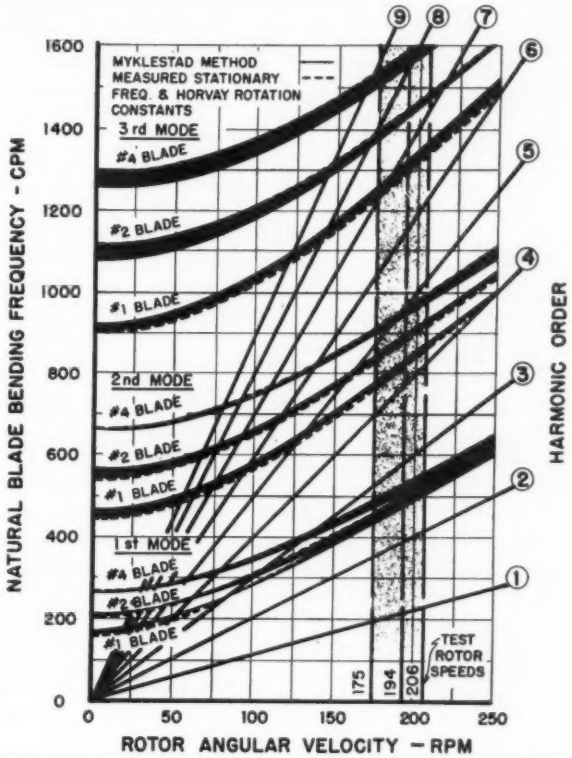

FIG. 5. Resonance diagram for flapwise bending of the fiberglass blades in the first, second, and third bending modes.

Next, as shown in the figure, a base line was drawn and the relative spanwise location of each trace was approximated. The direction of trace displacement was then indicated by an arrow, letting traces No. 2 and No. 8 remain undetermined. Knowing that all channels were sensed in the same direction, the blade deflection pattern immediately identified the source of the eighth-order component; the blade was unquestionably bending in the third bending mode.

Having thus revealed the existence of higher (third) mode resonant bending, steps were taken to determine whether its occurrence could be correlated with the measured frequency. Using available methods[10, 11] this was readily done, as shown in Fig. 5, and later discussed.

Natural frequency calculations were subsequently undertaken for the low- and high-stiffness blades for the cases of first-, second-, and third-mode bending. The results obtained predicted that at least one particular combination of blade stiffness, mode shape, and rotor speed would produce a resonant condition corresponding to each harmonic order between two and nine. Thus, before the flight program was undertaken, the resonant conditions and frequencies were predicted in detail. Results presented in later sections of this paper will show how well the predictions were checked by the measured data.

TABLE 2
Summary of Nonrotating Blade Characteristics

Blade Stiffness	Weight, Lbs.	Spanwise C.G. Station, In.	Moment of Inertia About Station 0, Slug-Ft.^{2}
Low (No. 1)	162.1	123.3	740
Medium (No. 2)	161.7	123.5	745
High (No. 4)	160.7	125.0	747

Blade Natural Frequency			
1st bending, c.p.m.	2nd bending, c.p.m.	3rd bending, c.p.m.	1st torsion, c.p.m.
155	440	895	1000
200	535	1110	1110
260	660	1290	1310

Determination of Blade Natural Bending Modes and Frequencies

As the first step in obtaining a correlation between the resonance conditions measured and those analytically predicted, the natural blade beam bending frequencies were determined. As previously mentioned, this was done for the first three bending modes for each blade stiffness, using both Horvay's[10] approximate coefficient method and the tabular solution outlined by Myklestad.[11]

Horvay Solution

In obtaining an approximate solution with Horvay's rotational coefficients, experimentally determined stationary blade natural bending frequencies were employed rather than those computed from Horvay's stationary coefficients. The experimentally obtained frequencies were used since it was believed that they would be more correct than those computed from the coefficients. This point, however, is not too important since the natural frequency values in the rotor operating speed range are insensitive to moderate variations of the stationary frequency values. This is particularly true of the first-mode frequencies and less so for the second- and third-mode frequencies.

Experimental Determination of Stationary Natural Frequencies

The stationary frequencies used in the Horvay solution were determined from a vibration survey of the blades. Substituting a welded steel fitting for the standard H-5 root sleeve and flapping link fittings, the blades were cantilevered from a structural backstop with the spanwise feathering axis horizontal and the chord plane vertical, leading edge down. The welded fitting also served to extend the blade so that the flapping hinge was located at its normal position at Station 0. The blade was hinged with a vertical pin at the attachment to the backstop so that it was permitted freedom in the flapping plane while being rigidly restrained in torsion and against movement in the blade lag plane. A variable-speed mechanical vibrator was attached to the blade tip at the quarter chord, and frequency sweeps were made to determine the frequencies of the first three natural bending modes and the node positions for each. The results obtained from the blade vibration survey are presented in Fig. 3 and Table 2.

Measured weight and balance characteristics of the blades are also summarized in Table 2. It will be noted that the maximum weight deviation of any instrumented blade from the average value for the three blades is less than 1 per cent and that the maximum spanwise center of gravity deviation from the average is also less than 1 per cent. More important, the variation of moment of inertia is even smaller. Since the measured node locations for all blades (Fig. 3) are in good agreement and since the type of blade construction precludes large local variations in blade weight, it may be concluded that the spanwise distribution of bending stiffness (EI) is similar in all blades, even though they differ widely in bending stiffness magnitude.

Myklestad Solution

The Myklestad method consists of a tabular procedure for determining the frequency at which the blade will vibrate subject to inertia forces while satisfying boundary conditions of zero deflection and zero moment at the hinged root and an assumed unit deflection at the blade tip. Trial frequencies other than a natural frequency produce a residual moment at the root hinge. By plotting the residual moment at the root hinge versus trial frequency, a curve is obtained from which the frequency at which the residual moment for each mode is zero can be accurately selected. This frequency is the natural bending frequency for the mode. The use of the preliminary natural frequency values determined from the Horvay solution made it possible to choose the trial values of frequency near the natural values, thereby reducing the number of trial computations required. This procedure is recommended as a timesaving step.

UNIVERSITY OF MICHIGAN LIBRARIES

Comparison of Blade Frequency Results

The relationships between blade natural bending frequency and rotor speed obtained by the Horvay and the Myklestad solutions may be compared by reference to Fig. 5, which includes curves showing the results obtained by each method. As indicated on the figure, results are given for the first, second, and third bending modes for each blade stiffness. It is seen that, in general, the agreement between methods is good. The maximum error between any two corresponding curves is less than 5 per cent for the stationary case and is less than 3 per cent in the range corresponding to rotor speeds at which flight tests were conducted (175–206 r.p.m.). It is also observed that the direction of error appears to be random.

Since the difference between results is less than the probable overall accuracy of either calculation, it will be assumed in subsequent discussions that the computed natural frequencies lie somewhere between the spread of the two results—that is, they lie within the shaded areas between curves.

Comparison of Blade Frequency Coefficients

Blade frequency coefficients comparable to those given by Horvay have been calculated for the Cornell Aeronautical Laboratory blades, using the natural frequencies obtained from the Myklestad solutions. The natural bending frequency may be approximated by the equation[12]

$$\omega_n^2 = \omega_{sn}^2 + b_n \Omega^2 \text{ cycles per sec.}$$

where

ω_n = rotating natural frequency in the nth mode (cycles per sec.)
ω_{sn} = stationary natural frequency in the nth mode (cycles per sec.)
b_n = a constant for the nth mode
Ω = rotational frequency (cycles per sec.)

Accordingly,

$$b_n = (\omega_n^2 - \omega_{sn}^2)/\Omega^2$$

The values of b_n obtained from the Myklestad results were calculated and compared with the values given by Horvay. Frequency values required in the calculations were read from Fig. 5, using the plotted stationary values and the value at 194 r.p.m. The results obtained are given in Table 3, together with the comparable values given by Horvay.

TABLE 3

Myklestad			
No. 1 blade	*No. 2 blade*	*No. 4 blade*	Horvay
$b_1 = 5.07$	$b_1 = 5.15$	$b_1 = 4.98$	$b_1 = 5.62$
$b_2 = 12.29$	$b_2 = 12.58$	$b_2 = 11.65$	$b_2 = 12.6$
$b_3 = 22.63$	$b_3 = 23.55$	$b_3 = 22.27$	$b_3 = 22.4$

Predicted Resonant Conditions

The conditions under which resonant bending may be anticipated can be predicted from a resonance diagram of the type commonly used in vibration work.[13] Fig. 5, which is typical of such diagrams, predicts resonant conditions for the three sets of Cornell Aeronautical Laboratory fiber-glass blades. Reference will subsequently be made to this diagram, with the objective of showing that the resonant conditions predicted were in fact consistently and accurately obtained.

Construction and interpretation of the resonance diagram are both simple. First, curves are constructed showing the variation of blade natural frequency, as ordinate, against rotational speed, as abscissa. Curves are plotted for each mode being investigated. Second, a family of straight lines is constructed, radiating from the origin, with slopes equal to the harmonic order numbers. The intersection of any natural frequency curve with any order line locates a resonant point. The order of the resonance is equal to the slope of the order line.

Study of the resonance diagram leads to several interesting and important generalizations, which will be used later to correlate the results obtained from the analysis of the measured resonance data:

(1) The frequencies at which resonance is predicted in any mode separate into groups. The groups do not overlap and are independent of blade stiffness. For example, it is seen that at all operating rotor speeds the first-mode frequencies fall between the second and third orders, the second-mode frequencies between the fourth and fifth orders, and the third-mode frequencies between the sixth and ninth orders.

(2) For even the exceptionally wide range of stiffness covered by the Cornell Aeronautical Laboratory blades, the variation of natural frequency with stiffness is small compared to the variation with mode.

(3) A decrease in blade stiffness in any mode will always tend to decrease the resonance order, the effect of the blade stiffness becoming increasingly important in the higher modes.

(4) An increase in rotor speed will, for all modes, always tend to decrease the resonance order, the effect of rotational speed becoming increasingly important in the higher modes.

Referring to Fig. 4, it is interesting to determine how well the eighth-order bending oscillation shown can be correlated with the resonance diagram. Entering the diagram at the ground run-up speed recorded (167 r.p.m.), it is found that eighth-order resonant bending of the medium-stiffness blade is exactly predicted. It is probable that the exact agreement obtained is somewhat a matter of chance, since it is improbable that the computed natural frequencies are sufficiently accurate to provide such precise correlation. Nevertheless, the check obtained is extremely convincing.

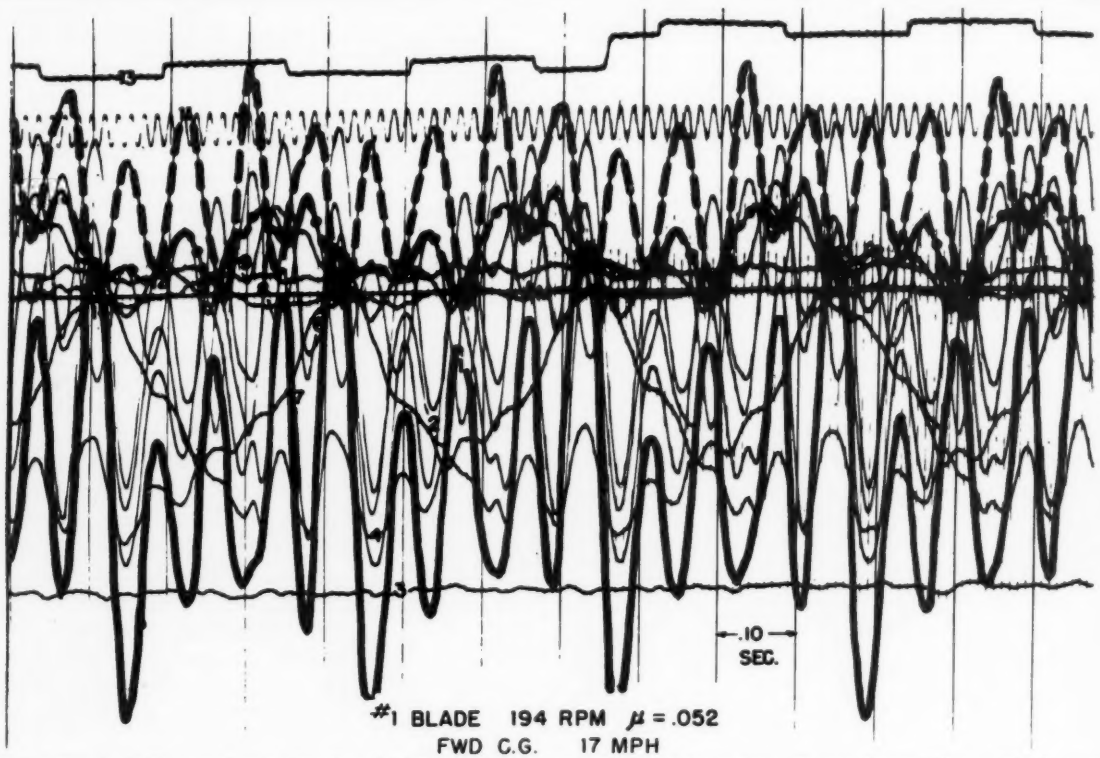

FIG. 6. Sample oscillogram showing bending of the low-stiffness blade in the transition region. Traces discussed in detail in the paper have been heavied up to aid in identification.

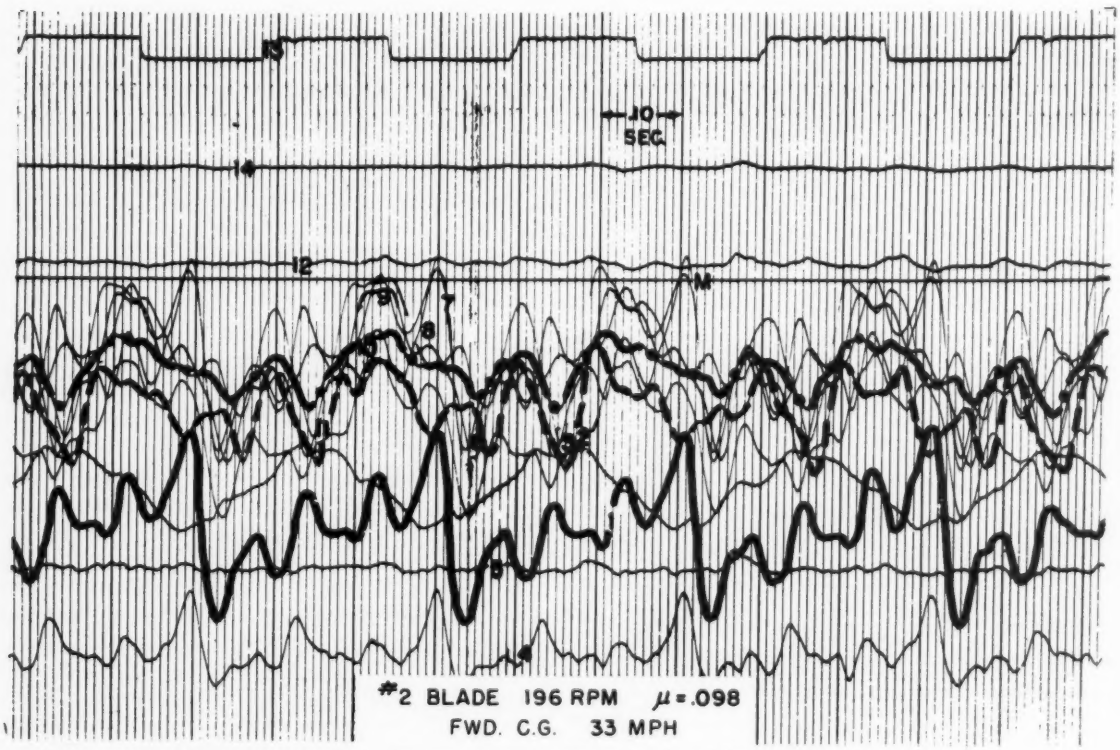

FIG. 7. Sample oscillogram, similar to Fig. 6, for the medium-stiffness blade.

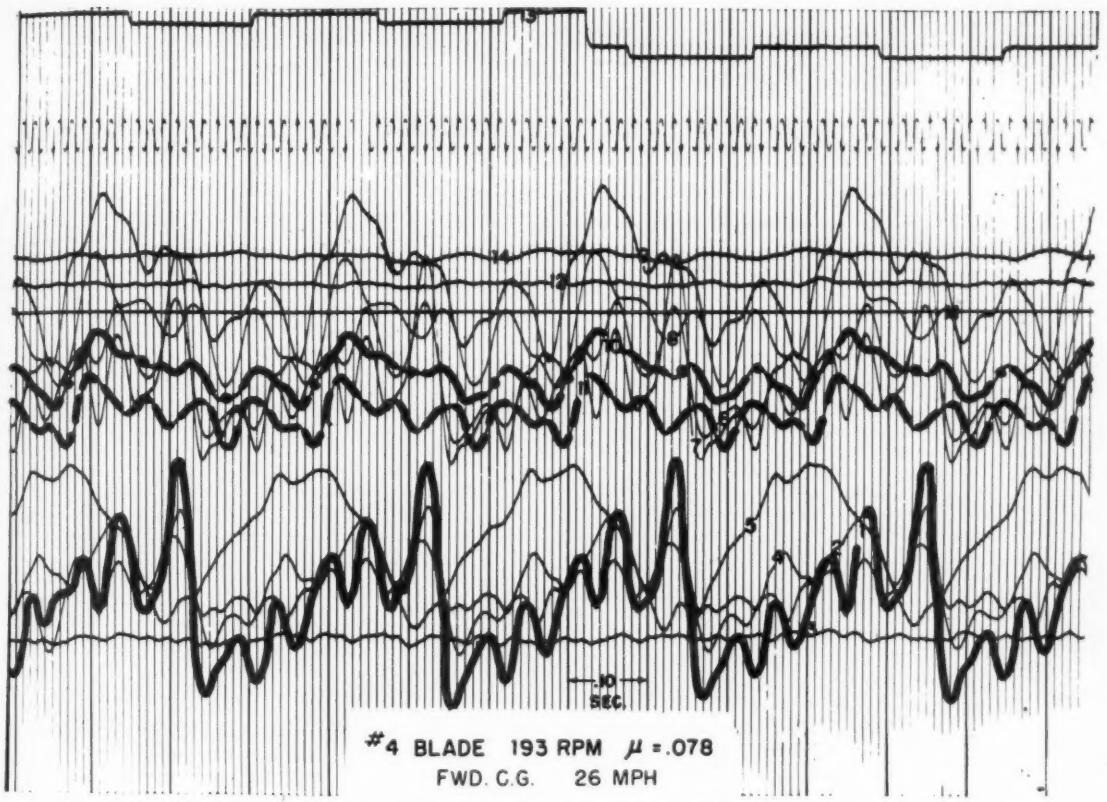

FIG. 8. Sample oscillogram, similar to Fig. 6, for the high-stiffness blade.

HARMONIC ANALYSIS OF BLADE BENDING MOMENTS

In the course of the variable-stiffness program, careful consideration was given to the problem of evolving methods of analyzing and evaluating data which would be convenient and accurate and, at the same time, provide an insight into the data not obtainable directly from the oscillograph records.

Since the rotor is a rotating mechanical device and the forces applied to the rotor in steady-state flight are periodic, the possibility of reducing the measured data to the form of a Fourier expansion appeared advantageous. Reduced in this manner, the data could be readily presented in tabular form. More important, however, was the fact that the reduced and tabulated harmonic data could be directly interpreted in terms of such important parameters as number of blades, aerodynamic loads, blade bending modes, and similar physically definable quantities. For example, the number of blades determines the phase relation between the loads applied to the helicopter; aerodynamic loads are calculated in the form of summations of harmonically varying quantities having frequencies that are multiples of the rotor speed, and, as revealed in this paper, certain important bending characteristics of rotor blades can be readily explained in terms of harmonic bending components. For these reasons, all rotor data were reduced to the form of Fourier coefficients and phase angles.

Data-Analysis Procedures

The amplitude coefficients and phase angles were obtained from harmonic analysis of selected cycles of each blade beam bending trace for each test point. Each trace was reduced to the first ten terms of its Fourier expansion, using a Dent-Draper Rolling Sphere Analyzer, of the Corradi type. The harmonic analyzer performs integrations that measure the sine and cosine components of the Fourier series expansion of the curve being analyzed. From the components, the resultant amplitudes and phase angles are computed. The expansion was carried through ten terms since preliminary analyses of shakedown data had shown that bending effects in the second and third bending modes would produce harmonic components, respectively, between the fourth and fifth and sixth and ninth orders.

Conversion of the harmonic coefficients to units of blade beam bending moment was accomplished by applying a channel sensitivity factor, determined from dead-weight calibrations recorded before and after each flight. These values were further adjusted for sensitivity and drift variations, which in some cases occurred during the flight, by comparing calibration

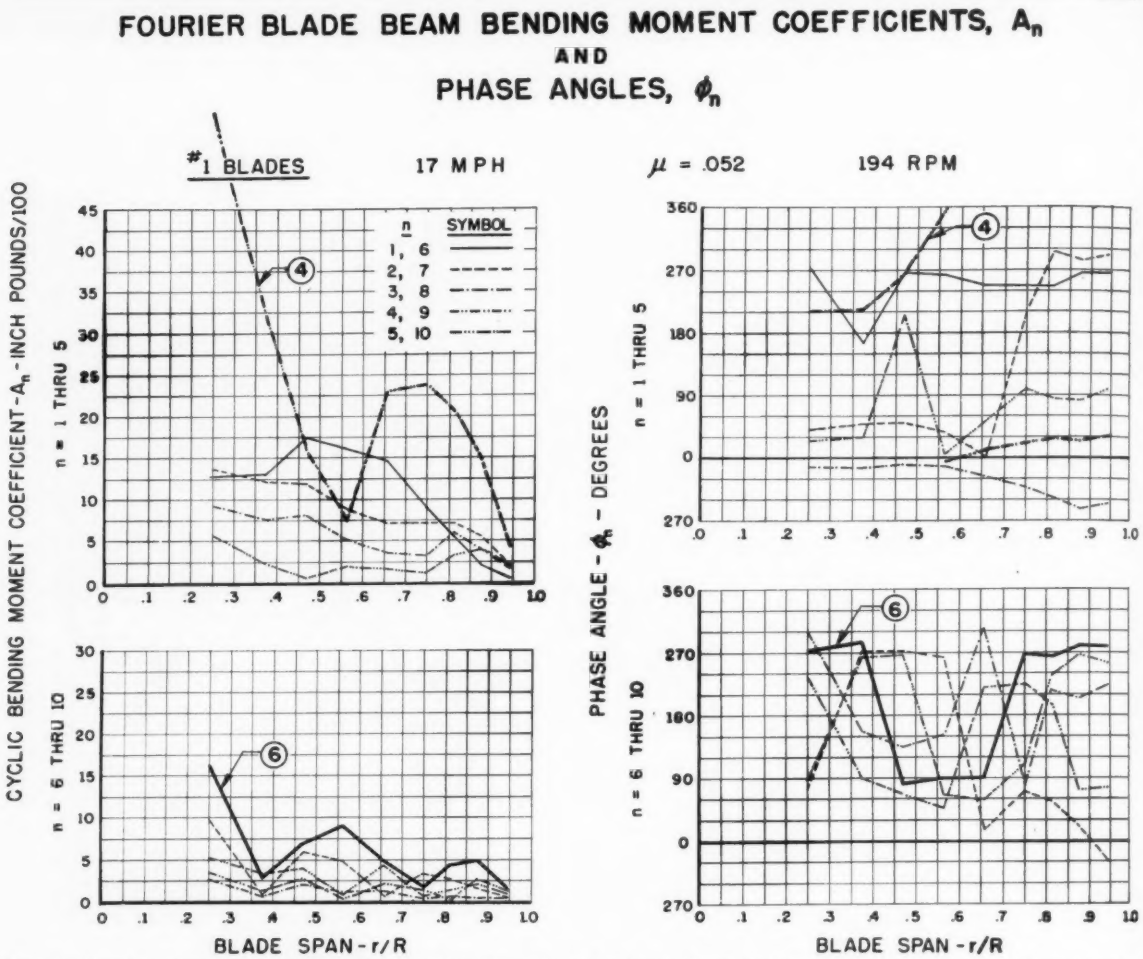

FIG. 9. Fourier reduction of transition bending data (Fig. 6) for the low-stiffness blades, showing predominance of fourth-order bending in the second mode and sixth-order bending in the third mode.

injects taken at intervals during the ground calibration with injects taken between the data record runs. Calibration injects were obtained for each trace by sequentially switching the data strain-gage bridge for each channel to a calibrated signal of fixed value.

Sample oscillograms showing sections of the flight-test records obtained for three test points are reproduced in Figs. 6, 7, and 8. The nine channels recording beam bending data may be identified from Fig. 3. Three traces on each record have been "heavied up" so that they may be followed. The three traces (Station 72 shown as a dash line, Station 135 as a dot-dash line, and Station 234 as a solid line) were chosen to bring out certain facts concerning the bending characteristics of the blades. The manner in which they do so can be visualized by reference to the mode shape diagrams (Fig. 3). The diagrams show that Station 72 is located so as to exhibit bending content in all three modes. Station 135 is located near a point of inflection in the second mode and should therefore show little second-mode content but large first- and third-mode content. Station 234 should show little first-mode content because of its outboard position and substantial second- and third-mode content because of its position between the second- and third-mode inflection points.

The sample records, all taken in the transition range, exhibit clearly the predominant higher mode bending components. Visual inspection of the records for the high- and medium-stiffness blades (No. 4 and No. 2) reveals, respectively, large fifth- and fourth-order components. Similar inspection of the record for the low-stiffness (No. 1) blade reveals an even larger fourth-order component. It is seen that the harmonic order and spanwise distribution of the higher frequency components agree with the concept of higher mode bending. Specifically, it is seen that the second-mode bending component, which appears as a fifth-order component with the No. 4 blades, appears as a fourth-order component with the No. 2 blades. Further, with the No. 1 blades, which provide a further decrease in stiffness, the

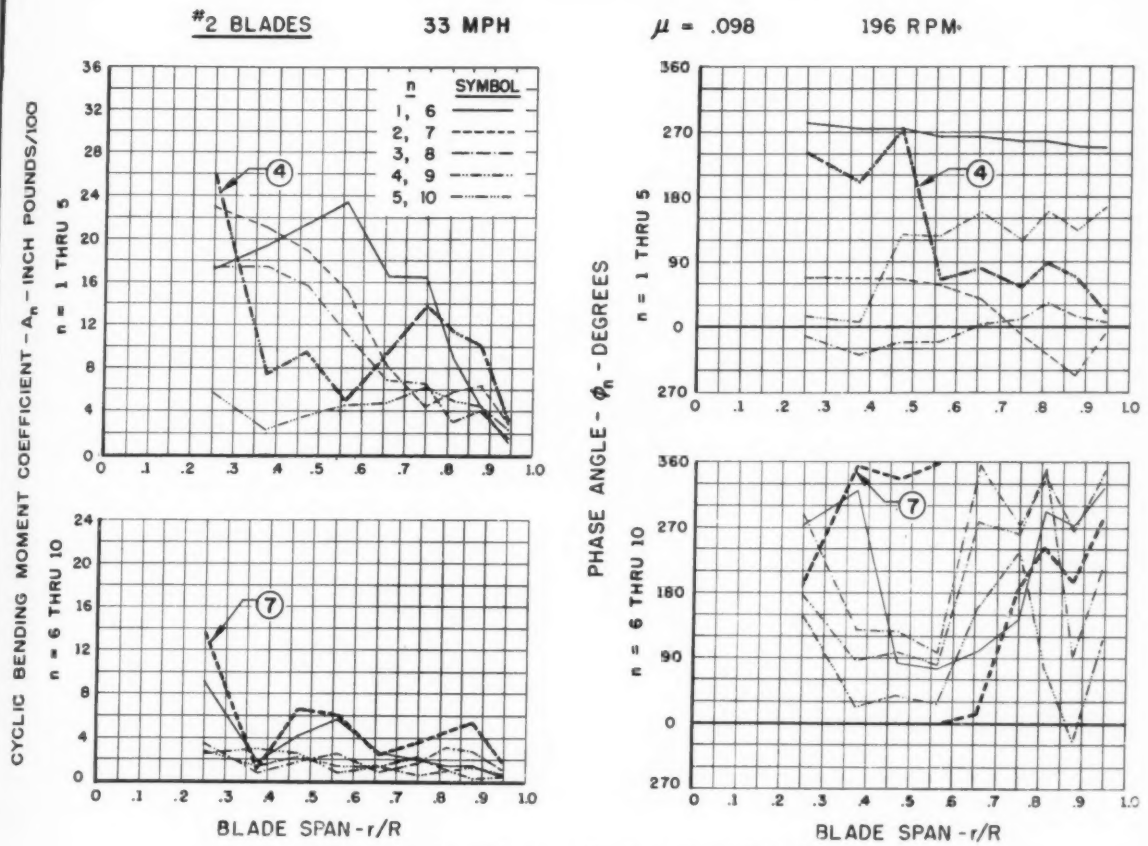

FIG. 10. Fourier reduction, analogous to Fig. 9, for the medium-stiffness blades.

fourth-order component becomes increasingly large, apparently denoting a closer approach to resonance. By comparing the phase of the bending traces for Station 72 and Station 234, it is seen that the 180-deg. phase difference required between bending measured at blade stations on opposite sides of the second-mode inflection point exists.

While the particular records shown clearly exhibit the characteristics, oscillatory amplitudes, and harmonic relationships associated with resonance, it is to be noted that they show extreme conditions and that the records for many other test conditions reveal, to the eye, little or none of the pronounced resonance visible here. On the other hand, as will be shown later, the harmonic analysis of almost every record does disclose substantial higher harmonic content.

Fourier Moment and Phase-Angle Plots

The harmonic data derived from each of the preceding sample oscillograms are shown in Figs. 9, 10, and 11. The ten amplitude coefficients and phase angles for each of the nine bending data channels are plotted against blade span. For clarity, harmonics one through five are shown on one plot, and harmonics six through ten on another. It is interesting to examine the harmonic plots and to determine how they may be identified with the oscillograms and interpreted in terms of the resonance diagram.

From a resonance point of view, the harmonic data for the high-stiffness (No. 4) blade reveal several important facts. It is seen (Fig. 11) that the predominant harmonics are the first, third, fifth, and eighth. The strength of the first harmonic is explained on the basis of the usually strong first-harmonic air loading. The fifth and eighth harmonics, which cannot be explained on the basis of known air loads, are shown by the resonance diagram, Fig. 5, to fall on predicted resonant points. Their large response seems thus explained. It is also seen from the resonance diagram that the large amplitude of the third harmonic appears to be explainable on the basis of resonant amplification, since the high-stiffness blade approaches resonance with the

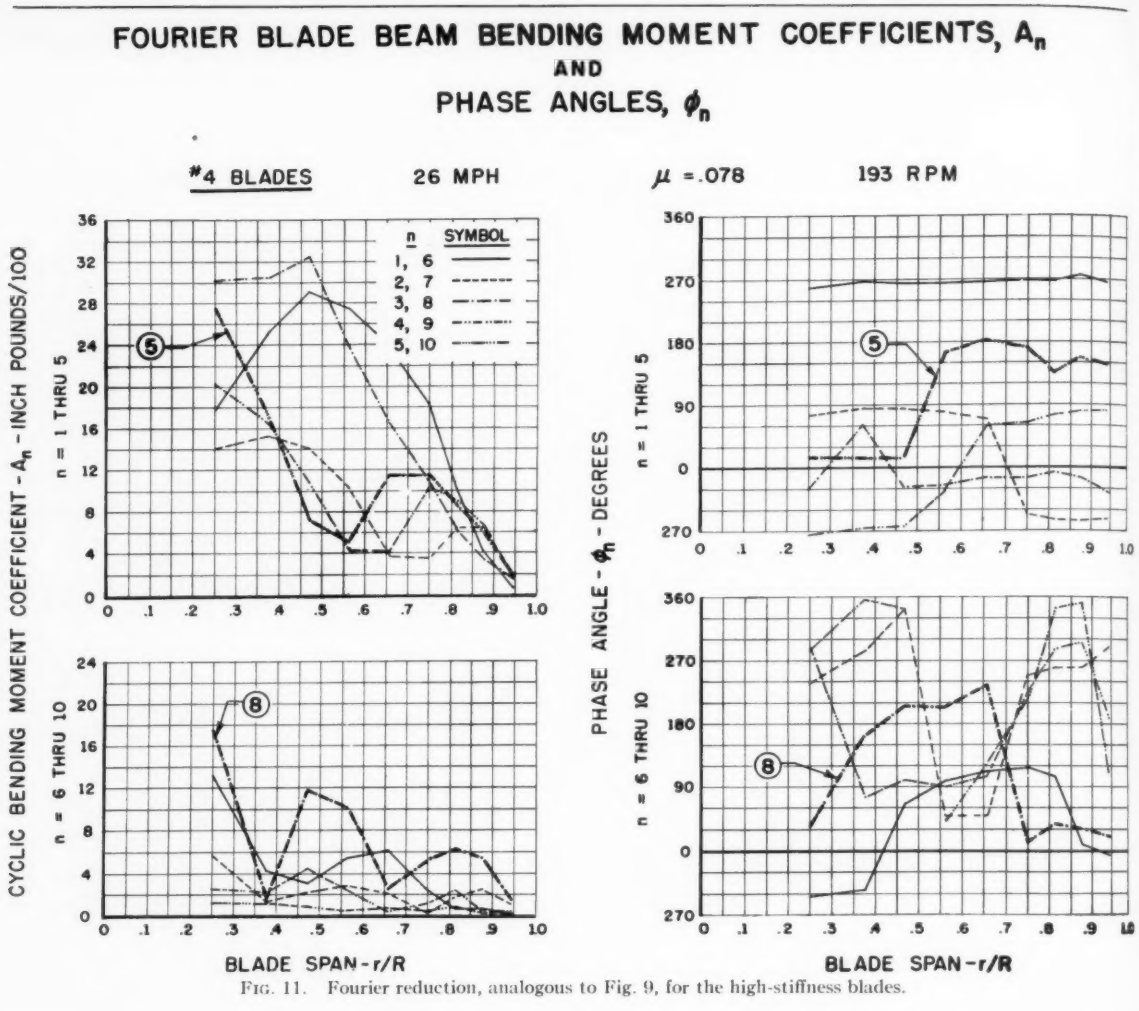

FIG. 11. Fourier reduction, analogous to Fig. 9, for the high-stiffness blades.

third-harmonic loads. Referring to the oscillograph traces, Fig. 8, it is seen that the large fifth-order component is readily identified in the trace (No. 1) for Station 234.

The spanwise distribution of the harmonic amplitudes and phase angles is next examined in order to determine whether they are consistent with the blade bending mode shapes. Referring to the third-harmonic amplitude and phase plots of Fig. 11, it is seen that the spanwise distribution of moment approximates the first bending mode shape in that it decreases smoothly from a peak value at mid-span to zero at the blade tip and that the peak amplitudes are all reached at approximately the same azimuth position. Referring to the fifth-order amplitude, it is found that the spanwise distribution decreases from a peak value at 0.25 span, to nearly zero at 0.56 span, then builds up to a second peak at 0.75 span, and drops off to zero at the tip. From the phase-angle plot, it is seen that the peak values for the inner half of the blade reach a maximum at approximately the same azimuth position (15°) and that the peak values on the outer half of the blade are all reached a half cycle later (180°). It is seen, therefore, that the second-mode amplitude distribution is consistent with the second-mode bending shape and that second-mode bending is verified. Similarly, by noting the two cusps in the eighth-order bending amplitude distribution and the double phase shift from approximately 30 to 210 to 30 deg., large bending in the third mode may be verified.

Study of the harmonic data for the medium- and low-stiffness blades will similarly establish the existence of large bending contributions in the second and third modes and show that the occurrence and order of the resonances measured are consistently predicted by the resonance diagram.

It is particularly interesting to note the extremely large fourth-order component apparent in the sample record, Fig. 6, for the low-stiffness blades. As seen from the record and shown in the harmonic plots, Fig. 9, the contribution of higher mode bending (fourth and sixth orders) is larger than the sum of all other har-

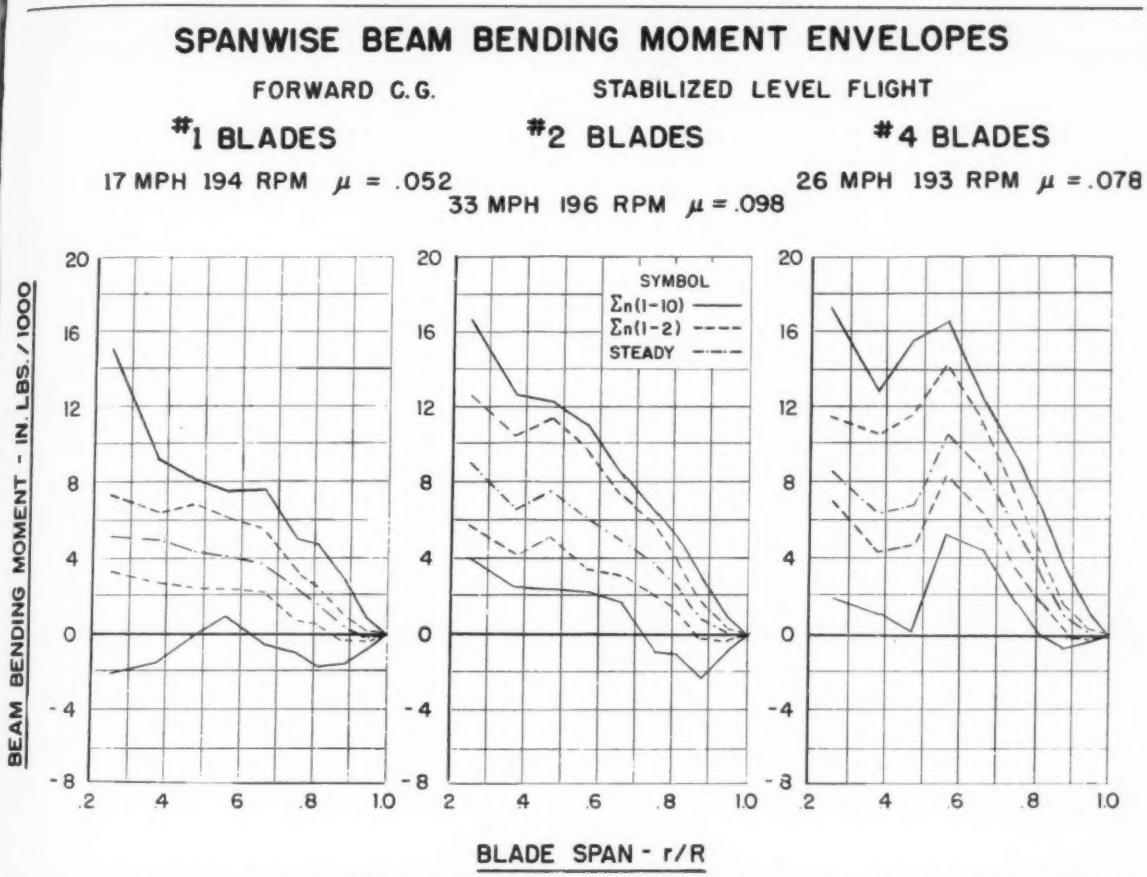

FIG. 12. Envelopes showing spanwise distribution of maximum and minimum beam bending moments measured during one rotor revolution. The envelopes correspond to the oscillograms shown in Figs. 6, 7, and 8.

monics. Although no substantiating evidence is given here, it is noted that the peak bending moments recorded for this test point are, over most of the blade, more than one and one-half times as great as the design moment envelope obtained from the maximum moments computed for any and all flight conditions.

ADVANCE RATIO EFFECTS

The data obtained from the test program show that the critical blade bending conditions were not experiences in high-speed flight but rather in the transition region. Further, it was generally found that a substantial, and sometimes predominant, portion of the total bending moment consisted of third- and higher order components.

This section of the paper presents results that substantiate the foregoing statements. Two types of data plots are reviewed. The first type (Fig. 12) consists of bending moment envelopes for the three transition conditions shown by the sample oscillograph records, plotted against blade span. The second (Figs. 13, 14, and 15) consists of bending moment envelopes plotted against advance ratio. In the latter plots, data for the nine blade stations are condensed on a single figure, thus providing a convenient means of studying the spanwise variation of the advance ratio effect.

Current methods of blade stress analysis assume that the total moment applied to the blades consists of a combination of only steady, first-harmonic and second-harmonic bending moment components. In order to provide data that might be used to study the reliability of these methods, one set of envelopes including only the first- and second-harmonic components of the measured data was prepared. This may be compared with the theoretically predicted harmonic components for the corresponding flight conditions. A second set of envelopes has also been determined for the sum of ten harmonics. The two envelopes, plotted on the same figure, provide a convenient method of showing the measured contribution of the higher harmonic terms and of disclosing how large they become in certain conditions.

By calling attention to these results, it is hoped that the structural importance of the resonance phenomenon throughout the speed range will be established and that attention will be called to the need for better design criteria.

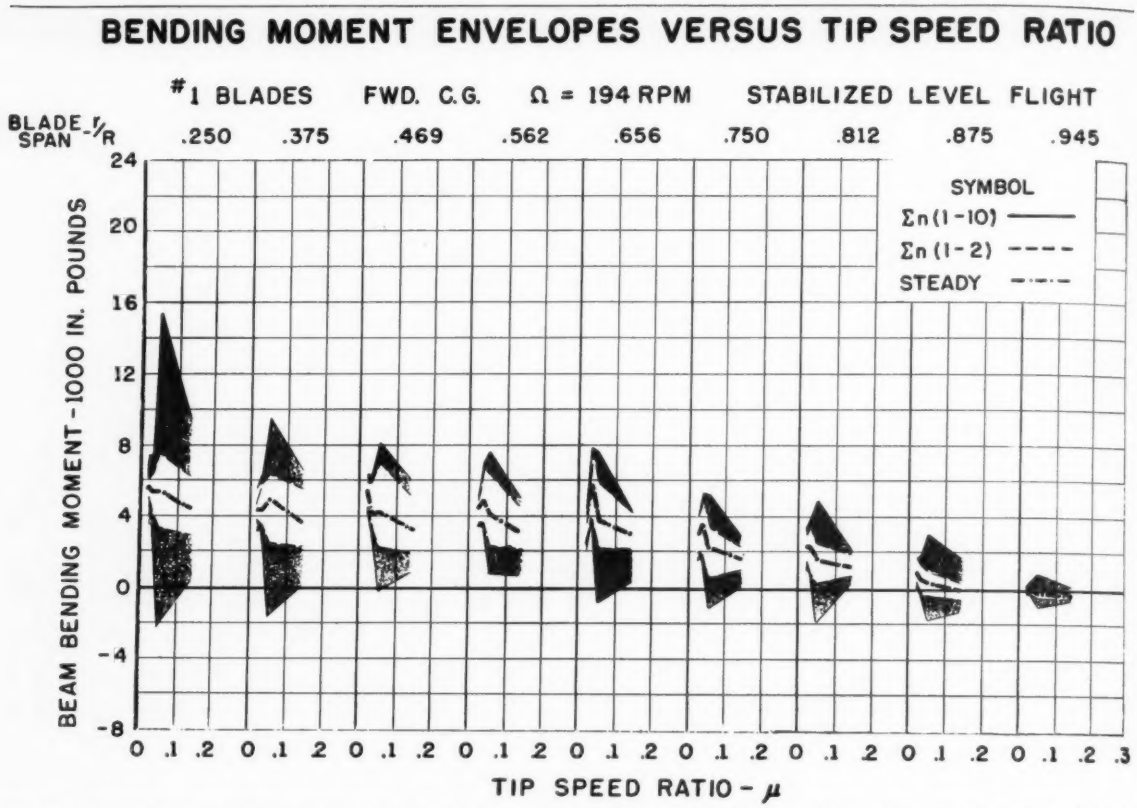
BENDING MOMENT ENVELOPES VERSUS TIP SPEED RATIO
#1 BLADES FWD. C.G. Ω = 194 RPM STABILIZED LEVEL FLIGHT
BLADE SPAN - r/R
.250 .375 .469 .562 .656 .750 .812 .875 .945
SYMBOL
Σn (1-10)
Σn (1-2)
STEADY
BEAM BENDING MOMENT - 1000 IN. POUNDS
24 20 16 12 8 4 0 -4 -8
0 .1 .2 0 .1 .2 0 .1 .2 0 .1 .2 0 .1 .2 0 .1 .2 0 .1 .2 0 .1 .2 0 .1 .2 .3
TIP SPEED RATIO - μ

FIG. 13. Spanwise beam bending moment distributions for the low-stiffness blade, showing the contributions of the sum of third- and higher order bending terms, as a function of advance ratio.

Bending Envelope Synthesis

The moment envelopes presented are plotted from data computed with a "synthesizer" developed for use in the program. The synthesizer is an electromechanical computer that provides the sum of either the first two or first ten harmonics, derived from the measured data, as a function of blade azimuth. The data set into the machine consist of the Fourier harmonic coefficients and phase angles for each trace.

While normally the envelopes might be determined from peak moment values measured directly from the oscillograph records, this could not be done in the present case without sacrificing accuracy because filters inserted in the data channel circuits for the purpose of removing high-frequency hash also produced substantial signal attenuation. With the filters used the response at frequencies as low as 3 cycles per sec. (rotor speed) fell off to 90 per cent, and, at frequencies corresponding to the important fourth and fifth harmonics (12 to 15 cycles per sec.), the response fell to 75 per cent. The filter attenuation problem was one of the reasons for employing the synthesizer; another was that use of the synthesizer also provided a convenient means of obtaining the harmonic sums used to construct the moment envelopes for the sum of the first and second harmonics

The steady bending moment distribution about which the loading oscillates throughout the azimuth cycle is also shown in the maximum-minimum envelope plots. The steady moments were computed from the test results, using the synthesizer. Adding the maximum and minimum cyclic moments to the steady moment determined for each blade station gave the maximum and minimum blade beam bending moment envelopes shown in the figures.

Description of the Harmonic Synthesizer

Basically, the harmonic synthesizer is a device in which the coefficients, phase angles, and harmonic relationships of a Fourier series may be inserted using a combination of electrical and mechanical means and the values of the sum of the series determined as a function of angular displacement. The machine consists principally, of ten pairs of selsyn units, ten potentiometers, and ten sets of gears having the exact ratios of the integers one through ten. The proper phase relationships of the harmonic inputs are obtained by setting the rotor positions of ten of the selsyns. The rotors of the remaining ten selsyns are geared to a common shaft by the ten sets of gears and are, therefore, caused to rotate through angles proportional to their harmonic order. The potentiometers provide a means of regulat-

UNIVERSITY OF MICHIGAN LIBRARIES

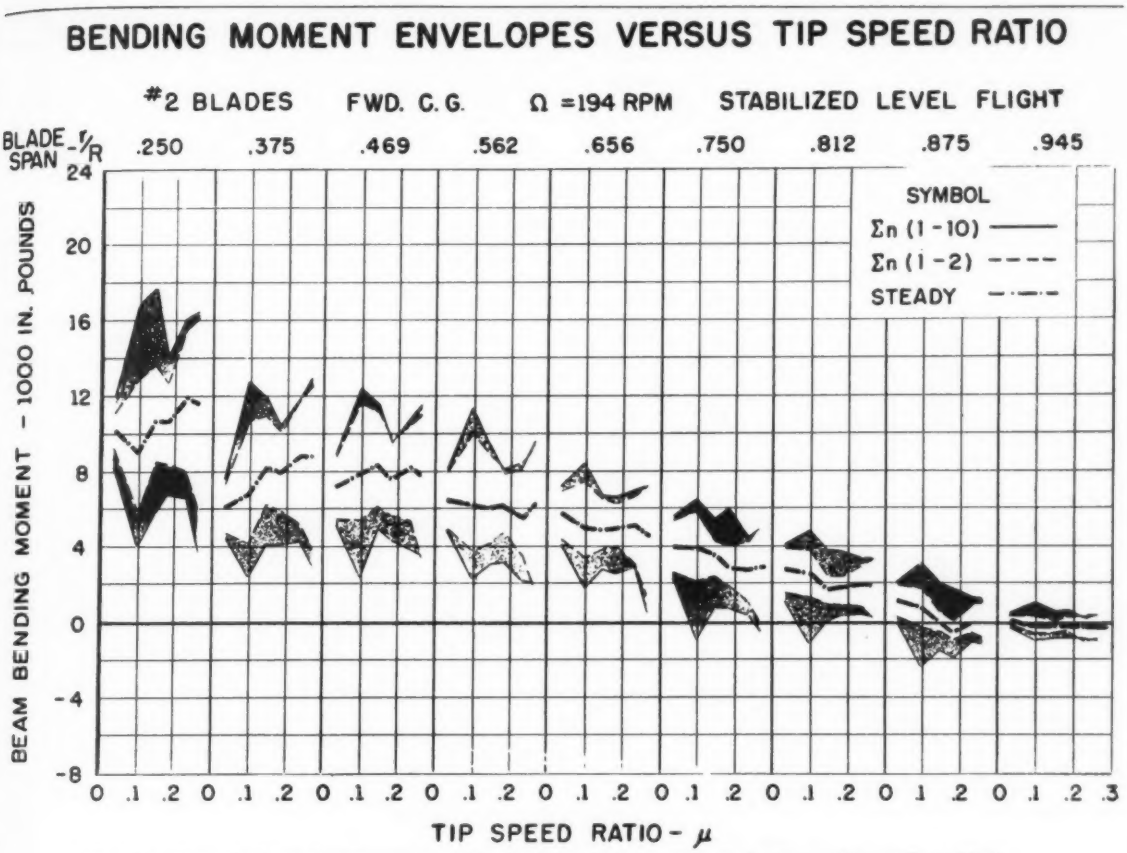
BENDING MOMENT ENVELOPES VERSUS TIP SPEED RATIO
#2 BLADES FWD. C.G. Ω =194 RPM STABILIZED LEVEL FLIGHT
BLADE SPAN - r/R
.250 .375 .469 .562 .656 .750 .812 .875 .945
SYMBOL
Σn (1 - 10)
Σn (1 - 2)
STEADY
BEAM BENDING MOMENT - 1000 IN. POUNDS
24 20 16 12 8 4 0 -4 -8
0 .1 .2 0 .1 .2 0 .1 .2 0 .1 .2 0 .1 .2 0 .1 .2 0 .1 .2 0 .1 .2 0 .1 .2 .3
TIP SPEED RATIO - μ

FIG. 14. Spanwise beam bending moment distributions, similar to Fig. 13, for the medium-stiffness blade.

ing the voltage—proportional to harmonic amplitude—applied to each pair of selsyns. By adding the voltage outputs of the ten pair of selsyns in series, as a function of angular position of the common geared shaft, the vector sum of the ten inputs is determined. When applied to the present problem, this is equivalent to providing the sum of the harmonic bending moment components as a function of blade azimuth. The sum of the first and second harmonics was obtained by a switching arrangement that added the voltage output of only the two proper sets of selsyns.

It was stated previously that the test data showed that the critical blade bending conditions were measured in the transition region. Also, it was shown by one example for each blade that a large part of the total moment consisted of the higher harmonic terms and that these terms originated from resonant bending. Since data are only given for one test point with each blade, the only comparisons that can be made directly are those concerned with blade stiffness effects. From the envelope data given in this section, the role played by advance ratio effects may be evaluated separately from the resonance effects.

In Fig. 12, envelopes synthesized from the harmonic data given in the harmonic plots (Figs. 9–11) are plotted against blade span. Each envelope shows the maximum and minimum moment experienced at each blade station during one rotor revolution. One set of curves, for the sum of ten harmonics, shows the total moment at the station. The second set of curves shows the sum of the first and second harmonics. The steady moment curve shown applies to the envelope for the sum of ten terms. Although the envelopes for the sum of two terms are constructed by plotting the maximum and minimum moments relative to the steady value, it should be recognized that the steady value does not have the physical significance with respect to two terms which it has with respect to ten terms. It is also noted that the steady value is not the average of the maximum and minimum values. This follows from the fact that the phase differences between the various harmonics cause the maximums and minimums to occur at different azimuth positions and to sum to different total values. In certain cases, it is found that the effects of the phase differences will even cause the sum of only the first and second harmonics to be greater than the sum of the ten harmonics.

The important bending moment contribution of the higher harmonics in the transition region is apparent in Fig. 12. It is seen that, in addition to accounting for a

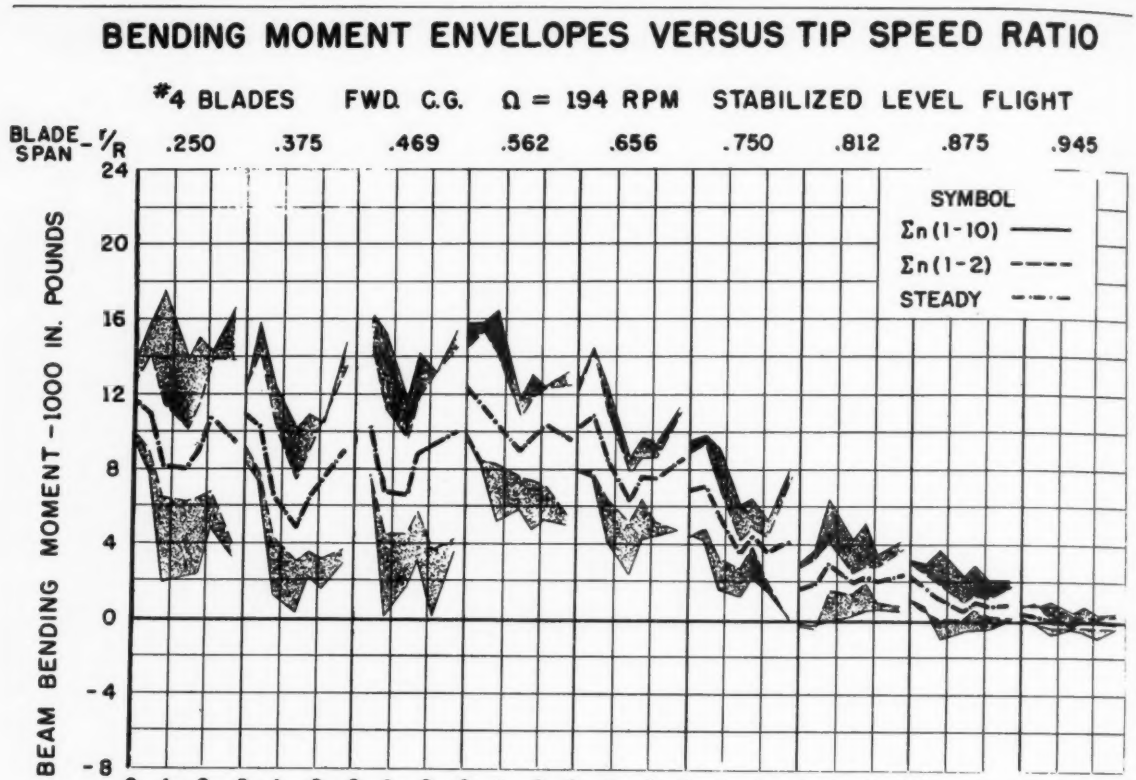
BENDING MOMENT ENVELOPES VERSUS TIP SPEED RATIO
#4 BLADES FWD. C.G. Ω = 194 RPM STABILIZED LEVEL FLIGHT
BLADE SPAN - r/R .250 .375 .469 .562 .656 .750 .812 .875 .945
BEAM BENDING MOMENT - 1000 IN. POUNDS
24
20
16
12
8
4
0
-4
-8
SYMBOL
Σn(1-10)
Σn(1-2)
STEADY
0 .1 .2 0 .1 .2 0 .1 .2 0 .1 .2 0 .1 .2 0 .1 .2 0 .1 .2 0 .1 .2 .3
TIP SPEED RATIO - μ

FIG. 15. Spanwise beam bending moment distributions, similar to Fig. 13, for the high-stiffness blade.

large part of the total moment on all blades. the higher harmonics may produce substantial negative bending. This is found to be particularly so with the low-stiffness blades, the negative bending resulting largely from the predominant fourth-order second-mode bending component.

The effect of advance ratio can be shown by plotting the maximum-minimum moment against advance ratio, as has been done in Figs. 13, 14, and 15. Although curves are shown for only the normal rotor speed, forward center of gravity, level flight conditions, results for other conditions of operation show that these curves are typical. In the form shown, two main effects are observed. First, at all advance ratios and all blade stations, the higher harmonic contributions are important. In most cases, and particularly with the medium-stiffness blades, the envelopes peak twice, first in transition and later at high speed. In all cases the transition peak is greatest. Over the inboard half of the blade the contributions of the higher harmonics are large in the transition conditions. In high-speed flight, the higher harmonic contributions continuously decrease although the peak values are again increasing. The small differences between the sum of two and sum of ten terms obtained over the inboard half of the blade in high-speed flight do not result from absence of the higher harmonics but from the fact that the predominant harmonics are out of phase and cancel one another. Over the outboard half of the blade, the contribution of the higher harmonics at intermediate speeds tends to be larger than inboard. This can again be accounted for primarily by a phase effect, since the large second-mode contribution has shifted phase by approximately 180°. Also, in this region of the blade, the second- and third-mode contributions are in phase. At high speeds, the differences between the harmonic content curves become extremely small, and, in some cases, the curves cross. This results from the fact that near the blade tip the second- and third-mode components are out of phase and that the amplitudes of the third-mode components become larger than those for the second mode.

RESONANCE CORRELATION

In the case of the three transition test points previously analyzed, it was shown that the occurrence and order of the higher harmonic bending components agreed well with those predicted by the resonance diagram. It is shown in this section that equally good agreement can be obtained by treating the 97 test

UNIVERSITY OF MICHIGAN LIBRARIES

points recorded in the test program (Table 1) as a whole. This is done by determining the average value of each harmonic for all test points in which the rotor speed and blade stiffness are the same. In this way the effects of advance ratio, center of gravity position, and flight condition (level flight, climb, autorotation) are averaged out of the results. As an example, 19 test conditions were averaged to obtain the average value of all data for the medium-stiffness blades operating at 194 r.p.m. Referring to Table 1, the 19 points are seen to consist of seven points with forward and five with aft helicopter center of gravity positions and seven points in climb.

The averaged values obtained for three blade stations have been plotted in Figs. 16, 17, and 18. Each figure applies to a particular blade spanwise station. Nine bar graphs are plotted on each figure, one for each combination of three blade stiffnesses and three test rotor speeds. The three blade stations for which average harmonic plots are given (Stations 72, 135, and 234) were selected because they provide a maximum amount of information with which to correlate the predicted and measured resonances, as discussed elsewhere in this paper.

It is recalled that in an earlier discussion it was pointed out that the harmonic orders predicted for resonance in each mode fell into nonoverlapping groups, as follows: first mode—second or third order; second mode—fourth or fifth order; and third mode—sixth, seventh, eighth, or ninth order. Keeping these groupings in mind, the predominant harmonics in each group can be selected from each bar graph and tabulated with the results shown in Table 4.

Inspection of the table clearly reveals that rotor resonant bending is a phenomenon common to all conditions of helicopter flight and that the measured data agree consistently and accurately with the results that were predicted. It is noted that each and every trend predicted from inspection of the resonance diagram (Fig. 5) is systematically and accurately verified. That is, the orders of the harmonics decrease with decrease of blade stiffness and increase of rotor speed and that the harmonics associated with the third mode shift order more often than those associated with the first or second mode. Finally, it is seen that the location of Station 135 near a point of second-mode inflection is reflected in the absence of significant fourth- or fifth-order harmonic content and that the predominant second- and third-mode components anticipated at Station 234 are obtained.

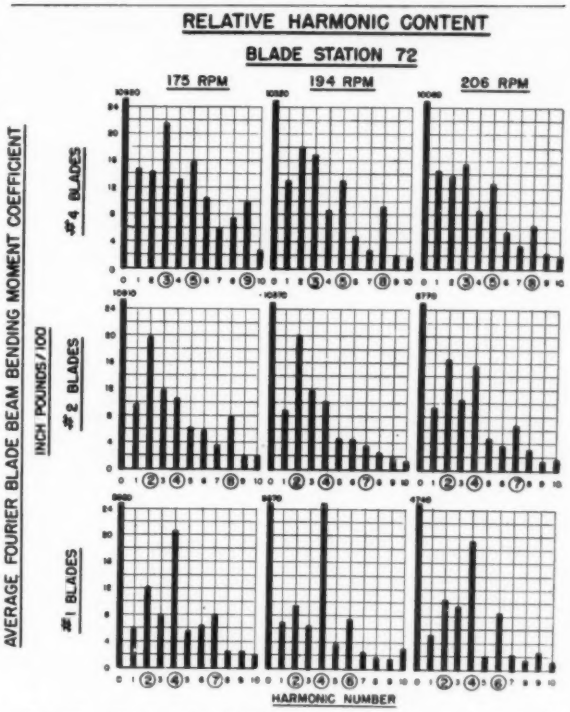

FIG. 16. Bar graphs showing the bending moment harmonic content at Station 72, averaged from representative data for all régimes of helicopter flight.

CONCLUDING REMARKS

It is obvious from the results presented that the blade resonance problem is of primary concern to rotor-blade designers and that it should be carefully considered in the design and flight evaluation phases of rotor development programs.

While the good correlation obtained between predicted and measured results indicates that it should be possible to predict resonant conditions during the design stage, unfortunately, it is found that little can be done to avoid coming close to one or another resonant point. It appears that the best that can be done, at least until the nature of the resonance is understood, is to make provision in the design so that the natural frequencies do not coincide with multiples of the normal rotor operating speed and, more important, to provide

TABLE 4
Tabulation of Predominant Harmonic Orders

	Station 72			Station 135			Station 234		
	175	194	206	175	194	206	175	194	206
No. 4	3, 5, 9	3, 5, 8	3, 5, 8	3, —, 9	3, —, 8	3, —, 8	—, 4, 9	—, 4, 8	—, 4, 8
No. 2	2, 4, 8	2, 4, 7	2, 4, 7	2, —, 8	2, —, 7	2, —, 7	—, 4, 8	—, 4, 7	—, 4, 7
No. 1	2, 4, 7	2, 4, 6	2, 4, 6	2, —, 7	2, —, 6	2, —, 6	—, 4, 7	—, 4, 6	—, 4, 6

Dashes indicate that the content is relatively small.

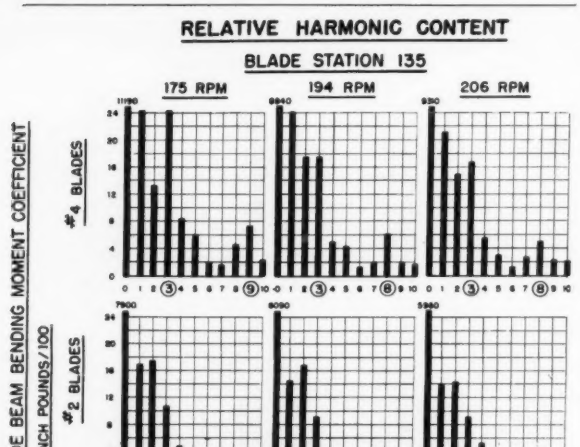

FIG. 17. Bar graphs showing harmonic bending moment content at Station 135, averaged from the same test points as Fig. 16.

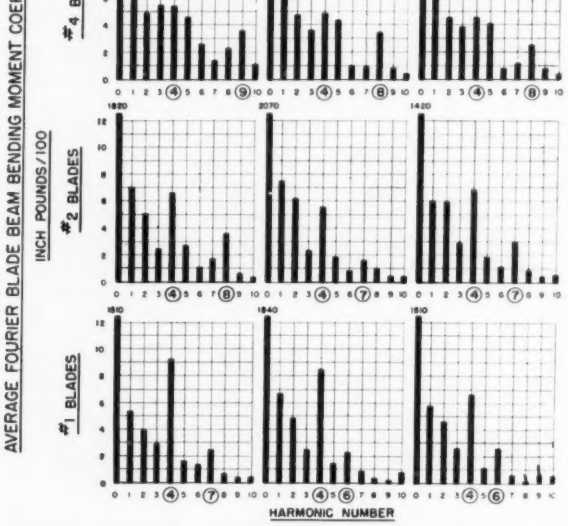

FIG. 18. Bar graphs showing beamwise bending moment content at Station 234, averaged from the same test points as Fig. 16.

sufficient structural strength, over and above that required to carry the normally computed steady, first- and second-harmonic loads, so that the blade can safely operate subject to higher order loads and resultant moments. A tentative but detailed method for estimating higher order loadings, based on the results of the variable-stiffness program, has been outlined by Daughaday and Kline.[14]

Anticipating the probability of higher order bending stresses, it is important that the blade designer recognize the critical role that resonant conditions may play in determining the fatigue life of blades. Since the blade resonant frequencies are harmonic multiples of the rotor speed, it is important to anticipate that the number of load cycles applied to the blade will be proportional to the product of total rotor revolutions and the excited harmonic orders and that the peak stresses and vibratory moment amplitudes will be larger than predicted by current theory.

Finally, the results call attention to the necessity of providing sufficient data stations, when conducting blade strain surveys, so that information will be obtained at all critical blade locations. Equally important, it is necessary that the stations be judiciously chosen so that they do not fall at points of inflection and thereby fail to detect important higher mode contributions.

It is trusted that this paper will direct the attention of those concerned to the rotor-blade higher mode bending phenomenon and that it discloses the most important manifestations of the problem. It is recognized that no answers are provided to many of the questions raised. Such answers are not yet available. It is hoped, however, that this paper will occasion sufficient interest and concern so that the problem will receive the attention it merits and that the needed answers will be forthcoming soon.

ACKNOWLEDGMENT

This paper has been extracted from reports prepared to summarize the Variable-Stiffness Blade investigation carried out at Cornell Aeronautical Laboratory, Inc., under sponsorship of the Air Research and Development Command, Wright Air Development Center. The sponsoring agency's permission to publish this paper is gratefully acknowledged.

The work reported was the responsibility of the Aero-Mechanics Department of Cornell Aeronautical Laboratory. While, in his capacity as project supervisor, it fell to the lot of the author to prepare this paper, it is obvious that credit for the successful completion of a project of the scope reported belongs to many participants. Particular credit is given to the important contributions of the Cornell Aeronautical Laboratory Materials and Flight Research Departments in the performance, respectively, of the rotor-blade fabrication and the instrumentation and flight-test phases of the work.

The contributions of W.A.D.C. Propeller Laboratory personnel, who conducted whirl tower and preliminary strain-gage calibrations on prototypes of the fiber-glass test blades, and those of Capt. Paul A. Simmons, Rotary Wing Branch, who, acting as project officer, gave the project continuing support, are also acknowledged. Individual recognition is given to the contributions of Hans Weichsel, Jr., who acted as flight engineer and project pilot; to Mr. James Kline, who supervised much of the analysis and data reduction included in the program and assisted in the preparation of this paper; and, finally, to A. F. Donovan, Head of the Cornell Aeronautical Laboratory Aero-Mechanics Department, who directly contributed to the program results, guided the project through difficulties, and is now carrying forward certain investigations suggested by the program.

References

[1] Johnson, W. C., and Mayne, R., *Effect of Second-Harmonic Flapping on the Stresses of a Hinged Rotor Blade*, Goodyear Aircraft Corporation, Report No. R-107-4, Part 3, May 2, 1946.

[2] Winson, J., *Motion of an Unarticulated Helicopter Blade*, Journal of the Aeronautical Sciences, Vol. 14, No. 9, p. 520, September, 1947.

[3] Flax, A. H., and Goland, L., *Dynamic Effects in Rotor Blade Bending*, Journal of the Aeronautical Sciences, Vol. 18, No. 12, p. 813, December, 1951.

[4] Arnold, L., and Goland, L., *Helicopter Dynamic Stability and Control Studies*, Cornell Aeronautical Laboratory Report No. BB-437-S-1, Part No. 1, September 29, 1950.

[5] Hirsch, H., Kline, J., and Mertens, R., *A Preliminary Design Study of Main Rotor Blades for a Variable Stiffness Flight Test Program*, Cornell Aeronautical Laboratory Report No. BB-427-S-2, Sept. 16, 1946.

[6] Hirsch, H., and Mertens, R., *Fabrication Procedure for Fiber Glass Main Rotor Blade for the H-5 Helicopter*, Cornell Aeronautical Laboratory Report No. BB-427-S-4, January 17, 1947.

[7] Hirsch, H., *Design and Construction of the Cornell Fiber Glass Helicopter Main Rotor Blades*, Fifth Annual Forum of the American Helicopter Society, May 12, 1949.

[8] Kidd, E. A., Hirsch, H., Guske, E., and Weichsel, H., *H-5 Variable Stiffness Blade Program Instrumentation and Shakedown Flight Phase Summary Report*, Cornell Aeronautical Laboratory Report No. BB-427-S-9, April 15, 1951.

[9] Weichsel, H., *Helicopter Flight Test Technique, Variable Blade Stiffness Program*, Fifth Annual Forum of the American Helicopter Society, May 12, 1949.

[10] Horvay, G., *Chordwise and Beamwise Bending Frequencies of Hinged Rotor Blades*, Journal of the Aeronautical Sciences, Vol. 15, No. 8, p. 497, August, 1948.

[11] Myklestad, H. O., *Vibration Analysis*, 1st Ed., p. 210; McGraw-Hill Book Company, Inc., New York, 1944.

[12] Den Hartog, J. P., *Mechanical Vibrations*, 3rd Ed., p. 328; McGraw-Hill Book Company, Inc., 1947.

[13] *Ibid*, p. 332.

[14] Daughaday, H., and Kline, J., *H-5 Variable Stiffness Blade Program, A Tentative Empirical Criterion for the Design of Rotor Blades for Higher Mode Resonances*, Cornell Aeronautical Laboratory draft of A.F. Technical Report No. 6329, Part 6, 1952.

Fourth Plasticity Symposium

Brown University, Providence, R.I. September 1–3, 1953

This symposium will cover three principal topics: (1) stress-strain relations (perfectly plastic, workhardening, viscoelastic, and viscoplastic materials); (2) distribution of stress and strain in bodies exhibiting inelastic properties (static and dynamic problems, infinitesimal and finite deformations); and (3) structural analysis and design in the inelastic range (limit analysis, static and dynamic loading, shakedown, inelastic buckling). Papers will be presented by American and foreign experts.

Certain sessions will be sponsored by Brown University in cooperation with the American Society of Civil Engineers' Engineering Mechanics Division. The remaining sessions will be sponsored jointly by Brown University and the Office of Naval Research.

For further information, please contact: Prof. Harry J. Weiss, Graduate Division of Applied Mathematics, Brown University, Providence 12, R.I.

Readers' Forum

BRIEF REPORTS of investigations in the aeronautical sciences and discussions of papers published in the JOURNAL are presented in this special department. Publication will be completed as soon as possible after receipt of the material. The Editorial Committee does not hold itself responsible for the opinions expressed by the correspondents. Contributions should not exceed 800 words in length.

Further Note on the Use of the Neutral Point as a Stability Parameter

S. J. Deitchman
Aerodynamicist, Bell Aircraft Corporation, Buffalo, N.Y.
March 11, 1953

IN A RECENT NOTE in the Reader's Forum of the JOURNAL, Baron[1] pointed out that the neutral-point location is not necessarily an indication of longitudinal static stability if the control effectiveness changes with angle of attack due to downwash effects. In showing this, it was assumed that the control effectiveness is independent of control deflection. For the type of aircraft discussed, however (canard, supersonic missile), this assumption is excessively restrictive.

The nonlinearity of the downwash at the aft wing derives from the behavior of the vortex sheet behind the forward wing. If the forward wing span is large with respect to the aft wing and the tail length is small with respect to the forward wing span, the trailing vortex sheet can be considered essentially flat and the downwash variation with normal force linear. However, with the forward wing of approximately the same span and a relatively large distance ahead of the aft wing, the trailing vortex sheet is partially or completely rolled up at the aft wing location. The vortex cores from the tips will either cross the aft wing or pass close to its tips. Therefore, the distribution of downwash will be nonuniform, and, furthermore, it will vary with C_N since the degree of rolling up of the trailing vortex sheet at the aft wing location depends on C_N.[2, 3] Since deflection of the elevator on the forward wing represents a change of C_N of that wing, the downwash effect on control effectiveness may be expected to depend on control deflection as well as α. It should be noted that the use of the trailing vortex concept for supersonic downwash has been justified by various authors.[2, 4]

Following the pattern and using the notation of reference 1, but using the NACA convention for writing derivatives, the stability equation may be derived in a more general way. Let the variation of pitching moment and normal force coefficients with control-surface deflection at constant α be of the general nature shown in Fig. 1.

Then C_{m_0} and C_{N_0} will be increments of moment and lift coefficient due to the variation of C_{m_δ} and C_{N_δ} with δ, and the equation for the pitching moment about a point b in terms of the conditions at point a is

$$(C_m)_b = (C_m)_a - C_N X^* + [(C_{m_\delta})_a - (C_{N_\delta})X^*]\delta + f_m(\delta) - f_L(\delta)X^* \quad (1)$$

where $C_{m_0} = f_m(\delta)$ and $C_{N_0} = f_L(\delta)$ are defined in Fig. 1.

From this, differentiating with respect to α, determining $(C_{m_\alpha})_a$ in terms of conditions at the neutral point, N, letting $X_{a,b}{}^*$ go to zero at the center of gravity and $X_N{}^*$ be the distance from the c.g. to the neutral point (positive forward), and dividing through by C_{N_α}, the stability equation becomes, for trimmed flight,

$$(C_{m_{C_N}})_{c.g.,T} = X_N{}^*\left[1 + \delta_N \frac{d}{dC_N}(C_{N_\delta})\right] + (\delta_T - \delta_N)\frac{d}{dC_N}(C_{m_\delta})_{c.g.} + \frac{d}{dC_N}[F(\delta_T) - F(\delta_N)] \quad (2)$$

where

$$F(\delta_T) = f_m(\delta_T) - f_L(\delta_T)X^* = f_m(\delta_T)$$
$$F(\delta_N) = f_m(\delta_N) - f_L(\delta_N)X_N{}^*$$

For the missile to be stable, the right-hand side of Eq. (2) must be negative. Whether or not this will be the case depends on the magnitudes and directions of the variations of C_{m_δ} and C_{N_δ}, as well as the relative locations of the c.g. and neutral point.

For a specific example, if the pitching-moment characteristics of the missile are as shown in Fig. 2, then the following relations will probably hold for trimmed flight:

$$\delta_N \leq 0$$
$$(\delta_T - \delta_N) \gtrless 0 \quad \text{if} \quad X_N{}^* \lesseqgtr 0$$
$$\frac{d}{dC_N}(C_{N_\delta}) < 0; \quad \frac{d}{dC_N}(C_{m_\delta})_{c.g.} < 0$$

from which

$$\left.\begin{aligned}(\delta_T - \delta_N)\frac{d}{dC_N}(C_{m_\delta})_{c.g.} &\lesseqgtr 0 \\ \frac{d}{dC_N}[F(\delta_T) - F(\delta_N)] &\gtrless 0\end{aligned}\right\} \text{ if } \quad X_N{}^* \lesseqgtr 0$$

and

$$\delta_N(d/dC_N)(C_{N_\delta}) \geq 0$$

where the upper signs or lower signs of $\gtrless$ in paired conditions are to be used simultaneously.

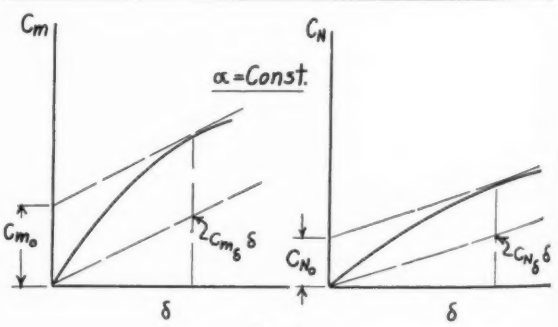

FIG. 1.

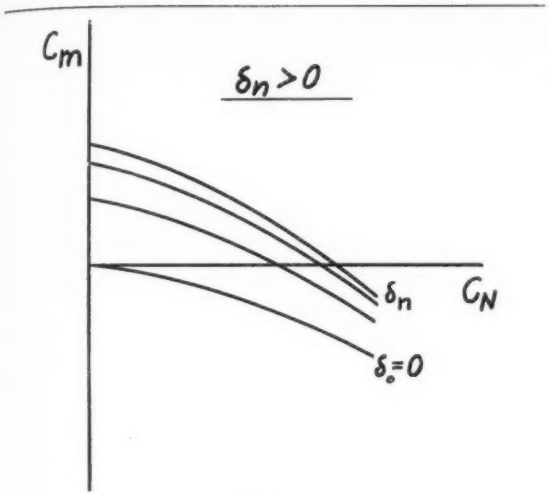

FIG. 2.

Applying these inequalities to the right-hand side of Eq. (2) shows that, if certain conditions of the magnitude and direction of pitching moment variations with δ are satisfied, it is possible to have a stable missile with the c.g. aft of the neutral point or an unstable one with the c.g. forward of the neutral point. Thus the concept of static margin as an all-inclusive measure of stability breaks down.

The chief significance of this result is the difficulty it introduces into making preliminary estimations of missile stability. If experimental data are available, the degree of stability is still indicated by the slope $(C_{m_{C_N}})_{\text{c.g.}, T}$, but the instantaneous aerodynamic center location of the complete configuration is no longer given by this slope.

REFERENCES

[1] Baron, Judson, R., *On the Use of the Neutral Point as a Stability Parameter*, Reader's Forum, Journal of the Aeronautical Sciences, Vol. 20, No. 2, pp. 145, 146, February, 1953.

[2] Sacks, A. H., and Spreiter, J. R., *The Rolling Up of the Trailing Vortex Sheet and Its Effect on the Downwash Behind Wings*, Journal of the Aeronautical Sciences, Vol. 18, No. 1, January 1951.

[3] Durand, W. F., Ed., *Aerodynamic Theory*, Vol. II, E VI, pp. 320 ff.; Julius Springer, Berlin, 1934.

[4] Mirels, H., and Haefeli, R. C., *Line-Vortex Theory for Calculation of Supersonic Downwash*, NACA TN 1925, August, 1949.

A Note on the Weight of the Blades in an Axial-Flow Compressor

John Mitchell Stephenson
Research Associate, Division of Engineering, Brown University, Providence, R.I.
March 19, 1953

THE GENERAL PROBLEM of designing an axial-flow compressor for the minimum weight is complex and can usually be discussed only for particular numerical cases. But by making some simplifying assumptions—especially that all the stages in a compressor are aerodynamically similar—it is possible in a few minutes to calculate the weight of all the blades in terms of the weight of the blades in the first stage.

A chart can then be drawn up to show the weight penalty incurred if manufacture is simplified by using the same blades (suitably shortened) for more than one row. The only properties of the compressor that must be known are the number of stages and their pressure ratio and efficiency. It is assumed that the maximum allowable bending stress is independent of the centrifugal stress. If this is not admitted and only the maximum *total* stress is fixed, the weight penalties for grouping are slightly larger than those given here.

The weight W of a row of blades is proportional to their number B, their root section area A, their height h, and a factor f, which takes account of the taper. Thus

$$W \propto BAhf$$

But, approximately, $A \propto ct$, where c and t are the chord and maximum thickness of the root section and where the product Bc is proportional only to the radius and solidity of the root section. Therefore, if we assume that Bc, f, are the same for all stages,

$$W \propto th \tag{1}$$

It was shown in reference (1) that the maximum bending stress in a blade can be written approximately as σ, where

$$\sigma t^2/h = (\cos\zeta + \beta \sin\zeta)\cdot QC_p\Delta T/2uBck \tag{2}$$

where $(\cos\zeta + \beta\sin\zeta)/k$ is a number of the order 10, depending of the geometry of the blade; Q is the mass flow; $C_p\Delta T$ is the work done in the stage; and u is the mean tangential blade speed. The right-hand side of Eq. (2) depends on the aerodynamic design of the stage, and we shall assume it to be the same for all of the stages in a compressor. Hence, if the stress is also constant,

$$t^2 \propto h$$

and substituting in Eq. (1)

$$W \propto h^{3/2} \tag{3}$$

Let us also assume that the Mach Number is the same at the entrance to each stage. Then $Q\sqrt{T}/PA$ is constant through the compressor, where T and P are the temperature and pressure (either total or static values will do) and A is the flow area (annulus area $\times$ cosine of the flow angle). Therefore, if the mean radius is constant,

$$h \propto A \propto \sqrt{T}/P$$

and, from Eq. (3)

$$W \propto T^{3/4}\cdot P^{-3/2} \tag{4}$$

Now assume that the polytropic efficiency η is constant through the compressor and that the entry temperature and pressure are fixed. Therefore,

$$P \propto T^{\gamma\eta/(\gamma-1)}$$

and, if $\gamma = {}^7/_5$,

$$P \propto T^{3.5\eta}$$

Any appropriate value for η can be used; a convenient value is $\eta = {}^6/_7$, which gives

$$T \propto P^{1/3}$$

Hence, Eq. (4) becomes

$$W \propto P^{-5/4} \tag{5}$$

If the pressure ratio of each stage is the same, the pressure at entry to the nth stage is

$$P_n \propto r^{n-1}$$

and the weight of the nth stage is, from Eq. (5),

$$W_n \propto P_n^{-5/4}$$

or

$$W_n \propto \exp\,[-(5/4)\,(n-1)\cdot\log_e r] \tag{6}$$

So the stages can be made progressively lighter.

The total weight of all the blades is clearly least if those in each successive row are thinner as well as shorter, so as to keep the stress constant at the maximum allowable value. But it is frequently cheaper to manufacture successive rows of rotors (or stators) by cropping the tips of the rotor (or stator) blades in the previous stage, thus keeping the root dimensions constant for two or more stages. In this case, the stresses in the second, third, etc., rows in each group are less than the maximum allowable value, and there is a weight penalty.

If there are $g_1, g_2, g_3, \ldots$, blade rows in each group and N rows altogether, the total weight is Ω times the weight of the first stage row, where

$$\Omega = \sum_1^n W_n/W_1$$

or, writing $[(5/4)\log_e r]$ as q in Eq. (6),

$$\Omega = g_1 + g_2 \exp(-qg_1) + g_3 \exp[-q(g_1 + g_2)] \ldots \quad (7)$$

The extreme conditions are when the stages are all the same and $\Omega = N$, and when they are all different, so that

$$\Omega = [1 - \exp(-qN)]/[1 - \exp(-q)]$$

Between these limits, the condition that Ω is a minimum for a given number of groups is

$$\frac{\partial\Omega}{\partial g_1} = \frac{\partial\Omega}{\partial g_2} = \frac{\partial\Omega}{\partial g_3} = \ldots = 0$$

or

$$\left.\begin{aligned} 1 - qg_2 &= \exp(qg_1) \\ 1 - qg_3 &= \exp(qg_2) \\ 1 - qg_4 &= \exp(qg_3) \end{aligned}\right\} \quad (8)$$

etc.

The application of Eqs. (7) and (8) can best be illustrated by a numerical example. Suppose $q = 1/4$; then using Eqs. (8) we can plot, as in Fig. (1), curves of g_2, $(g_1 + g_2)$, g_3, $(g_1 + g_2 + g_3)$, g_4, $(g_1 + g_2 + g_3 + g_4)$, etc. Then if we have a compressor with, say, eleven stages, we draw vertical lines intersecting the lines of $(g_1 + g_2)$, $(g_1 + g_2 + g_3)$, and $(g_1 + g_2 + g_3 + g_4)$, at the ordinate eleven. The appropriate values of g_1, g_2, g_3, and g_4 are read off the intersections to the nearest whole number. Therefore Table 1 can be compiled, the corresponding values of Ω being calculated from Eq. (7). The weight penalty incurred by grouping is seen at a glance in the last row. The relative weight of distributions other than those given in the table can easily be calculated from Eq. (7). The case of two groups, for instance, is shown in Fig. 2.

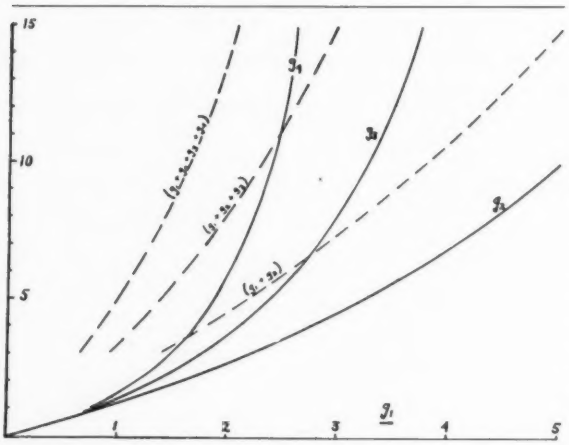

FIG. 1.

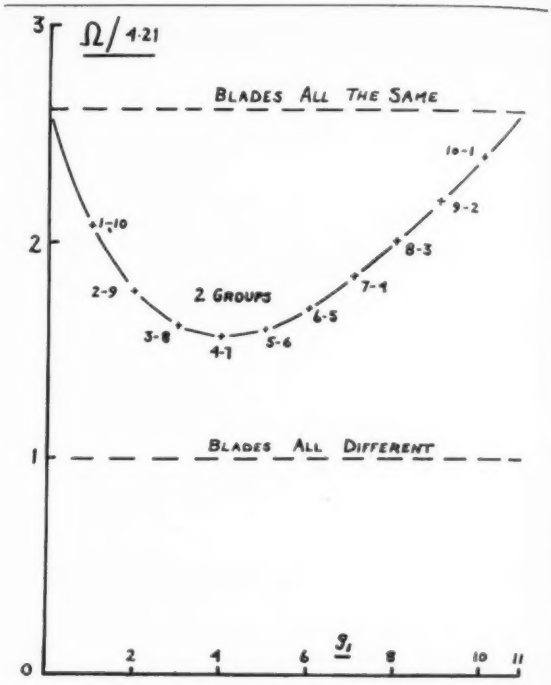

FIG. 2.

TABLE 1

Number of Groups	1	2	3	4	11
Distribution	11	4-7	3-3-5	2-2-3-4	...
Ω	11	6.58	5.53	5.02	4.21
$\Omega/4.21$	2.61	1.56	1.31	1.19	1.00

In practice, the apparent advantage of using many groups may not always be realized because of a lower limit to the blade thickness imposed by the process of manufacture.

REFERENCE

[1] Stephenson, J. M., *The Gas Bending Stress on a Blade in an Axial-Flow Compressor*, Readers' Forum, Journal of the Aeronautical Sciences, Vol. 20, No. 5, p. 357, May, 1953.

A Method for Differentiation of Experimental Data

William M. Kauffman and Marvin Shinbrot
Ames Aeronautical Laboratory, NACA, Moffett Field, Calif.
February 13, 1953

IN ANALYZING THE MEASURED TRANSIENT RESPONSE of aircraft to disturbances, it is often desired to evaluate time derivatives of the measured quantities. Among other uses, these quantities can be employed in various forms of the derivative method for determining the aircraft stability parameters.[1] However, there has been a tendency to avoid this procedure because of the difficulty in evaluating the time derivatives with sufficient accuracy.

Recently, one of the authors was faced with this problem while attempting to develop methods for analyzing the measured

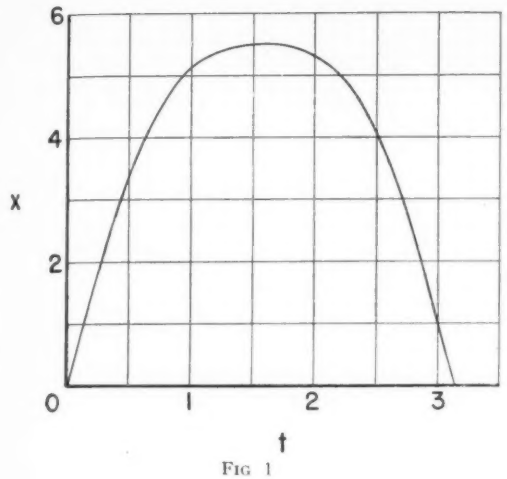

FIG. 1

transient response of nonlinear systems. The usual graphical and numerical differentiation methods were checked first by applying them to analytically expressed functions having certain characteristics of available or expected test data. These methods did not consistently yield even the first derivative to the desired accuracy when the basic data were rounded off to simulate recorded data typical of dynamic flight tests. This difficulty led to the development of the following differentiation method, which has been applied successfully to several problems at hand.

Basically, it is a differencing method refined by a curve-fairing procedure. Given a curve $x = f(t)$, consider any point $t = T$. Calculate

$$\Delta x_1 = x(T + \Delta t) - x(T)$$
$$\Delta x_2 = x(T + 2\Delta t) - x(T)$$
$$\Delta x_{-1} = x(T - \Delta t) - x(T)$$
$$\Delta x_{-2} = x(T - 2\Delta t) - x(T)$$

where Δt is a convenient small interval. Next find the quantities $\Delta x_k/k\Delta t$ ($k = 1, 2, -1, -2$), which are all approximations, of the familiar general form $\Delta x/\Delta t$, to the derivative dx/dt at $t = T$. Then plot $\Delta x_k/k\Delta t$ as a function of k, and fair a curve through the four points. The ordinate of this curve at $k = 0$ is a measure of dx/dt, since

$$\lim_{k \to 0} \frac{x(T + k\Delta t) - x(T)}{k\Delta t} = \lim_{\Delta t \to 0} \frac{x(T + \Delta t) - x(T)}{\Delta t} \equiv dx/dt$$

More than four points can, of course, be used but generally have not been found necessary; two points yield the often crude chord-line approximation.

This procedure is illustrated in the following test problem. The function

$$x = 6 \sin t + 0.5 \sin 3t$$

($0 \leq t \leq \pi$) was selected as a troublesome one having a term ($0.5 \sin 3t$) with a relatively small effect on x but successively larger effects on dx/dt and d^2x/dt^2. This function is plotted in Fig. 1. The only data furnished a computer who evaluated dx/dt and d^2x/dt^2 by the above method were the values of x at Δt intervals of 0.2. These x values were rounded off to 0, 3, 5, or 8 in the second decimal place, corresponding to recorded data with a readability of about 0.5 per cent of the maximum value.

Plots of $\Delta x_k/k\Delta t$ for a few values of T are given in Fig. 2. The resulting values of dx/dt ($\Delta x/k\Delta t$ at $k = 0$) are plotted as circles in Fig. 3. The entire procedure was then repeated with these dx/dt results to obtain the d^2x/dt^2 points plotted as triangles in Fig. 3. Curves representing the true values of dx/dt and d^2x/dt^2, determined analytically from the given equation for x, are shown for comparison. The accuracy of the proposed method appears particularly noteworthy in view of the complicated shapes of the

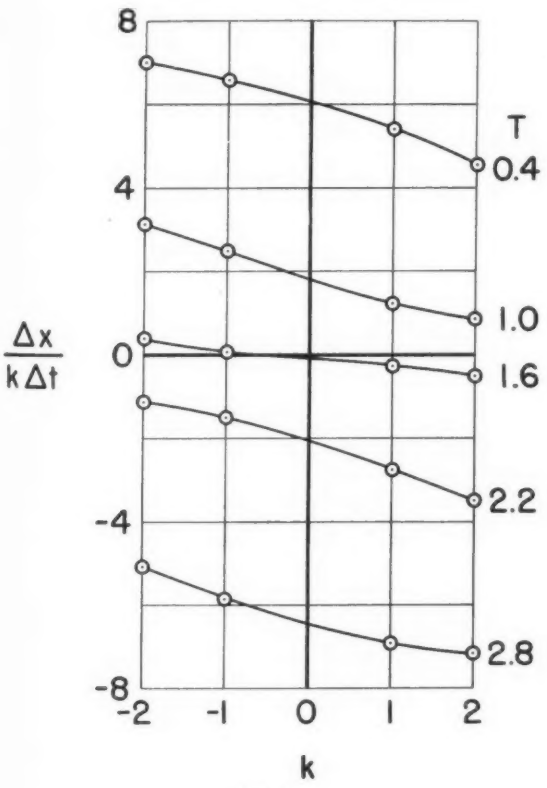

FIG. 2.

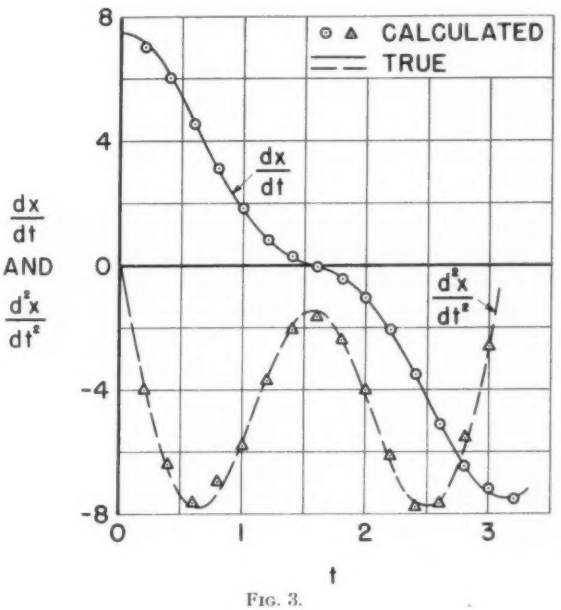

FIG. 3.

derivative curves. The root-mean-square errors in dx/dt and d^2x/dt^2 are 0.05 and 0.18, respectively—significantly smaller (especially for the second derivative) than those obtained when other well-known graphical and numerical differentiation methods were applied to the given data.

REFERENCE

[1] Greenberg, Harry, *A Survey of Methods for Determining Stability Parameters of an Airplane from Dynamic Flight Measurements*, NACA TN 2340, 1951.

Leading-Edge Separation from Delta Wings at Supersonic Speeds

Mac C. Adams
Cornell University, Ithaca, N.Y.
March 23, 1953

IN A RECENT PAPER, Legendre[1] has treated approximately the problem of leading-edge separation from flat-plate delta wings. His method, in brief, is to consider the problem as a potential flow and to represent the separation by concentrated vortices as in the figure. A further simplification is made by considering the flow in cross-planes perpendicular to the wing surface (i.e., the Jones low aspect ratio theory). The restriction to supersonic speeds is inherent in Legendre's treatment because conical flow is assumed. The method, however, may give an indication of the subsonic behavior if the aspect ratio is extremely small.

In unpublished work at Langley Field (NACA) C. E. Brown and the writer have considered this problem using the same approach as that of Legendre. However, there is a discrepancy in the determination of the lift, which will be briefly discussed below. The purpose of this note is to give what is believed to be a correct interpretation of Legendre's results and to show further that the simplified model of the real flow leads to some inconsistencies.

Referring to Fig. 1, the more realistic model would have, instead of concentrated vortices, vortex spirals or sheets such as the lines A-B extending to vortex cones. Such lines would represent mathematical barriers across which there would be a potential jump but a continuous pressure. Now if the vortex sheets are not considered, as in the simplified model, the barriers A-B are still necessary in order to render a single-valued solution. Unfortunately, however, the logarithmic singularity due to a concentrated vortex leads to the unrealistic result that a pressure jump exists in the field across the lines A-B. This same pressure jump exists across the wing surface in addition to the pressure difference as computed by Legendre. By ignoring this pressure jump on the wing surface Legendre obtains extremely small negative lift coefficients for small angles of attack. By simply adding to Legendre's result, the lift contributed by the pressure jump on the wing, as discussed above, the lift coefficient becomes, for small angles of attack,

$$C_L = \frac{\pi}{2}\,\text{A.R.}\alpha + \pi\left(1 + \frac{1}{2\sqrt{2}}\right)(4\text{A.R.})^{1/2}\,\alpha^{3/2}$$

where A.R. denotes aspect ratio and α the angle of attack in radians.

It is also interesting to calculate the lift by means of the well-known impulse method of Munk. In this case a less lift results because the negative lift carried on the barriers A-B is also included. The lift coefficient given by this second method is, for small angles of attack,

$$C_L = (\pi/2)\,\text{A.R.}\alpha + \pi(4\,\text{A.R.})^{1/2}\,\alpha^{3/2}$$

The inconsistency in these two different lift coefficients is clearly due to the simplified model considered (i.e., the condition of vortex continuity is violated in ignoring the vortex feedlines to the cores).

It is not intended to say which, if either, of these results is correct. It is reasonable to say that the difference in the lift coefficients is a measure of the error introduced by the simplified model. It is noteworthy that both results give the same behavior. The linear term is the same as Jones' low aspect ratio result and the nonlinear term gives an increase in lift coefficient proportional to $\text{A.R.}^{1/2}\,\alpha^{3/2}$. The lift also changes sign correctly for negative angles of attack.

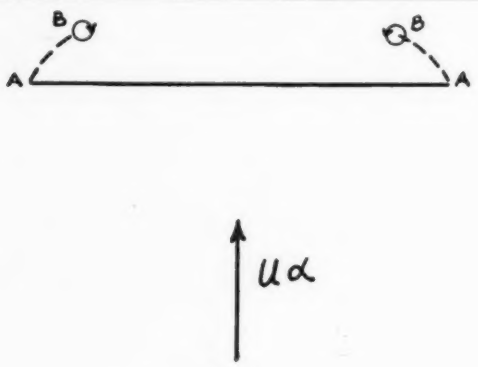

FIG. 1.

REFERENCE

[1] Legendre, Robert, *Écoulement au Voisinage De La Pointe Avant D'une Aile A Forte Flèche Aux Incidences Moyennes*, La Recherche Aeronautique, Bulletin Bimestriel, De L'Office National D'Études Et De Recherches Aéronautiques, Novembre-Décembre, 1952, and Janvier-Février, 1953.

Improvement of Pressure Recovery of a Fixed Diffuser by Means of Suction

Ashton M. Patterson†
Institute of Aerophysics, University of Toronto, Toronto, Ontario, Canada
February 13, 1953

PRESSURE RECOVERY in a supersonic wind tunnel is important because the power requirements for a continuous tunnel decrease and the running times of an intermittent wind tunnel increase with increase in pressure recovery. The pressure recovery of a fixed diffuser is limited by the "starting condition" of the supersonic wind tunnel. When the control valve of the intermittent blowdown wind tunnel is opened, the downstream pressure drops and the flow of air through the tunnel is accelerated.[1] When the velocity of sound (a_*) is reached in the throat of the nozzle (A_*), the flow expands to supersonic velocity in the nozzle and is converted to subsonic velocity through a shock wave (starting shock wave). As the downstream pressure continues to decrease, the shock wave moves down the nozzle, and the velocity at the diffuser throat (A_{*_2}) increases. Once the velocity of sound (a_{*_2}) is reached in the diffuser throat, the diffuser acts as a nozzle, and no further drop in the downstream pressure will affect conditions upstream of the diffuser throat. The mass flow through

† Research Assistant, Institute of Aerophysics. Now, Research Engineer, Ford Scientific Laboratory, Dearborn, Mich.

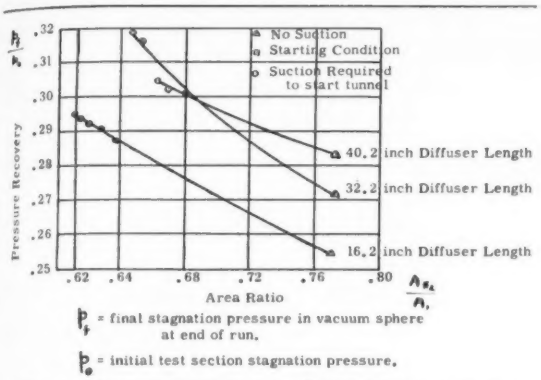

FIG. 1. Pressure recovery vs. diffuser throat area ratio.

the two throats is

$$\rho_* a_* A_* = \rho_{*2} a_{*2} A_{*2} \tag{1}$$

Using the energy equation and the relation $a^2 = \gamma p/\rho$, Eq. (1) can be changed to

$$A_*/A_{*2} = p_{0_2}/p_0 \tag{2}$$

where (p_{0_2}/p_0) is the stagnation pressure ratio across the normal shock wave. As the shock wave moves down the nozzle, it occurs at higher Mach Numbers, and the ratio p_{0_2}/p_0 decreases in value and has a minimum value when the shock wave occurs in the test section (A_1). As the starting shock wave will jump to some position downstream of the diffuser throat once it enters the diffuser, the tunnel will start when

$$A_*/A_{*2} \leq (p_{0_2}/p_0)_{min}. \tag{3}$$

(starting condition). The assumption that the wind tunnel starts with a normal shock wave introduces a small error into the calculation of the size of the diffuser throat that will allow the tunnel to run supersonically. [For short diffuser lengths the diffuser throat opening can be about 5 per cent smaller than that calculated from Eq. (3).] Therefore, Eq. (3) gives a good approximation for the calculation of the diffuser throat "starting" area.

In order to improve the pressure recovery of the wind tunnel over that obtained with a diffuser having a throat area the size that the "starting condition" will permit, the diffuser throat area must be made smaller. If the throat area (A_{*2}) is smaller than $A_*/(p_{0_2}/p_0)_{min}$, then the shock wave will stand in the nozzle and the tunnel will not "start." The mass flow through the diffuser throat is $\rho_{*2}' a_{*2}' A_{*2}$ and is equal to the mass flow through the nozzle throat. (ρ_{*2}' and a_{*2}' define the density and velocity of sound at the diffuser throat when the shock wave is standing in the nozzle.) If the shock wave was standing at the end of the nozzle blocks (starting condition), the mass flow through the diffuser throat would be $\rho_{*2} a_{*2} A_{*2}$. As the shock wave occurs at a higher Mach Number in the second case, $\rho_{*2} < \rho_{*2}'$. Therefore the diffuser throat cannot handle all the mass flow of the tunnel, and the mass flow that must be removed before the tunnel will run supersonically is

$$m = (\rho_{*2}' - \rho_{*2}) a_{*2} A_{*2} \tag{4}$$

If sufficient suction is applied upstream of the diffuser throat, the excess mass flow will be removed, and the tunnel will "start." Once the tunnel is "started," the suction can be discontinued, and the wind tunnel will continue to run supersonically.

Preliminary experimental work was done in the 5- by 7-in. blowdown-type supersonic wind tunnel at the Institute of Aerophysics on the application of suction for initiating supersonic flow in the tunnel.[2] The wedge-type diffuser used was constructed so that slots of different shapes and sizes could be inserted upstream of the diffuser throat and so that the diffuser throat area could be adjusted between tunnel runs. The slots were connected by means of a flexible metal hose to a small vacuum tank, which was used as the suction source. The most efficient slot of those tested had a rounded inlet lip and a width the order of magnitude of the boundary-layer thickness.[3] With the diffuser throat area smaller than $A_*/(p_{0_2}/p_0)_{min.}$, the control valve was opened (the tunnel would not run supersonically); suction was then applied, and once the tunnel started, the suction was discontinued.

Calculation of the excess mass flow [Eq. (4)] for the smallest diffuser throat area obtained showed that 19 cu.ft. per sec. at a pressure of 127 mm. Hg and a density of 4.54×10^{-4} slugs per cu.ft. had to be removed by suction before the tunnel would start. This amount checked well with the actual volume of air removed in the short time required for the tunnel to start (approximately $^1/_{10}$ sec.).

Fig. 1 shows the improvement in pressure recovery that was obtained by using suction to initiate supersonic flow in the tunnel. The improvement in the pressure recovery was only of the order of 3 per cent over that obtained with a diffuser that would allow the tunnel to start without suction being applied. This small increase in pressure recovery indicated that the use of suction by itself would not give large increases of pressure recovery for fixed diffusers. Further work should be done on slots and suction systems to determine the maximum usefulness of suction. It was found, however, that, if a long constant area throat section[4] was inserted immediately downstream of diffuser throat (Fig. 2), the combination of the long throat and suction

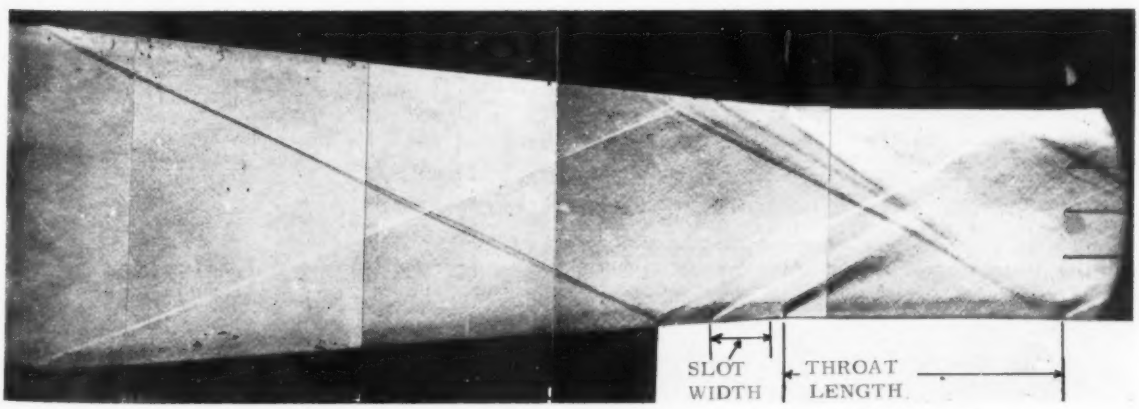

FIG. 2. Sixteen-and-two-tenths-in. diffuser length containing suction slots and 6-in. throat length.

to start the tunnel would improve the pressure recovery considerably. The improvement that was obtained in the 5- by 7-in. wind tunnel using a 6-in. constant-area throat length and suction was about 15 per cent over the best pressure recovery obtained with a fixed diffuser designed for the "starting condition."

References

[1] Bull, G. V., *Starting Processes in an Intermittent Supersonic Wind Tunnel*, UTIA Report No. 12, February, 1951.

[2] Patterson, A. M., *Factors Affecting the Performance of Supersonic Diffusers*, UTIA Report No. 23, December, 1952.

[3] Pierpont, P. Kenneth, *Investigation of Suction Slot Shapes for Controlling a Turbulent Boundary Layer*, NACA 1292, June, 1947.

[4] Kantrowitz, Arthur, and Neice, Stanford E., *Stabilization of Shock Waves in Channel Flow*, Readers' Forum, Journal of the Aeronautical Sciences, Vol. 17, No. 5, p. 316, May, 1950.

The Two-Dimensional Incompressible Aerodynamic Coefficients for Oscillatory Changes in Airfoil Camber

Irvin N. Spielberg

Wright Air Development Center, Wright-Patterson Air Force Base, Ohio

March 2, 1953

CERTAIN TYPES OF WINGS, notably those with low thickness ratio and low aspect ratio, are known to undergo rather pronounced deformations of chordwise sections when oscillating in their normal modes of vibration. Such deformations change the camber of the wing profile and, hence, can be expected to affect the aerodynamic pressure acting on the wing when it vibrates during flight. The significance, from the standpoint of flutter, of the nonstationary aerodynamic effects associated with camber changes is not fully known at present. In this note the two-dimensional, incompressible aerodynamic coefficients associated with harmonic changes in camber are derived. The derivation makes use of the linearized aerodynamic equations relating the pressure on the profile to the downwash distribution, as outlined in reference 1. Only one particular mode of camber deformation is studied—namely, parabolic bending of the profile mean chord line—although the derivation can easily be extended to other chordwise deformation patterns.

A thin airfoil of chord $2b$, immersed in a uniform stream of velocity V in the direction of the positive x axis, is considered to be undergoing small amplitude harmonic oscillations at right angles to the direction of the stream. Under the usual assumptions of thin airfoil theory, the actual profile is replaced by its mean chord, which in the rest position is supposed to lie on the x axis extending from $x = -1$ (leading edge) to $x = +1$ (trailing edge) with x nondimensionalized by the semichord b. If z represents the actual vertical motion of any point on the mean chord, positive down, then linearized theory gives for the downwash

$$w = [(V/b)\,(\partial z/\partial x)] + (\partial z/\partial t) \tag{1}$$

Assuming the oscillations are simple harmonic of the form $e^{i\omega t}$, ω being the circular frequency, Eq. 1 reduces to

$$w = (V/b)\,[(\partial z/\partial x) + ikz] \tag{2}$$

where $k = b\omega/V$ is the reduced frequency. The subsequent development follows the procedure outlined in reference 1. A new chordwise coordinate, $x = -\cos\theta$, is introduced and w is expanded in the Fourier series,

$$w(\theta, t) = Ve^{i\omega t}\left(P_0 + 2\sum_1^\infty P_n \cos n\theta\right) \tag{3}$$

Then the pressure difference between the upper and lower sides of the mean line is given by

$$\Pi(\theta, t) = -\rho V^2 e^{i\omega t}\left(2a_0 \operatorname{cotan}\frac{\theta}{2} + 4\sum_1^\infty a_n \frac{\sin n\theta}{n}\right) \tag{4}$$

where, contrary to the notation of reference 1, the negative sign has been introduced here to give the pressure jump in the direction of positive forces—i.e., downward—in accordance with usual U.S. flutter notation. The following relations then hold between the coefficients P_n and a_n:

$$\left.\begin{aligned} a_0 &= C(k)\,(P_0 - P_1) + P_1 \\ a_n &= \frac{ik}{2}\,(P_{n-1} - P_{n+1}) - nP_n, \quad n \geqq 1 \end{aligned}\right\} \tag{5}$$

where $C(k) = F(k) + iG(k)$ is the Theodorsen circulation function.

Although this note is primarily concerned with the nonstationary aerodynamic coefficients associated with camber changes, with little additional work the coefficients for translational and pitching oscillations can also be obtained. It is therefore intended to treat the following three types of motions:

$$\left.\begin{aligned} z_1(x) &= he^{i\omega t}, \text{ translation of the mean chord with amplitude } h, \text{ positive down} \\ z_2(x) &= \alpha b[x + (1/2)]e^{i\omega t}, \text{ rotation of the mean chord about the quarter-chord point with angular amplitude } \alpha, \text{ positive nose up} \\ z_3(x) &= \zeta(1 - x^2)e^{i\omega t}, \text{ parabolic change in camber of mean chord with amplitude } \zeta \text{ measured at the mid-chord point, positive down} \end{aligned}\right\} \tag{6}$$

The pressure distribution corresponding to each of these motions is obtained directly by applying Eqs. 2 through 5 as follows: Note that for convenience the factor $e^{i\omega t}$ is omitted temporarily.

For z_1:

$$w_1(\theta) = (iVk)\,(h/b)$$

$$P_0 = (ik)\frac{h}{b}, \quad P_n = 0, \quad n \geqq 1$$

$$\left.\begin{aligned} a_0 &= [ikC(k)]\,\frac{h}{b} = a_{0h}\,\frac{h}{b} \\ a_1 &= \left(-\frac{k^2}{2}\right)\frac{h}{b} = a_{1h}\,\frac{h}{b} \\ a_n &= 0, \quad n > 1 \end{aligned}\right\} \tag{7}$$

For z_2:

$$w_2(\theta) = V\left[\left(1 + i\frac{k}{2}\right) - ik\cos\theta\right]\alpha$$

$$P_0 = \left(1 + i\frac{k}{2}\right)\alpha, \quad P_1 = \left(-i\frac{k}{2}\right)\alpha, \quad P_n = 0, \quad n > 1$$

$$\left.\begin{aligned} a_0 &= \left[(1 + ik)C(k) - i\frac{k}{2}\right]\alpha = a_{0\alpha}\,\alpha \\ a_1 &= \left(ik - \frac{k^2}{4}\right)\alpha = a_{1\alpha}\,\alpha \\ a_2 &= (k^2/4)\alpha = a_{2\alpha}\,\alpha \\ a_n &= 0, \quad n > 2 \end{aligned}\right\} \tag{8}$$

For z_3:

$$w_3(\theta) = V\left(i\frac{k}{2} + 2\cos\theta - i\frac{k}{2}\cos 2\theta\right)\frac{\zeta}{b}$$

$$P_0 = \left(i\frac{k}{2}\right)\frac{\zeta}{b}, \quad P_1 = \frac{\zeta}{b}$$

$$P_2 = \left(-i\frac{k}{4}\right)\frac{\zeta}{b}, \quad P_n = 0, \; n > 2$$

$$
\left.\begin{aligned}
a_0 &= \left[\left(-1 + i\frac{k}{2}\right)C(k) + 1\right]\frac{\zeta}{b} &&= a_{0\zeta}\frac{\zeta}{b}\\
a_1 &= \left(-1 - \frac{3}{8}k^2\right)\frac{\zeta}{b} &&= a_{1\zeta}\frac{\zeta}{b}\\
a_2 &= (ik)\frac{\zeta}{b} &&= a_{2\zeta}\frac{\zeta}{b}\\
a_3 &= \left(\frac{k^2}{8}\right)\frac{\zeta}{b} &&= a_{3\zeta}\frac{\zeta}{b}\\
a_n &= 0, \quad n > 3
\end{aligned}\right\} \tag{9}
$$

Hence,

$$
\begin{aligned}
\Pi(h, \alpha, \zeta, \theta) = {} & \\
& -\rho V^2\left[2\cot\frac{\theta}{2}\left(a_{0h}\frac{h}{b} + a_{0\alpha}\alpha + a_{0\zeta}\frac{\zeta}{b}\right) + \right.\\
& 4\sin\theta\left(a_{1h}\frac{h}{b} + a_{1\alpha}\alpha + a_{1\zeta}\frac{\zeta}{b}\right) + 2\sin 2\theta \times\\
& \left.\left(a_{2\alpha}\alpha + a_{2\zeta}\frac{\zeta}{b}\right) + \frac{4}{3}\sin 3\theta\left(a_{3\zeta}\frac{\zeta}{b}\right)\right] \qquad (10)
\end{aligned}
$$

The generalized aerodynamic forces and moments can be obtained through the use of the virtual work principle. The virtual work corresponding to a virtual displacement in any of the three types of motion is

$$
\delta W_j = b\int_{-1}^{1}\Pi(h, \alpha, \zeta, \theta)\delta z_j\, dx, \quad j = 1, 2, 3 \qquad (11)
$$

where

$$
\left.\begin{aligned}
\delta z_1 &= \delta h\\
\delta z_2 &= b[x + (1/2)]\delta\alpha\\
\delta z_3 &= (1 - x^2)\delta\zeta
\end{aligned}\right\} \tag{12}
$$

Substituting 10 and 12 in 11 and performing the necessary integrations yields:

$$
\left.\begin{aligned}
\delta W_1 = {} & -\rho V^2 b\delta h\left[2\left(a_{0h}\frac{h}{b} + a_{0\alpha}\alpha + a_{0\zeta}\frac{\zeta}{b}\right)(\pi) + \right.\\
& \left. 4\left(a_{1h}\frac{h}{b} + a_{1\alpha}\alpha + a_{1\zeta}\frac{\zeta}{b}\right)\left(\frac{\pi}{2}\right)\right]\\
\delta W_2 = {} & -\rho V^2 b^2\delta\alpha\left[4\left(a_{1h}\frac{h}{b} + a_{1\alpha}\alpha + a_{1\zeta}\frac{\zeta}{b}\right)\left(\frac{\pi}{4}\right) + \right.\\
& \left. 2\left(a_{2\alpha}\alpha + a_{2\zeta}\frac{\zeta}{b}\right)\left(-\frac{\pi}{4}\right)\right]\\
\delta W_3 = {} & -\rho V^2 b\delta\zeta\left[2\left(a_{0h}\frac{h}{b} + a_{0\alpha}\alpha + a_{0\zeta}\frac{\zeta}{b}\right)\left(\frac{\pi}{2}\right) + \right.\\
& \left. 4\left(a_{1h}\frac{h}{b} + a_{1\alpha}\alpha + a_{1\zeta}\frac{\zeta}{b}\right)\left(\frac{3\pi}{8}\right) + \frac{4}{3}\left(a_{3\zeta}\frac{\zeta}{b}\right)\left(-\frac{\pi}{8}\right)\right]
\end{aligned}\right\} \tag{13}
$$

If now the right-hand sides of Eqs. 13 are multiplied and divided by $b^2\omega^2$, if the time-dependency factor is reintroduced, and if the definitions of equations (7), (8), and (9) are inserted, the following expressions are obtained for the generalized forces:

$$
\left.\begin{aligned}
L &= \frac{\delta W_1}{\delta h} = \pi\rho b^3\omega^2 e^{i\omega t}\left(L_h\frac{h}{b} + L_\alpha\alpha + L_\zeta\frac{\zeta}{b}\right)\\
M &= \frac{\delta W_2}{\delta\alpha} = \pi\rho b^4\omega^2 e^{i\omega t}\left(M_h\frac{h}{b} + M_\alpha\alpha + M_\zeta\frac{\zeta}{b}\right)\\
N &= \frac{\delta W_3}{\delta\zeta} = \pi\rho b^3\omega^2 e^{i\omega t}\left(N_h\frac{h}{b} + N_\alpha\alpha + N_\zeta\frac{\zeta}{b}\right)
\end{aligned}\right\} \tag{14}
$$

where

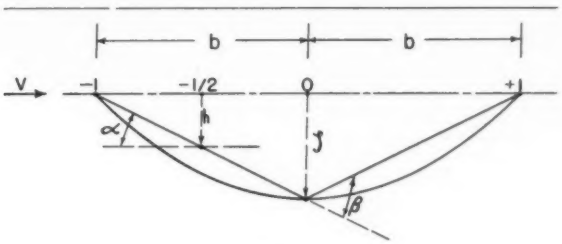

FIG. 1.

$$
\left.\begin{aligned}
L_h &= 1 - i\frac{2}{k}C(k)\\
L_\alpha &= \frac{1}{2} - i\frac{1}{k} - i\frac{2}{k}C(k) - \frac{2}{k^2}C(k)\\
L_\zeta &= \frac{3}{4} - i\frac{1}{k}C(k) + \frac{2}{k^2}C(k)\\
M_h &= 1/2\\
M_\alpha &= (3/8) - i(1/k)\\
M_\zeta &= \frac{3}{8} + i\frac{1}{2k} + \frac{1}{k^2}\\
N_h &= \frac{3}{4} - i\frac{1}{k}C(k)\\
N_\alpha &= \frac{3}{8} - i\frac{1}{k} - i\frac{1}{k}C(k) - \frac{1}{k^2}C(k)\\
N_\zeta &= \frac{7}{12} - i\frac{1}{2k}C(k) + \frac{1}{2k^2} + \frac{1}{k^2}C(k)
\end{aligned}\right\} \tag{15}
$$

and where L is the oscillatory lift on the airfoil, M is the oscillatory moment about the airfoil quarter-chord, and N corresponds to a second moment about the airfoil mid-chord point. In the expressions for the forces and moments of Eqs. (14) and (15), the notation of reference 2 has been adhered to. The coefficients L_h, L_α, M_h, and M_α are tabulated as functions of $1/k$ in reference 2. The remaining coefficients L_ζ, M_ζ, N_h, N_α, and N_ζ are tabulated in reference 3.

In order to introduce the camber change coefficients in a practical flutter analysis, it would probably be most convenient to use the normal modes of vibration of the wing as degrees of freedom. However, the chordwise, as well as the spanwise, distribution of amplitude in each normal mode would have to be known. In each mode and at each of several stations along the wing span, the actual deformation of the mean chord line would be plotted and then reduced to equivalent h, α, and ζ components. The aerodynamic terms would thus be treated by strip theory, although the mechanical terms could be handled on a "three-dimensional" basis. Such a flutter analysis procedure might be highly approximate, but it would represent a relatively simple initial approach to the problem of accounting for the effects of camber changes in flutter.

A rough indication of the magnitude of the lift and pitching moment due to parabolic camber change can be given by replacing the parabola with a triangle, as shown in Fig. 1. This triangular deflection pattern corresponds to a wing that translates an amount h, rotates through an angle α about the quarter-chord point, and has a 50 per cent chord control surface, hinged at its leading edge, which deflects through an angle β relative to the wing. In order that the maximum deflections in the two cases may be the same, it is necessary to set $h/b = 1/2$, $\alpha = 1$, $\beta = -2$, and $\zeta/b = 1$. The oscillatory lift and moment per unit span in the two cases are, then:

$$
\left.\begin{aligned}
L &= \pi\rho b^3\omega^2 e^{i\omega t}[L_h(h/b) + L_\alpha\alpha + L_\beta\beta]\\
M &= \pi\rho b^4\omega^2\, e^{i\omega t}[M_h(h/b) + M_\alpha\alpha + M_\beta\beta]
\end{aligned}\right\} \textit{(triangular)}
$$

and

$$\left.\begin{aligned} L &= \pi\rho b^3\omega^2\, e^{i\omega t}[L_\zeta(\zeta/b)] \\ M &= \pi\rho b^4\omega^2\, e^{i\omega t}[M_\zeta(\zeta/b)] \end{aligned}\right\} \text{(parabolic)}$$

For purposes of comparison, one need examine only the terms in the brackets in each case—i.e.

$$\left.\begin{aligned} &(1/2)L_h + L_\alpha - 2L_\beta \\ &(1/2)M_h + M_\alpha - 2M_\beta \end{aligned}\right\} \text{(triangular)}$$

and

$$\left.\begin{aligned} &L_\zeta \\ &M_\zeta \end{aligned}\right\} \text{(parabolic)}$$

Using the formulas of reference 2 for L_β and M_β and Eq. (15) for the other aerodynamic coefficients, one obtains

$$\left.\begin{aligned} \frac{1}{2}L_h + L_\alpha - 2L_\beta &= 0.576 - 0.727\, i\,\frac{1}{k}\,C(k) + \\ &\qquad 1.273\,\frac{1}{k^2}\,C(k) \\ L_\zeta &= 0.75 - i\,\frac{1}{k}\,C(k) + 2\cdot\frac{1}{k^2}\,C(k) \end{aligned}\right\} \tag{16}$$

$$\left.\begin{aligned} \frac{1}{2}M_h + M_\alpha - 2M_\beta &= 0.288 + 0.424\, i\,\frac{1}{k} + 0.637\,\frac{1}{k^2} \\ M_\zeta &= 0.375 + 0.5\, i\,\frac{1}{k} + \frac{1}{k^2} \end{aligned}\right\} \tag{17}$$

The two expressions for the lift and moment are of identical form, differing only in the numerical coefficients of each term.

In case a more accurate realization of a particular camber deformation pattern is desired than can be obtained with either the parabolic or two-segment approximation, two alternatives are available: (1) Derive the aerodynamic terms for higher order modes of camber deflection using the general method presented above; or (2) Employ more straight-line segments. Both possibilities have the drawback of adding considerably to the computational labor involved in performing a flutter analysis.

References

[1] Kussner, H. G., and Schwarz, L., *The Oscillating Wing with Aerodynamically Balanced Elevator*, NACA TM 991, October, 1941.

[2] Smilg, B., and Wasserman, L. S., *Application of Three-Dimensional Flutter Theory to Aircraft Structures*, Air Force Technical Report No. 4798, July, 1942.

[3] Spielberg, I. N., *The Two-Dimensional Incompressible Aerodynamic Coefficients for Oscillatory Changes in Airfoil Camber*, Wright Air Development Center Technical Note WCNS 52-7, August 18, 1952.

Note on the Use of Two-Dimensional Compressible Flow Aerodynamic Coefficients in the Flutter Analysis of a Tapered Wing

R. J. Werdes

Design Engineer, McDonnell Aircraft Corporation, St. Louis

March 20, 1953

A METHOD IS OUTLINED which makes it possible to compile, in a compact table for use with little or no subsequent interpolation, the various compressible flow aerodynamic coefficients used in the flutter analysis of a tapered wing.

In the practical analysis of the flutter characteristics of a tapered wing, the span is usually idealized as a composite of constant chord sections. This or similar treatment is necessary when considering the effect of spanwise variation in elastic deformation and the effect of surface taper. The two-dimensional aerodynamic coefficients defining the forces and moments at these sections are functions of the reduced wave length $1/k$ defined as $v/b\omega$. where v is the forward velocity, b is the section semichord, and ω is the circular frequency of oscillation. Thus, for a value of v/ω constant over the entire wing, a different value of $1/k$ is defined at each section. While almost any convenient sectioning of the span is adequate when considering the effect of elastic deformation, a judicious sectioning of the span will greatly simplify the calculations when considering the effect of surface taper.

TABLE 1
Values of $1/k$ for $R = 2^{1/8}$

0.50000	2.0000	8.0000
0.54525	2.1810	8.7241
0.59460	2.3784	9.5137
0.64842	2.5937	10.375
0.70711	2.8284	11.314
0.77111	3.0844	12.338
0.84090	3.3636	13.454
0.91700	3.6680	14.672
1.0000	4.0000	16.000
1.0905	4.3620	17.448
1.1892	4.7568	19.027
1.2968	5.1874	20.749
1.4142	5.6569	22.627
1.5422	6.1688	24.675
1.6818	6.7272	26.909
1.8340	7.3360	29.344
		32.000

Suppose the two-dimensional aerodynamic coefficients have been tabulated corresponding to values of $1/k$ which form a geometric series of ratio R. If the tapered wing under consideration is then idealized as a composite of constant chord sections oriented spanwise such that the section average chords also form a geometric series of ratio R, the aerodynamic coefficients required in the evaluation of the oscillatory forces and moments can be obtained directly from the prepared table. In particular, for $R = 2^{1/8}$, the aerodynamic coefficients would be tabulated for the values of $1/k$ given in Table 1. It will be noted that relatively few values of $1/k$ are required in covering the range of usual interest. Fig. 1 represents the tip portion of a nondimensionalized tapered wing of infinite span, the chords of which are normalized with respect to the tip chord, and on which a standard span is defined for a taper ratio of one-half. For $R = 2^{1/8}$, the sectioning is as shown in Fig. 1 with eight sections contained in each portion of span having a taper ratio of one-half. For a given taper ratio, the number of sections depends on the spanwise location of the normalized root chord. In most cases the root chord will not coincide with a standard section boundary. However, the aerodynamic coefficients applicable to this partial section can be conveniently written in terms of the adjacent section coefficients. The following relations are used in locating sections on the given wing span:

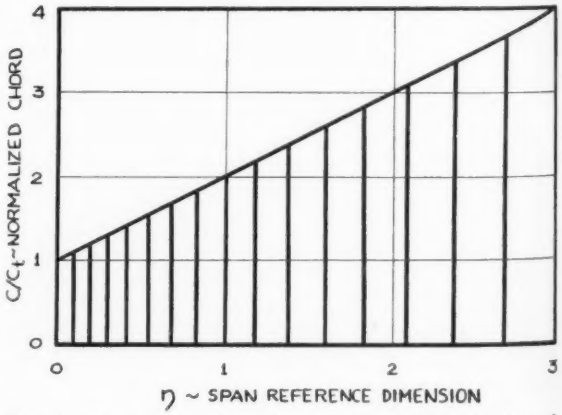

FIG. 1. Tip portion of nondimensionalized tapered wing of infinite span showing spanwise sectioning scheme.

UNIVERSITY OF MICHIGAN LIBRARIES

$$\eta_t = 0$$
$$\eta_r = (C_r/C_t) - 1$$
$$\eta_i = R^{i-1} - 1 \; (i = 1, 2, 3 \ldots)$$
$$(1/2)(\eta_i + \eta_{i+1}) = (1/2)(R + 1)(\eta_i + 1) - 1$$

where

η = span reference dimension
R = ratio of adjacent section chords
C = chord
i = subscript denoting section boundary location with $i = 1$ at the wing tip
r, t = subscripts denoting wing root and wing tip locations, respectively

For $R = 2^{1/8}$, the values of η_i can be obtained from Table 1 by subtracting unity from the values of $1/k$ starting with $1/k = 1$. When the value of $(\eta_r - \eta_t)$ has been established, all dimensions can be converted to full-scale wing dimensions.

The scheme outlined above is ideally suited to punched-card computational methods, since the functions can be stored with relatively few cards and practically no interpolation is required.

An Observation on the Vortex System of Dual-Rotation Propellers

J. J. Eisenhuth and B. W. McCormick
Research Associates, Ordnance Research Laboratory, The Pennsylvania State College, State College, Pa.
March 5, 1953

In order to determine the induced effects associated with a pair of dual-rotation propellers, it is commonly assumed that the vortex system aft of the propellers is formed by the intersection of right- and left-handed nondistorted helical vortex sheets.[1] Recent water-tunnel* experiments have shown that the above concept might be in considerable error. The accompanying high-speed photograph, Fig. 1, shows a dual-rotation propeller operating on the tail of a torpedo model. The outer edge of the vortex sheet is easily discernible because of the occurrence of cavitation in this low-pressure region. In addition to the use of high-speed photographs, the behavior of the tip vortices was viewed with stroboscopic light. These photographic and visual observations are extremely enlightening with regard to the qualitative nature of the combined trailing vortex system. The tip vortices trailing from the individual blades of each propeller intersect in the plane of the after propeller. The flow configuration is apparently unstable at these points of intersection. Instead of the vortices from each propeller blade maintaining their expected helical shapes, the ones from the forward propeller break and join with those from the after-propeller, forming a series of closed loops that move downstream with periodic spacing. In view of the observed behavior of the tip vortices, it is reasonable to assume that the inner portion of the vortex sheets must also undergo some similar distortion, thus invalidating the assumption of true helical surfaces.

* These tests were conducted in the 48-in. water tunnel of the Ordnance Research Laboratory, operated under Contact NOrd 7958 with the Bureau of Ordnance, Department of the Navy, by The Pennsylvania State College.

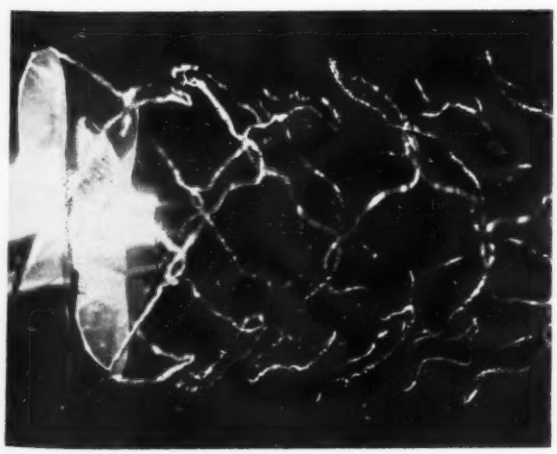

Fig. 1.

Reference

[1] Theodorsen, Theodore, *Theory of Propellers*, 1st Ed.; McGraw-Hill Book Company, Inc., New York, 1948.

A Note on Second-Order Supersonic Flow Theory

Robert E. Lavender
Technical Feasibility Studies Office, Ordnance Missile Laboratories, Redstone Arsenal, Huntsville, Ala.
January 21, 1953

Van Dyke has recently pointed out that the solution to the second-order equation for the supersonic flow past nonlifting bodies of revolution whose slope of the meridian line has discontinuities requires a superposition of five basic solutions to the first-order equation.[1] The writer feels that a discussion of the suitable strengths of these solutions is warranted.

Consider a body of revolution (Fig. 1) which has discontinuities in curvature or slope at points X_{k1} to X_{k4}. The first-order solution can be written as follows:

$$\varphi_n = -AX_n b(t_n) - \sum_{i=0}^{n-1} B_i (X_n - \xi_i)^2 a(\mathbf{T}_i^n) - \sum_{y=1}^{4} C_{ky} \times (X_n - \xi_{ky})^{2/2} g(\mathbf{T}_{ky}^n) - \sum_{y=1}^{4} D_{ky} \sqrt{X_n - \xi_{ky}}\, h(\mathbf{T}_{ky}^n) \quad (1)$$

where $C_{ky} = D_{ky} = 0$ for $X_n < X_{ky}$.

$$\varphi_{r_n} = A\beta e(t_n) + \beta \sum_{i=0}^{n-1} B_i (X_n - \xi_i)\, c(\mathbf{T}_i^n) + \beta \sum_{y=1}^{4} C_{ky} \sqrt{X_n - \xi_{ky}}\, i(\mathbf{T}_{ky}^n) + \beta \sum_{y=1}^{4} D_{ky} \times (X_n - \xi_{ky})^{-1/2} k(\mathbf{T}_{ky}^n) \quad (2)$$

$$\varphi_{t_n} = -Ad(t_n) - \sum_{i=0}^{n-1} B_i (X_n - \xi_i) b(\mathbf{T}_i^n) - \sum_{y=1}^{4} C_{ky} \sqrt{X_n - \xi_{ky}}\, h(\mathbf{T}_{ky}^n) - \sum_{y=1}^{4} D_{ky} \times (X_n - \xi_{ky})^{-1/2} j(\mathbf{T}_{ky}^n) \quad (3)$$

$$\varphi_{TT_n} = -A(X_n)^{-1} f(t_n) - \sum_{i=0}^{n-1} B_i d(\mathbf{T}_i^n) - \sum_{y=1}^{4} C_{ky} (X_n - \xi_{ky})^{-1/2} j(\mathbf{T}_{ky}^n) + \sum_{y=1}^{4} D_{ky} (X_n - \xi_{ky})^{-2/2} l(\mathbf{T}_{ky}^n) \quad (4)$$

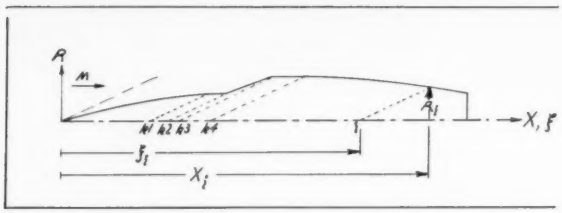

FIG. 1. Body of revolution.

As noted by Van Dyke,[1] the other second derivatives can be expressed by:

$$\varphi_{rr_n} = \beta^2 \varphi_{xx_n} - (\varphi_{r_n}/R_n) \tag{5}$$

$$\varphi_{xr_n} = R_n'' - R_n' \varphi_{rr_n} \quad (\text{for } \varphi_{r_n} = R_n') \tag{6}$$

Eqs. (1) through (6) give the first-order potential and its derivatives at station X_n along the body, where

$$\begin{aligned} t_n &= \beta R_n/X_n \\ t_0 &= \beta R_0', \quad X_0 = 1, R_0 = R_0', R_0'' = 0 \\ \mathrm{T}_i^n &= \beta R_n/(X_n - \xi_i) \\ \xi_i &= X_i - \beta R_i \end{aligned}$$

The functions $a(t)$ through $m(t)$ are defined and tabulated in the referenced report.

Taking the first-order tangency condition to be $\varphi_{r_n} = R_n'$ (as suggested by Van Dyke[1]),

$$A = \epsilon^2/\sqrt{1 - \beta^2\epsilon^2}, \quad \epsilon \equiv R_0' \tag{7}$$

$$B_{n-1} = \frac{1}{\beta(X_n - \xi_{n-1})c(\mathrm{T}_{n-1}^n)}\Bigg[R_n' - A\beta e(t_n) - \beta \sum_{i=0}^{n-2} B_i(X_n - \xi_i)c(\mathrm{T}_i^n) - \beta \sum_{y=1}^{4} C_{ky} \sqrt{X_n - \xi_{ky}}\, i(\mathrm{T}_{ky}^n) - \beta \sum_{y=1}^{4} D_{ky}(X_n - \xi_{ky})^{-1/2} k(\mathrm{T}_{ky}^n)\Bigg] \tag{8}$$

$$D_{ky} = (R_{kyb}' - R_{kya}')\sqrt{\beta R_{ky}}/\beta \tag{9}$$

$$C_{ky} = \frac{\sqrt{\beta R_{ky}}}{\beta - \beta^2 R_{kyb}'}\Bigg[R_{kyb}'' - (\varphi_{xr})_{kya} - R_{kyb}'(\varphi_{rr})_{kya} + \frac{(R_{kyb}' - R_{kya}')}{R_{ky}}\left(\frac{7}{8} R_{kyb}' - \frac{3}{8\beta}\right)\Bigg] \tag{10}$$

where $R_{kya}'' = R''$ just ahead of the discontinuity at station X_{ky} and $R_{kyb}'' = R''$ just behind the discontinuity at station X_{ky}. If the discontinuity at station X_{ky} is in curvature only and not in slope, Eqs. (9) and (10) reduce to

$$\begin{aligned} D_{ky} &= 0 \\ C_{ky} &= \frac{\sqrt{\beta R_{ky}}}{\beta - \beta^2 R_{kyb}'}(R_{kyb}'' - R_{kya}'') \end{aligned}$$

Eqs. (7) through (10) are the constants defining the strengths of the basic solutions which are needed to obtain the first-order potential and its derivatives.

A particular solution, ψ, to the second-order perturbation equation has been obtained by Van Dyke in terms of the first-order potential, φ, and its derivatives. The second-order potential, ϕ, consists of this particular solution plus a complementary solution, χ, to the first-order equation, so that (as given by Van Dyke[1])

$$\chi_{r_n} = R_n'(1 + \varphi_{x_n}) - \psi_{r_n} \tag{11}$$

The expressions for χ_x and χ_r can be written:

$$\chi_{r_n} = E\beta e(t_n) + \beta \sum_{i=0}^{n-1} F_i(X_n - \xi_i)c(\mathrm{T}_i^n) + \beta \sum_{y=1}^{4} G_{ky}(X_n - \xi_{ky})^{-1/2} k(\mathrm{T}_{ky}^n) + \beta \sum_{y=1}^{4} H_{ky}(X_n - \xi_{ky})^{-3/2} m(\mathrm{T}_{ky}^n) + \sum_{y=1}^{4} \beta\, J_{ky} \sqrt{X_n - \xi_{ky}}\, i(\mathrm{T}_{ky}^n) \tag{12}$$

where $G_{ky} = H_{ky} = J_{ky} = 0$ for $X_n < X_{ky}$ and

$$\chi_{x_n} = -Ed(t_n) - \sum_{i=0}^{n-1} F_i(X_n - \xi_i)b(\mathrm{T}_i^n) - \sum_{y=1}^{4} G_{ky}(X_n - \xi_{ky})^{-1/2} j(\mathrm{T}_{ky}^n) + \sum_{y=1}^{4} H_{ky}(X_n - \xi_{ky})^{-3/2} l(\mathrm{T}_{ky}^n) - \sum_{y=1}^{4} J_{ky} \sqrt{X_n - \xi_{ky}}\, h(\mathrm{T}_{ky}^n) \tag{13}$$

Eqs. (12) and (13), along with the values of ψ_{r_n} and ψ_{x_n} (obtainable[1] in terms of the first-order values), define the second-order perturbation velocities at station X_n along the body:

$$\left.\begin{aligned} \phi_{r_n} &= \psi_{r_n} + \chi_{r_n} \\ \phi_{x_n} &= \psi_{x_n} + \chi_{x_n} \end{aligned}\right\} \tag{14}$$

Taking the second-order tangency condition to be given by Eq. (11),

$$E = [R_0'(1 + \varphi_{x_0}) - \psi_{r_0}]/\beta e(t_0) \tag{15}$$

$$F_{n-1} = \frac{1}{\beta(X_n - \xi_{n-1})c(\mathrm{T}_{n-1}^n)}\Bigg[R_n'(1 + \varphi_{x_n}) - \psi_{r_n} - E\beta e(t_n) - \beta \sum_{i=0}^{n-2} F_i(X_n - \xi_i)c(\mathrm{T}_i^n) - \beta \sum_{y=1}^{4} G_{ky}(X_n - \xi_{ky})^{-1/2} k(\mathrm{T}_{ky}^n) - \beta \sum_{y=1}^{4} H_{ky}(X_n - \xi_{ky})^{-3/2} \times m(\mathrm{T}_{ky}^n) - \beta \sum_{y=1}^{4} J_{ky} \sqrt{X_n - \xi_{ky}}\, i(\mathrm{T}_{ky}^n)\Bigg] \tag{16}$$

In determining the constants defined by Eqs. (8) and (16) when X_n corresponds to a station X_{ky} with a discontinuity in R'' or R', take $X_n = X_{kya}$.

$$H_{ky} = (\psi_{kyb} - \psi_{kya})\sqrt{\beta R_{ky}} \tag{17}$$

$$G_{ky} = \frac{\sqrt{\beta R_{ky}}}{\beta}\Bigg[(R_{kyb}' - R_{kya}')\left(1 + \varphi_{xkya} - \frac{R_{kyb}'}{\beta}\right) - (\psi_{rkyb} - \psi_{rkya}) - \frac{3}{8R_{ky}}(\psi_{kyb} - \psi_{kya})\Bigg] \tag{18}$$

$$\left.\begin{aligned} J_{ky} &= G_{ky}(C_{ky}/D_{ky}), \quad D_{ky} \neq 0 \\ &= 0, \quad D_{ky} = 0 \end{aligned}\right\} \tag{19}$$

If the discontinuity at station X_{ky} is in curvature only and not in slope, Eqs. (17) and (18) reduce to

$$\begin{aligned} H_{ky} &= 0 \\ G_{ky} &= (-\sqrt{\beta R_{ky}}/\beta)(\psi_{r_{kyb}} - \psi_{r_{kya}}) \end{aligned}$$

Eqs. (15) through (19) are the constants defining the strengths of the basic solutions which are needed to obtain the complementary solutions from Eqs. (12) and (13). The generalization of the above equations for bodies with more than four discontinuities is easily seen.

As pointed out by Van Dyke, the proper expression for the second-order pressure coefficient is given by the exact expression:

$$C_{p_n} = \frac{2}{\gamma M^2}\left(\left\{1 + \frac{\gamma - 1}{2} M^2 \times [1 - (1 + \phi_{x_n})^2 - \phi_{r_n}^2]\right\}^{\gamma/(\gamma-1)} - 1\right)$$

where the second-order perturbation velocities are given by Eqs. (14).

UNIVERSITY OF MICHIGAN LIBRARIES

REFERENCE

[1] Van Dyke, Milton D., *Practical Calculation of Second-Order Supersonic Flow Past Nonlifting Bodies of Revolution*, NACA TN 2744, July, 1952.

Influence Matrix of Beam Vibration

L. S. Dzung
Brown, Boveri & Cie., Baden, Switzerland
February 13, 1953

THE DIFFERENTIAL EQUATION of beam vibration $(EI\ y'')'' = \mu\omega^2 y$ (E = Young's modulus, I = area moment of inertia, y = deflection, μ = mass per unit length, ω = angular frequency, and primes denote differentiation with respect to beam length) when applied to a uniform beam section (I and μ constant) is readily solved by standard methods and leads to the following matrix equation:[1]

$$\begin{bmatrix} y_{i+1} \\ \theta_{i+1} \\ M_{i+1} \\ S_{i+1} \end{bmatrix} = \begin{bmatrix} j & a & b & \bar{c} \\ u\bar{c} & j & \bar{a} & \bar{b} \\ ub & uc & j & a \\ ua & ub & u\bar{c} & j \end{bmatrix} \cdot \begin{bmatrix} y_i \\ \theta_i \\ M_i \\ S_i \end{bmatrix} \tag{1}$$

where $\theta = y'$, $M = EIy''$, $S = EIy'''$ denote the slope, the bending moment, and the shearing force, respectively. Subscripts i and $i + 1$ denote the left and right end of the section.

The elements of the influence matrix are:

$$\begin{aligned} j &= (1/2)(\cosh\alpha + \cos\alpha) \\ a = EI\bar{a} &= (1/2)(\sinh\alpha + \sin\alpha)(l/\alpha) \\ b = EIb &= (1/2)(\cosh\alpha - \cos\alpha)(l/\alpha)^2 \\ c = EI\bar{c} &= (1/2)(\sinh\alpha - \sin\alpha)(l/\alpha)^3 \\ u &= \mu\omega^2 \\ \alpha^4 &= \mu\omega^2 l^4/EI \end{aligned}$$

If the section length l is chosen short enough so that $\alpha^4 << 1$, the elements can be approximated by

$$\begin{aligned} j &= l^0/0! = 1 \\ a = EI\bar{a} &= l^1/1! = l \\ b = EIb &= l^2/2! = l^2/2 \\ c = EI\bar{c} &= l^3/3! = l^3/6 \end{aligned} \tag{2}$$

This is the result obtained by Morton.[2]

If the section is not uniform but if the changes of I and μ are small and can be approximated by straight-line variations along the beam length, then the differential equation can still be solved by series integration. The result is similar to Eq. (1), except that it is more convenient to use the quantities $y'' = \bar{M} = M/EI$, $y''' = \bar{S} = S/EI$. Eq. (1) becomes

$$\begin{bmatrix} y_{i+1} \\ \theta_{i+1} \\ \bar{M}_{i+1} \\ \bar{S}_{i+1} \end{bmatrix} = \begin{bmatrix} j & a & b & c \\ u\bar{c} & j & a & b \\ ub & uc & j & a \\ u\bar{a} & ub & u\bar{c} & j \end{bmatrix} \cdot \begin{bmatrix} y_i \\ \theta_i \\ \bar{M}_i \\ \bar{S}_i \end{bmatrix} \tag{3}$$

This equation is more symmetrical than Eq. (1) and, within the approximation of Eqs. (2), is applicable to a nonuniform beam as well, provided

$$\Delta I/I = 2\,\Delta\mu/\mu << k$$

where Δ denotes the difference between the values at station i and at station $i + 1$.

$$k = 2(4 + n)/(2 - n)$$

for $n = 1$ or 2—i.e., $k = 10$ or ∞. It is understood that the values of I and μ just to the right of station i are taken to calculate the matrix elements, while the values at the respective stations are taken for $\bar{M}$ and $\bar{S}$.

If a concentrated mass m is attached to the left end just to the right of station i, then the shearing force of the whole section is increased by $m\omega^2 y$. The first column of the matrix in Eq. (1) or (3) must be increased by $m\omega^2$ multiplied by the respective last column. For a massless beam, $\mu = 0$, this is the system of equations used by Prohl,[3] Myklestad,[4] Targoff,[5] and Thomson.[6]

If the same mass is attached to the right end just to the left of station $i + 1$, then the shearing force at station $i + 1$ is increased by $m\omega^2 y_{i+1}$. The last row of the matrix must be increased by $m\omega^2$ multiplied by its first row. For a massless beam, this is the equation given by Thomson.[1]

A word of caution is in order if, for the calculations of natural frequencies and natural modes, the entire beam is divided into sections to each of which Eq. (1) or (3) is applied. If the cross section of the beam varies smoothly—e.g., in case of an airplane wing—then M and S or $\bar{M}$ and $\bar{S}$ are usually continuous at the joint between two sections, except due to concentrated mass or external constraint. If the beam cross section changes abruptly at a station point—e.g. in case of a rotating shaft with stepwise varying diameters—then M and S are still continuous usually but not $\bar{M}$ and $\bar{S}$ due to abrupt change of I. In this case it is more appropriate to use Eq. (1) than Eq. (3), in order that the right end conditions of one section can be used directly as the left end conditions of next section.

REFERENCES

[1] Thomson, W. T., *Matrix Solution for the Vibration of Non-Uniform Beams*, J. Appl. Mech., Vol. 17, p. 337, 1950.

[2] Morton, A. J., *Tabular Methods for Critical Speed Calculations*, Engineering, Vol. 173, pp. 674, 704, 1952.

[3] Prohl, M. A., *A General Method for Calculating Critical Speeds of Flexible Rotors*, J. Appl. Mech., Vol. 12, p. A-142, 1945.

[4] Myklestad, N. O., *A New Method of Calculating Natural Modes of Uncoupled Bending Vibration of Airplane Wings and Other Types of Beams*, Journal of the Aeronautical Sciences, Vol. 11, No. 2, p. 153, April, 1944.

[5] Targoff, W. P., *The Associated Matrices of Bending and Coupled Bending Torsion Vibrations*, Journal of the Aeronautical Sciences, Vol. 14, No. 10, p. 579, October, 1947.

[6] Thomson, W. T.: *A Note on Tabular Methods for Flexural Vibrations*, Journal of the Aeronautical Sciences, Vol. 20, No. 1, p. 62, January, 1953.

Regarding the Computation of Unsteady Air Forces by Means of Mathieu Functions

Henry E. Fettis
Mathematician, Flight Research Laboratory, Wright Air Development Center, Wright-Patterson Air Force Base, Ohio
February 13, 1953

SINCE THE PUBLICATION OF the last letter on this subject by the author,[1] significant new results have been obtained from calculations performed by Dr. Gertrude Blanch, at the Institute for Numerical Analysis of the National Bureau of Standards at Los Angeles, based on the equations of Reissner[2] and Haskind.[4] Some preliminary results of these computations are shown in Table 1, together with the corresponding values by Dietze's method.[2] From these results it can be seen that essentially the same values are obtained by the exact solution in terms of Mathieu functions as were obtained by the approximate method, the effect of the approximation being confined to discrepancies (in general) in only the third significant figure. Thus it may be safely concluded both that Dietze's results are fundamentally correct and that the method of Mathieu functions can be made to duplicate results previously obtained by other means to a satisfactory degree of accuracy. It is also noted that the results obtained from the equations of Haskind and Reissner satisfy the relation

TABLE 1

Comparison of Lift and Moment Coefficients for $M = 0.7$ (a) Values by Reissner's Formulas; (b) Values by Dietze's Method

	L_h		M_h	
ω	a	b	a	b
0.6	$-0.05032-2.28919i$	$-0.0550-2.2922i$	$0.778961-0.40171i$	$0.7806-0.4053i$
0.7	$+0.03390-1.99385i$	$+0.02715-1.9977i$	$0.738792-0.44705i$	$0.7394-0.4535i$
	L_α		M_α	
ω	a	b	a	b
0.6	$-4.64460-1.80363i$	$-4.6581-1.7967i$	$-0.42508-2.85183i$	$-0.4258-2.8617i$
0.7	$-3.55325-1.59523i$	$-3.5630-1.5830i$	$-0.45912-2.43883i$	$-0.4691-2.4434i$

$$L_\alpha + M_h = [1 - (i/\omega)]L_h$$

identically with the exception of one unit in the fifth decimal place for $\omega = 0.6$, as shown in Table 2.

TABLE 2

ω	$L_\alpha + M_h$	$[1 - (i/\omega)]L_h$
0.6	$-3.86564-2.20534i$	$-3.86564-2.20533i$
0.7	$-2.81446-2.04228i$	$-2.81446-2.04228i$

In conclusion, the author wishes to say that the pointing out of the discrepancies that exist between the values of the coefficients as presented by the Messrs. Timman and van de Vooren and those otherwise computed is in no way intended to discredit either the validity of their method or the value of their work. It is, rather, to call attention to the presence of some (perhaps obscure) numerical error that has somehow entered into their calculation scheme.

REFERENCES

[1] Fettis, Henry E., *Comments on "Aerodynamic Coefficients of an Oscillating Airfoil in Two-Dimensional Subsonic Flow,"* Readers' Forum, Journal of the Aeronautical Sciences, Vol. 19, No. 5, pp. 353–354, May, 1952.

[2] Dietze, *The Air Forces of the Harmonically Vibrating Wing in a Compressible Medium at Subsonic Velocity, Part I*, AF Translation No. F-TS-506RS, August 9, 1946, 1947, and Chance Vought Report No. GTR-65, June, 1945.

[3] Reissner, Eric, *On The Application of Mathieu Functions in the Theory of Subsonic Compressible Flow Past Oscillating Airfoils*, NACA TN 2363.

[4] Haskind, M.D., *Oscillations of a Wing in a Subsonic Gas Flow*, Mat. I. Mekh. (Moscow), Vol. XI, No. 1, pp. 129–146, 1947 (in Russian). Also available as Translation No. A 9-T-22, Air Materiel Command and Brown University.

On the Measurement of Surface Pressure with a Static Probe

W. W. Willmarth
Graduate Student, Guggenheim Aeronautical Laboratory, California Institute of Technology, Pasadena, Calif.

March 2, 1953

SURFACE PRESSURES on two-dimensional bodies of small thickness ratio have been measured by traversing a conventional static pressure probe over the surface. The method can be applied to thin bodies that are difficult, if not impossible, to instrument with conventional surface pressure taps. The same method should prove useful in problems involving the shaping of aerodynamic surfaces to obtain a given pressure distribution, for example, in wind-tunnel tests on pylons, fuselage-wing fillets, etc.

The fact that surface pressures on thin bodies can be measured with precision at points off the surface depends on two effects. The first is the effect of viscosity in providing a boundary layer through which the static pressure is constant in a direction normal to the body surface when the surface curvature is small. The second effect depends on the fluid being irrotational outside of the boundary layer. In conventional notation, using two-dimensional perturbation velocities, u and v, the irrotationality condition is

$$u_y - v_x = 0 \tag{1}$$

The linearized boundary condition on the body surface is

$$v/U_\infty \doteq (\text{body slope}) \tag{2}$$

on $y = 0$, and the pressure coefficient is

$$C_p \doteq -(2u/U_\infty) \tag{3}$$

From Eqs. (1) and (2) it is apparent that in the inviscid flow near the surface the change in u in the y-direction is proportional

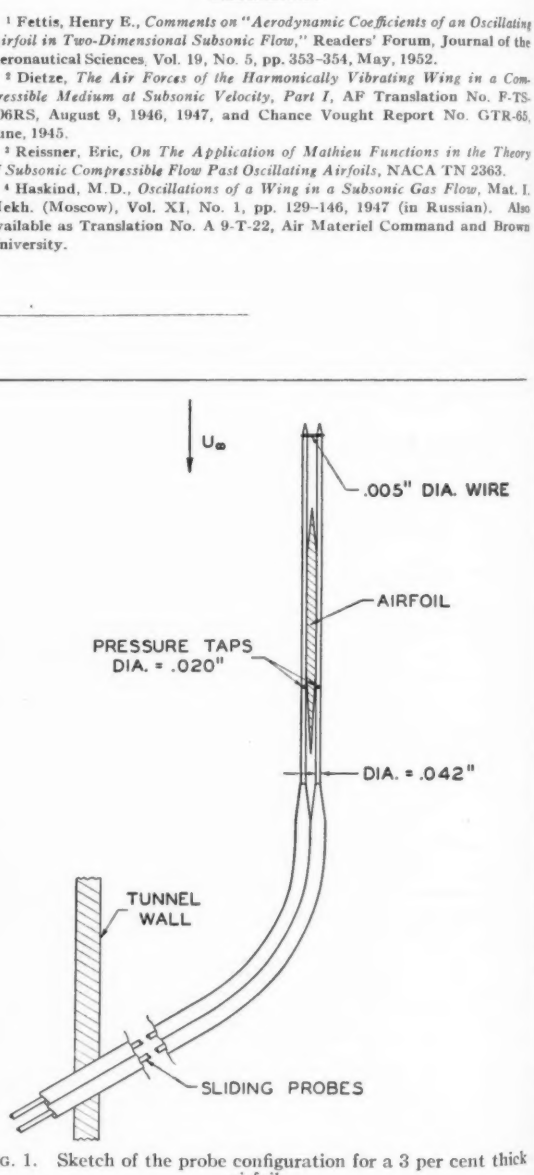

FIG. 1. Sketch of the probe configuration for a 3 per cent thick airfoil.

to the x-derivative of the slope of the body when the boundary-layer growth is small. For flat surfaces $\partial u/\partial y$ is negligible, and from Eq. (3) the pressure change normal to the surface ($y = 0$) will be extremely small. On slightly curved surfaces, the change of body slope is small and the normal pressure gradients must also be small.

Using the above considerations, a pair of slender static pressure probes aligned with the chord of a thin two-dimensional airfoil have been used to obtain surface pressure distributions at transonic speeds and small angles of attack. The probe arrangement on the airfoil cross section is shown in Fig. 1. In order to minimize tunnel blockage, the probes slide inside larger supporting tubes, which lead back from the airfoil and out through the tunnel wall. The probes were held together by a loop of wire approximately two diameters from the tips. The wire loop also made the probe boundary layer turbulent, which is important when measuring steep pressure gradients.[1] The ratio of probe diameter to airfoil thickness was of the order of one-half.

The effect of the small three-dimensional probe disturbances on the basic two-dimensional flow over the airfoil was checked with a Mach-Zehnder interferometer.[2] An interferogram of the flow over one surface of a 3 per cent thick airfoil was made and the pressure distribution was computed. The probes were then installed and used to find the surface pressure distribution. The airfoil was investigated for an angle of attack of approximately 1 deg. at two supersonic Mach Numbers. In one case, the bow shock wave was attached with completely supersonic flow over the airfoil. The second case was at a lower Mach Number with a detached bow wave giving subsonic flow over the front portion of the airfoil. The agreement between interferometer and probe measurements was good except in the vicinity of the airfoil nose, as shown in Fig. 2.

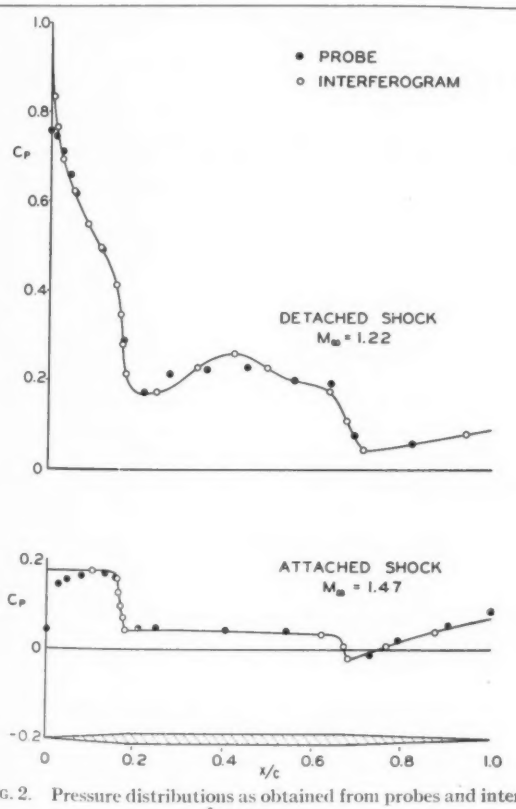

FIG. 2. Pressure distributions as obtained from probes and interferograms.

Using this probe technique, pressure distributions on a 5 per cent thick double wedge have been measured at high subsonic speeds.[3]

REFERENCES

[1] Liepmann, H. W., Roshko, A., and Dhawan, S., *On the Reflection of Shock Waves from Boundary Layers*, NACA TN 2334, p. 20, April, 1951.

[2] Ashkenas, H., and Bryson, A. E., *Design and Performance of a Simple Interferometer for Wind Tunnel Measurements*, Journal of the Aeronautical Sciences, Vol. 18, No. 2, p. 82, February, 1951.

[3] Cole, J. D., Solomon, G. E., and Willmarth, W. W., *Transonic Flow Past Simple Bodies*, presented at the Twenty-First Annual Meeting, IAS, New York, January 26–29, 1953.

Concerning "The Subsonic Calculation of Circulatory Spanwise Loadings for Oscillating Airfoils by Lifting-Line Techniques"[1]

M. A. Dengler and Martin Goland
Midwest Research Institute, Kansas City, Mo.
February 19, 1953

A REVIEW OF OUR PAPER shows that we do not make entirely clear the nature of the mode shapes used for the swept-wing calculations. Our intent was to study the effects of geometrically sweeping a plan form. Hence, after a calculation was performed for an unswept wing, a similar computation was made for a 45° swept wing *having the same geometric downwash along the rear quarter-chord line as the unswept case.* The paper is clear concerning the geometric downwash for the unswept wings; the geometric downwash boundary conditions for the swept wings are taken as identical.

We should also like to call attention to an inadvertent omission from our bibliography of the valuable series of papers by W. P. Jones. Among these are the *Aero. Res. Council Tech. Repts.*, R. and M. Nos. 1920, 2142, 2215, and 2470. The last paper bears particularly on our approach and presents a method by which Falkner's discrete-vortex scheme for calculating surface loadings can be made part of a technique for air-load calculations on oscillating, finite-span airfoils.

REFERENCE

[1] Dengler, M. A., and Goland, Martin, *The Subsonic Calculation of Circulatory Spanwise Loadings for Oscillating Airfoils by Lifting-Line Techniques*, Journal of the Aeronautical Sciences, Vol. 19, No. 11, p. 751, November, 1952.

Errata—"The von Kármán Integral Method as Applied to a Turbulent Boundary Layer"[1]

Nguyen Van Le
Preliminary Design Engineer, AiResearch Manufacturing Company, Los Angeles, Calif.
February 23, 1953

IN THE EQUATION PRECEDING Eq. (5), in Eqs. (5) and (6), and in the last equation, there should be

$$\int_0^\delta \frac{\partial^2}{\partial x^2}\overline{u'v'}\,dy$$

instead of

$$\int_0^\delta \frac{\partial}{\partial x} \overline{u'v'}\, dy$$

REFERENCE

[1] Van Le, Nguyen, *The von Kármán Integral Method as Applied to a Turbulent Boundary Layer*, Readers' Forum, Journal of the Aeronautical Sciences, Vol. 19, No. 9, p. 647, September, 1952.

Errata—"Elastic Stability of Simply Supported Flat Rectangular Plates..."[1]

Robert G. Noel
Aerophysics Laboratory, North American Aviation, Inc., Downey, Calif.
March 18, 1953

THE AUTHOR IS GRATEFUL TO Dr. Gorden C. K. Yeh, Project Engineer, Analytical Engineering Department, Reed Research, Inc., for pointing out that certain corrections should be made in reference 1.

These typographical errors were made in the manuscript submitted for publication and therefore are not the fault of the publisher. It should be noted that the validity of the result curves given in the paper is not affected.

(1) In Eq. (3), the first term of the integral should read:

$$\left\{\left(\frac{\partial^2 w}{\partial x^2} + \frac{\partial^2 w}{\partial y^2}\right)^2 -\right.$$

(2) In Eq. (5), $(\partial^2 w/\partial x^2)^2$ and $(\partial^2 w/\partial y^2)^2$ should be replaced by $(\partial w/\partial x)^2$ and $(\partial w/\partial y)^2$, respectively.

(3) In the first term of Eq. (6), the number 16 should be replaced by the number 8.

(4) In Eqs. (7) and (8), the quantity $[1 - n^2\beta^2]^2$ should be replaced by the quantity $[1 + n^2\beta^2]^2$.

(5) The factor outside the bracket in Eq. (9) should read $8k_{bx}\beta^2\alpha i/\pi^2 A$.

(6) Expression (10) should be set equal to zero.

(7) In the expression for A following Eq. (10), the first term should read $(1 + i^2\beta^2)^2$.

(8) In the fourth line under the section "Use of the Curves," "Figs. 3" should be replaced by "Figs. 2."

(9) The expression for k_b in Fig. 4 should be divided by β^2.

(10) In the sentence next to the last sentence in the paper, "R_b" should be replaced by "R_x."

REFERENCE

[1] Noel, Robert G., *Elastic Stability of Simply Supported Flat Rectangular Plates Under Critical Combinations of Longitudinal Bending, Longitudinal Compression, and Lateral Compression*, Journal of the Aeronautical Sciences, Vol. 19, No. 12, p. 829, December, 1952.

Library Facilities of the
Institute of the Aeronautical Sciences

To serve Institute members and others in the aeronautical industry, the Institute of the Aeronautical Sciences offers the facilities of:

The W. A. M. Burden Library
2 East 64th Street
New York 21, N.Y.

The facilities of this library are available for reference study at the Institute.

The Paul Kollsman Lending Library
2 East 64th Street
New York 21, N.Y.

This library loans books without charge to members and others in the United States over eighteen years of age. Full information will be sent on request.

The Pacific Aeronautical Library
7660 Beverly Boulevard
Los Angeles 36, Calif.

This is a service and reference library for West Coast members and organizations. Full information as to its facilities will be sent on request.